Geodetic Deformation Model for the 2022 update of the New Zealand National Seismic Hazard Model

KM Johnson
IJ Hamling
MC Gerstenberger
LM Wallace
CA Williams
RJ Van Dissen
J Maurer
C Rollins

GNS Science Report 2021/37
September 2022

GNS SCIENCE
TE PŪ AO

DISCLAIMER

The Institute of Geological and Nuclear Sciences Limited (GNS Science) and its funders give no warranties of any kind concerning the accuracy, completeness, timeliness or fitness for purpose of the contents of this report. GNS Science accepts no responsibility for any actions taken based on, or reliance placed on the contents of this report and GNS Science and its funders exclude to the full extent permitted by law liability for any loss, damage or expense, direct or indirect, and however caused, whether through negligence or otherwise, resulting from any person's or organisation's use of, or reliance on, the contents of this report.

BIBLIOGRAPHIC REFERENCE

Johnson KM, Wallace LM, Maurer J, Hamling IJ, Williams CA, Rollins C, Gerstenberger MC, Van Dissen RJ. 2022. Geodetic deformation model for the 2022 update of the New Zealand National Seismic Hazard Model. Lower Hutt (NZ): GNS Science. 62 p. (GNS Science report; 2021/37). doi:10.21420/P93X-8293.

KM Johnson, Indiana University, Department of Earth and Atmospheric Sciences; Bloomington IN, 47405-7000, USA

LM Wallace, GNS Science, PO Box 30368, Lower Hutt 5040, New Zealand
University of Texas, Institute for Geophysics; Austin, TX 78705, USA

J Maurer, Missouri University of Science & Technology, Departments of Geosciences and Geological & Petroleum Engineering; Rolla, MO 65409, USA

IJ Hamling, GNS Science, PO Box 30368, Lower Hutt 5040, New Zealand

CA Williams, GNS Science, PO Box 30368, Lower Hutt 5040, New Zealand

C Rollins, GNS Science, PO Box 30368, Lower Hutt 5040, New Zealand

MC Gerstenberger, GNS Science, PO Box 30368, Lower Hutt 5040, New Zealand

RJ Van Dissen, GNS Science, PO Box 30368, Lower Hutt 5040, New Zealand

© Institute of Geological and Nuclear Sciences Limited, 2022
www.gns.cri.nz

ISSN 2350-3424 (online)
ISBN 978-1-99-101305-7 (online)
http://dx.doi.org/10.21420/P93X-8293

CONTENTS

FIGURES

TABLES

ABSTRACT

In order to incorporate geodetic measurements of contemporary deformation into the 2022 revision of the New Zealand National Seismic Hazard Model (NSHM), we develop strain rate and fault slip deficit rate models derived from New Zealand's interseismic Global Navigation Satellite Systems (GNSS)-derived velocity field. Four strain-rate maps, derived from different methodologies, underpin elastic deformation models that are based on inversions of strain rate for slip deficit rates on the suite of faults being used in the New Zealand NSHM 2022 fault model. The methodology adopted for the geodetic-based deformation model here is different from the more commonly adopted methods for estimating long-term fault slip rates using elastic block models or fault-based deep-slipping dislocation models. The need to estimate a geodetic slip rate for the large number of often closely spaced faults in the fault model preclude the use of standard block models, and rapid tectonic rotation of the eastern North Island, observed in the velocity field, makes fault-based models (that do not explicitly include block rotations) difficult to implement. The key advantages of the strain-rate inversion approach adopted here are that it obviates the need to model block rotations and is not hindered by the large number of closely spaced faults. Furthermore, the strain-rate inversion method directly estimates the slip deficit rate, which is the difference between the long-term slip rate on the fault and the present-day creep rate. Slip deficit is assumed to drive the rate of interseismic elastic strain accumulation, much of which we assume will be relieved in future earthquakes.

We compute strain-rate maps from the GNSS-derived velocity field using two purely statistical methods and two elasticity-based methods. The statistical methods include VELMAP, which solves for a spatially smooth velocity field by balancing the misfit between fitting observed velocities and minimising the Laplacian of the velocity field. The other uses geostatistical methods of variogram analysis and kriging to build realisations of the velocity and strain-rate fields with covariance structure inherent to the observed velocities. The physics-based methods derive a continuous velocity field using elasticity solutions. These methods solve for a distribution of body forces in an elastic thin plate that explain the observed velocity field and then compute the strain-rate field from the estimated distribution of forces. The Vertical Derivatives of Horizontal Stress (VDoHS) method uses the finite element method to compute elastic responses, while the body-force method adopts analytical expressions for the body-force responses.

The principal result from the strain-rate maps is that the mean maximum shear strain rate is similar across all methods, while the spatial distribution of dilatation and strain-rate style differs more significantly. The maximum shear strain rate averaged across the country varies between about 0.1 and 0.12 micro-strain/yr (~20% variation) and the dilatation rate between about 0.015 and 0.023 micro-strain/yr (~40% variation). The dilatation rates appear to show the impact of different types of spatial interpolation methods, with VDoHS and body-force results being relatively smooth, while VELMAP and geostatistics are comparatively rougher but with different characteristics. The uncertainties of the four methods are also quite variable and reflect the assumptions of the method, while differences between methods highlight these assumptions. In particular, there are large differences in the strain rates estimated offshore by the various methods. The uncertainties of the VDoHS, body force and VELMAP methods are small relative to the differences between methods, while the geostatistical method has uncertainty larger than the differences. The inversion of strain-rate maps for slip deficit rate is based on the commonly held assumption in nearly every geodetic-based inversion for slip rates that the majority of present-day strain-rate field is elastic strain due to interseismic coupling across actively slipping faults. Under this assumption, the strain-rate field is linearly related to the slip deficit rates on faults. We discretise the New Zealand NSHM 2022 community fault model into

rectangular slip patches in an elastic half space and solve for the spatial distribution of slip deficit rates on faults by inverting the four strain-rate maps. We conduct suites of inversions with and without the geologic slip rate model as a prior on slip deficit rates. The differences in slip deficit rate across all four strain-rate map inversions is typically less than 3–4 mm/yr for the high-rate faults. There are some notable differences between the geologic slip-rate model and the slip deficit inversion results. The geodesy-based inversions infer higher slip rates on belts of faults along the major strike-slip systems, including the Alpine Fault, the Marlborough Fault System and the northern part of the North Island Dextral Fault Belt. The geodesy-based inversions also infer systematically higher slip deficit rates on a complex system of reverse and strike-slip faulting in northern Canterbury and on some faults in the Otago region. The geodetic rates are systematically lower along the near-shore part of the Hikurangi margin. The slip deficit rate models explain 70–80% of the total strain-rate field; the remaining 20–30% of the strain-rate field cannot be mapped to slip deficit rates on faults. Residual strain rates that are not explained by slip deficit rates on faults are relatively low, with maximum shear strain rates typically less than about 0.1 micro-strain/yr. However, the residual strain rates are not randomly distributed; there are systematic spatial patterns to the style of the residual strain-rate field. indicating a potential tectonic origin to the residual strain rates. Finally, the depth distribution of slip deficit rate is not well resolved by the inversions on most of the faults.

KEYWORDS

Active faulting, geodesy, strain rates, seismic hazard models, fault slip rates

This page left intentionally blank.

1.0 INTRODUCTION

Since the early 1990s, our understanding of plate boundary zone crustal deformation has been revolutionised by advances in satellite-based geodetic techniques using Global Positioning Systems (GPS) and Interferometric Synthetic Aperture Radar (InSAR). Such methods allow us to directly track the movement of the ground in real time, quantify the rates of crustal deformation within plate boundary zones and determine the displacement of the Earth's surface during earthquakes. GPS (or, more recently, Global Navigation Satellite Systems [GNSS]) measurements are taken at survey points permanently attached to the ground either by intermittent (survey-style) or continuous (daily, automated) collection of phase and pseudo-range data from the constellation of GPS/GNSS satellites that orbit the Earth. Such measurements have allowed scientists to determine the distribution and rate of tectonic strain accumulation within plate boundary zones (e.g. Kreemer et al. 2000; Beavan and Haines 2001; Haines and Wallace 2020, among others).

Although GPS data provide a direct measure of contemporary surface displacements and contain important information regarding future seismic hazard, they are not yet widely used in probabilistic seismic hazard assessments, with a few notable exceptions such as California's UCERF-3 (Field et al. 2014). This is undoubtedly due in part to uncertainties regarding how modern strain rates relate to seismic hazard assessment. One of the advantages of GPS over geological and seismological studies is that it provides more complete spatial coverage and can help to detect 'hidden' active faults that have not yet been recognised. Moreover, geodetic data can provide additional independent information regarding active fault slip rates and the distribution of tectonic strain accrual that may ultimately result in future earthquakes. However, to be useful, the contemporary strain rates derived from GPS need to be interpreted in terms of fault slip rates and moment rate accumulation to be released in future earthquakes.

Much of the strain that contemporary GPS data detects is elastic, accumulating in the Earth's crust during the time between large earthquakes (the interseismic period) (e.g. Savage 1983; McCaffrey et al. 2000; Mazzotti et al. 2000; Wallace et al. 2004). This strain arises when two pieces of crust are prevented from sliding past one another along a fault by friction on the fault's surface. The two pieces of crust become stuck together at the fault, and the surrounding crust deforms elastically as the crustal blocks on either side of the fault continue to move in the far field. Faults can be locked together for hundreds or thousands of years until ultimately the accumulated stress overcomes the strength of the fault and failure in an earthquake occurs. Moreover, large surface displacements occurring during earthquakes (coseismic deformation) and for some extended period of time following an earthquake (post-seismic deformation) can complicate the use of geodetic data for future seismic hazard, as these transient signals produce large, measurable strains that are much higher than the background tectonic strain accumulation. This makes it important to utilise GPS velocity fields that measure the rate of strain / moment accumulation between earthquakes (e.g. interseismic deformation) and are free of coseismic and post-seismic deformation.

In order to incorporate geodetic measurements of contemporary deformation into the 2022 revision of the New Zealand National Seismic Hazard Model (New Zealand NSHM 2022), we develop strain rate and fault slip deficit rate models utilising New Zealand's interseismic campaign GPS-derived velocity field spanning 1995–2013 (Beavan et al. 2016; Figure 2.1). These models are used in two ways. First, strain rates derived from these velocity fields (see Section 3 of this report) are directly used to scale the background seismicity model (Rhoades et al. 2017). The use of geodetic data in the hybrid model of Rhoades et al. (2017) is not the subject of this report and will be discussed in a future report. In the second

(and primary topic of this report) approach, we utilise geodetic data to underpin 'backslip models' that invert the suite of strain-rate models for slip deficit rates on the same faults being used in the 'fault model' of the New Zealand NSHM 2022, deriving a geodetically based deformation model (see Section 4 for further details on the methodology and results; see Field et al. [2014] for specific definitions and usage of terms such as 'fault model' and 'geodetic deformation model'). This geodetic deformation model will be incorporated into the New Zealand NSHM 2022 in a similar way to which the geologic deformation model(s) are used.

The most recent version of California's probabilistic seismic hazard model (UCERF3; Field et al. 2014) utilised geodetic data in their deformation model for the first time by undertaking joint modelling of geologic fault slip rates and the interseismic GPS-derived velocity field to estimate fault slip rates using three different approaches. These included: (1) Elastic block models (e.g. McCaffrey 2002, 2005; Johnson and Fukuda 2010; Hammond et al. 2011); (2) Deep-slipping dislocation models (Zeng and Shen 2014, 2016); and (3) NeoKinema (Bird 2009), which uses a finite element approach to invert geologic, geodetic and stress orientation data to estimate a long-term deformation field (including both on- and off-fault deformation). We considered these approaches in our effort to incorporate geodetic data into the New Zealand NSHM 2022, but ultimately decided to use a different approach (outlined in Section 3) that inverts the strain-rate field (rather than the velocity field) for backslip (or slip deficit rate) on faults in the New Zealand NSHM 2022 fault model. The need to estimate a geodetic slip rate for all 703 faults considered in the New Zealand NSHM 2022 precluded use of a block model, as this would require use of an overly complex (and probably unphysical) model with hundreds of independent tectonic blocks bounded by faults. Such a model would not be well constrained by the data (some blocks would have no, or very few, GPS velocities to constrain their motion) and would also push the model to a level of detail where the physical validity of the block model assumption breaks down. Deep-slipping dislocation models (e.g. Beavan et al. 1999; Zeng and Shen 2016) provide a means to determine long-term fault slip rates below the portion of the fault that is locked, and the derived strain rates are mathematically equivalent to backslip models. However, fitting the rapid tectonic rotation of the eastern North Island observed in the velocity field (Wallace et al. 2004; Figure 2.1) would be difficult, if not impossible, to fit with such an approach. NeoKinema utilises an iterative forward modelling approach to estimate the contribution from fault locking, which limits the range of models and uncertainty space that can be explored.

A key advantage to the strain rate/backslip approach is that it relies on determining the slip deficit rate (or moment accumulation rate), which is directly relevant to the rate of elastic strain accumulation, much of which we assume will be relieved in future earthquakes. Slip deficit rate is defined as the difference between the long-term slip-fault slip rate and the present-day creep rate and is modelled with backslip. The alternative approaches discussed above were implemented with a focus on obtaining long-term slip rates, which then must be scaled with an 'aseismicity factor' to account for the possibility that not all of the long-term fault slip accrues seismically. Moreover, utilising strain rates (rather than velocity fields) avoids the need to account for rotating rigid block motions or deep-slipping dislocation sources that are required to fit the far-field component of the GPS-derived velocity field.

2.0 DATA

This project makes use of the comprehensive GNSS campaign velocity field for New Zealand collected under the leadership of the late John Beavan (Beavan et al. 2016; Figure 2.1). The velocity field is based on data acquired between 1998 and 2013 and includes corrections for recent earthquakes during that period, such as the 2010/11 Canterbury earthquake sequence, and therefore represents interseismic deformation. The campaign GNSS network is relatively dense, with average site spacing between sites of <10–20 km, varying from around 5 km in more densely-sampled areas to 50 km in less tectonically active regions (such as the Northland and Waikato regions). We use this velocity field (and formal data uncertainties, Figure 2.2) to estimate surface strain rate using the various methods discussed below; the strain-rate models are then used to constrain the inversions for slip deficit rates on faults encompassed by the New Zealand NSHM 2022 fault model, as discussed in Section 4. Note that velocities from most continuous GNSS stations available in New Zealand were not included in the velocity field, as we restrict ourselves to utilising the published (and peer-reviewed) New Zealand GNSS velocity field of Beavan et al. (2016).

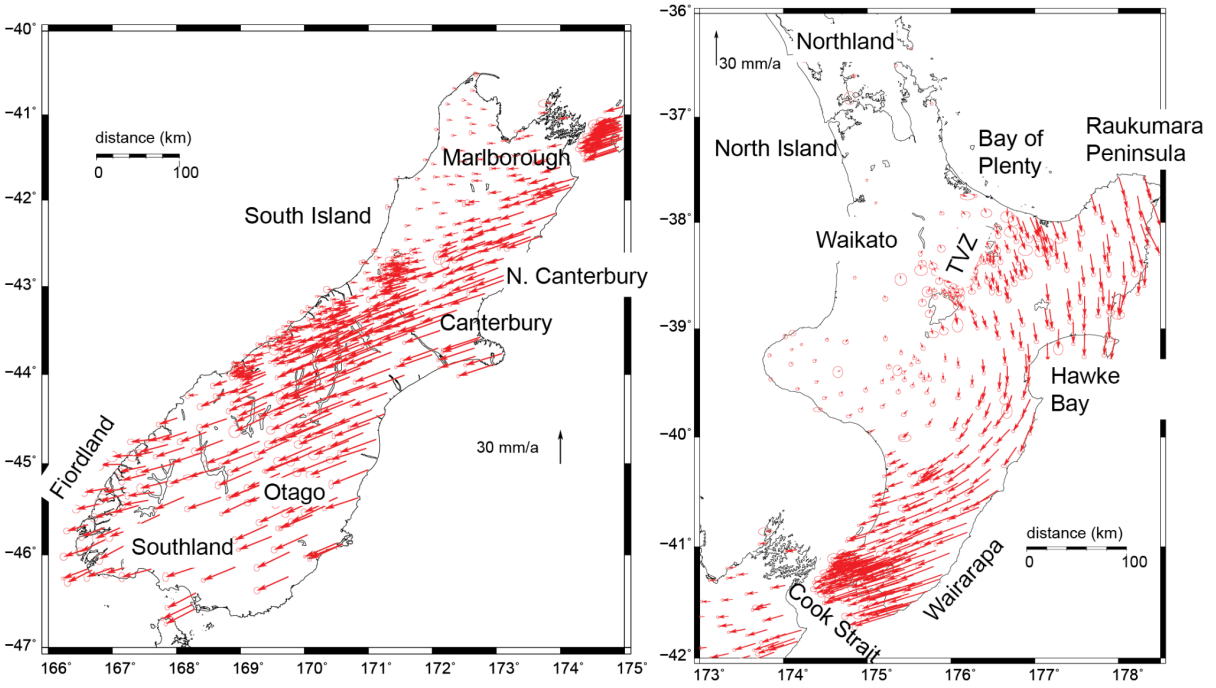

Figure 2.1 GNSS velocity field from Beavan et al. (2016), relative to a fixed Australian Plate. (Left) South Island; (right) North Island.

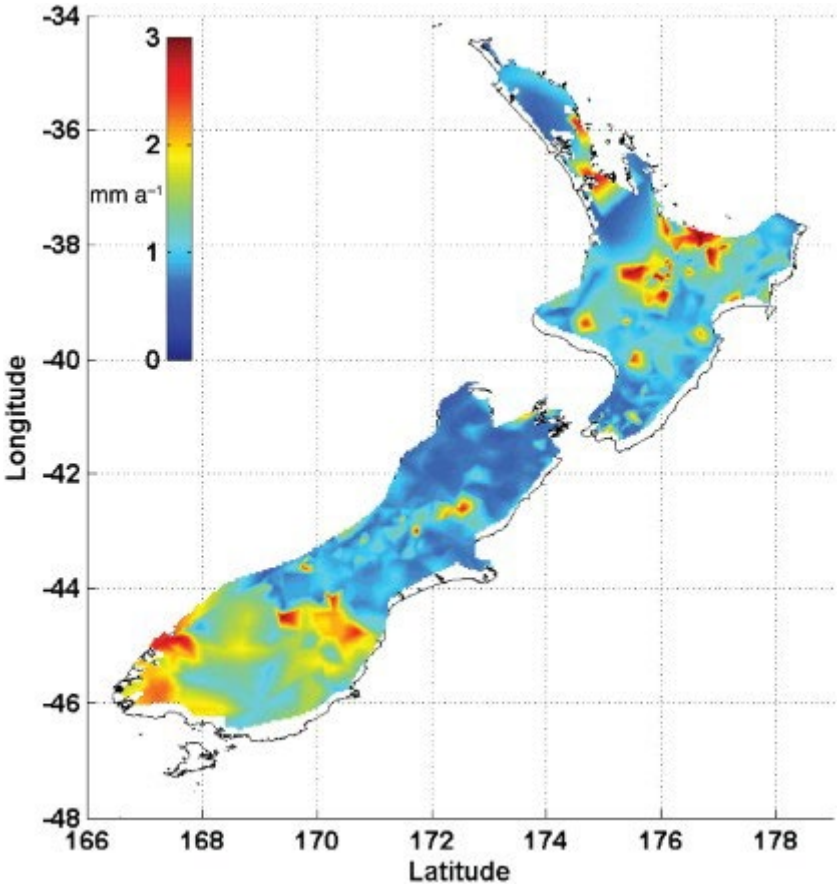

Figure 2.2 GNSS velocity field uncertainty magnitude from Beavan et al. (2016).

2.1 Correcting the Velocity Field for Deformation Related to Sill Cooling in the Central North Island

The Taupō Volcanic Zone (TVZ), located in centre of New Zealand's North Island, has formed over the last ~2 Ma as a consequence of the continuing subduction of the Pacific Plate beneath the Australian Plate and rotation of the fore-arc (Wallace et al. 2004). Long-term (hundreds of thousands of years) extension through the central TVZ has resulted in the development of a NE–SW-trending extensional (normal) fault belt (e.g. Davey et al. 1995; Villamor and Berryman 2001) with estimates of long-term slip rates ranging from 1.2 to 2.8 mm yr^{-1} at the surface and to ~10 mm yr^{-1} at seismogenic depths (6–10 km) (Villamor and Berryman 2001). However, contemporaneous deformation indicates that the present day TVZ is largely undergoing contraction (Holden et al. 2015; Haines and Wallace 2020; Dimitrova et al. 2016; Hamling et al. 2015). There are numerous mechanisms that can help explain contraction and subsidence in and around active volcanic centres, including the withdrawal of magma at depth (Dzurisin et al. 1990, 1994), regional extension (Peltier et al. 2009) and the contraction of cooling magma (Sigmundsson et al. 1997, Poland et al. 2006; Hamling et al. 2015). In the TVZ, the contraction has been previously explained by the cooling and contraction of melt at depth (Hamling et al. 2015; Holden et al. 2015), which is consistent with pockets of interconnected melt, imaged by magnetotellurics (Heise et al. 2010; Bertrand et al. 2015) and seismic velocity models, suggesting a heavily intruded shallow crust beneath the central TVZ (Harrison and White 2004, 2006; Stratford and Stern 2004, 2006). Other models, based on the flexure of the upper crust as a result of variations in the rates of deep upwelling of mantle material, have been invoked to explain the subsidence through the TVZ (Lamb et al. 2017). However, given the extensive evidence of shallow magma pockets distributed through the TVZ, our preferred model assumes that the subsidence is related to the cooling and contraction of melt. To correct

for the contraction and subsidence throughout the central TVZ, we use an updated model of Hamling et al. (2015), which includes additional SAR data up to 2020. The model consists of a horizontal set of tensile dislocations to represent the cooling and contraction of a sill-like body at 9.5 km depth. The model is discretised into ~1900 individual patches, and we solve for the best-fitting contraction at each patch. Here we follow the method of Hamling et al. (2022a) and use regional magnetotelluric data to help constrain the spatial extent of contraction (Figure 2.3). The best-fitting model, which predicts a volume loss of ~0.02 km^3/yr, is then used to remove the expected horizontal contraction rates from the interseismic velocity field. While our preferred model is based on the assumption of cooling magma at depth, the model of Lamb et al. (2017) produces similar fits to the data and so, regardless of which model is invoked, the correction would be largely the same.

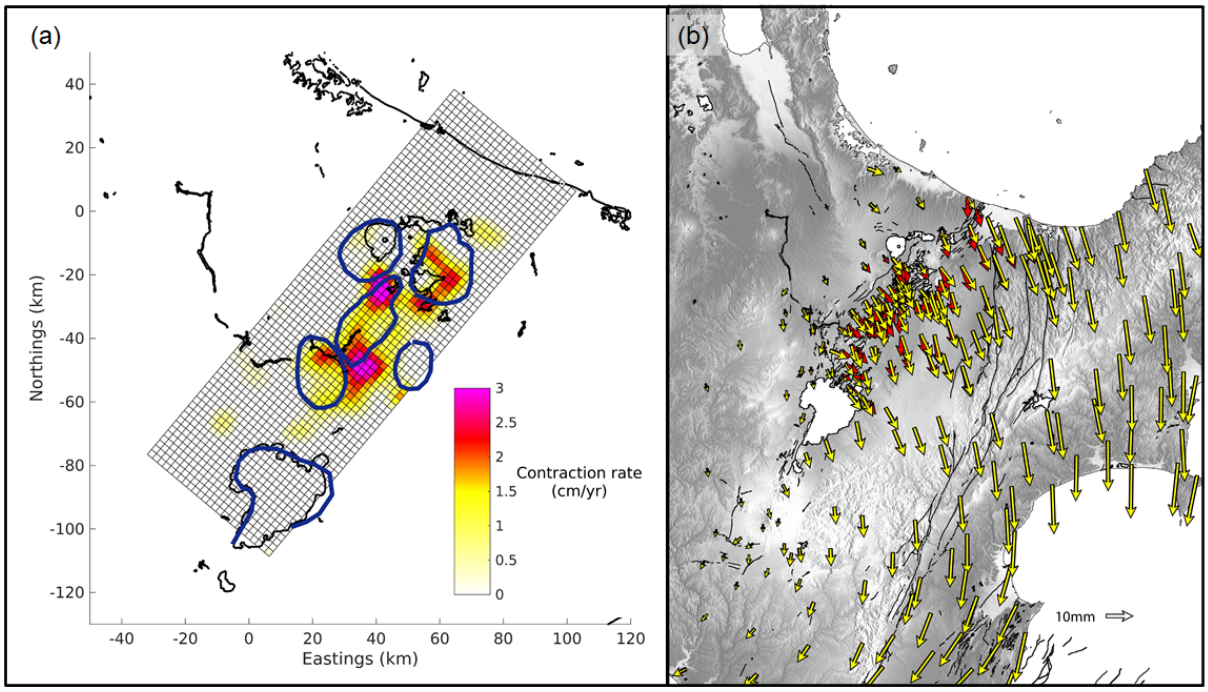

Figure 2.3 (a) Best-fitting contraction model (due to sill cooling) based on the inversion of GPS and InSAR data between 2015 and 2020. The dark blue lines denote caldera boundaries. (b) Difference between uncorrected (red arrows) and corrected (yellow) velocities based on the contraction model shown in (a).

2.2 Correcting the Velocity Field for Elastic Strain due to Coupling on the Hikurangi Subduction Interface

The inversions for slip deficit rate discussed in Section 4 do not include the Hikurangi subduction interface as a source; the inversions solve for slip deficit rates only on crustal faults. (i.e. all faults in the New Zealand NSHM 2022 fault model, with the exception of the Hikurangi subduction interface and the Puysegur subduction interface). We do this because adding the large Hikurangi subduction zone source (with many fault patches) to the inversion framework greatly increases the number of free parameters in the inversion and compromises our ability to explore the full parameter space in a computationally efficient manner. Instead, we take advantage of well-established block modelling methods to invert the velocity field for Hikurangi subduction interface coupling (e.g. Wallace et al. 2004; 2012) to determine the influence of subduction interface locking on the velocity field. We then subtract the component of deformation due to elastic strain from Hikurangi locking from the Beavan et al. (2016) velocity field (also corrected for sill cooling in the TVZ deformation discussed in Section 2.1) and use the remaining velocity field to derive the strain-rate maps (see Section 3) that are used

as input into the inversions of strain rate for slip deficit rate on the crustal faults (Section 4). Moreover, Williams and Wallace (2015, 2018) have a well-established framework to incorporate heterogeneous elastic properties into such block model inversions for Hikurangi subduction interface deformation, allowing us to easily account for the influence of realistic elastic properties in our Hikurangi block rotation and slip deficit models. Previous work has shown that accounting for such spatial variations in elastic properties is important when undertaking inversions for crustal deformation at subduction zones, due to the large elastic contrasts between the rigid subducting slab (and less rigid forearc). Williams and Wallace (2015, 2018) showed that, in the case of slow-slip events, the amount of slip can be under- or over-estimated (depending on the depth of the events) by up to 40%, and we expect a comparable effect for slip deficit rate estimates at subduction zones. In addition to using the new interseismic coupling model to correct the velocity field (for our inversions of backslip on the crustal faults in the NSHM), the new coupling model is also being used in a separate study (in conjunction with paleoseismic data bearing on past earthquake ruptures) to inform the deformation model for the Hikurangi subduction interface in the New Zealand NSHM 2022.

For the block models, we divide New Zealand into multiple tectonic blocks based on the locations of known, active faults following the model of Wallace et al. (2012), updated to include the revised Hikurangi subduction interface geometry of Williams et al. (2013). The Williams et al. (2013) geometry also serves as the basis for the Hikurangi subduction source in the New Zealand NSHM 2022. The elastic block model utilises the TDefnode software (McCaffrey 2009), which applies simulated annealing to downhill simplex minimisation (e.g. Press et al. 1989) to solve for the angular velocities of the specified tectonic blocks and coupling coefficients for faults between the blocks. Unlike our previous models (e.g. Wallace et al. 2012), which were based only on horizontal GPS velocities, our block model includes vertical deformation rates from InSAR (Hamling et al. 2022b) and the continuously operating GNSS sites in the GeoNet network and incorporates realistic elastic properties into our inversions (e.g. Williams and Wallace 2015). We also relax assumptions made in previous Hikurangi subduction locking inversions that forced a monotonic down-dip decrease in interseismic coupling. We minimise data misfit, defined by the reduced chi-squared statistic (χ_n^2) in our inversion for the best-fitting block rotation poles and interseismic coupling coefficients. See Wallace et al. (2012) for additional details on the block model developed for the New Zealand region and how the inversions were undertaken.

The elastic contribution to the velocity field from the fault slip rate deficit on the Hikurangi subduction thrust is calculated using the PyLith finite element package (Aagaard et al. 2013, 2017a, 2017b). As mentioned previously, variations in elastic properties can have a significant effect on the predicted surface displacements due to slip on the subduction interface (Williams and Wallace 2015, 2018). Using PyLith, we are able to directly use seismic velocities from the New-Zealand-wide seismic velocity model (Eberhart-Phillips et al. 2010; Eberhart-Phillips and Bannister 2015; Eberhart-Phillips and Reyners 2012) to constrain our elastic properties when generating Green's functions. We are then able to integrate the Green's functions generated by PyLith to obtain those required by TDefnode, exactly as was done in Williams and Wallace (2015). The region surrounding the Hikurangi subduction interface contains the most significant elastic property variations in the New Zealand study region and is therefore the most important source to account for these effects in our analysis.

Our new subduction coupling (Figure 2.4a) model reveals a more heterogeneous distribution of coupling than previously published models (Figure 2.4b). Similar to previous studies, we observe deep locking at the southern Hikurangi subduction interface and a largely creeping interface in the northern and central portion of the subduction zone. However, the new models

highlight additional, discrete patches of locking embedded within the mostly creeping interface at the central and northern Hikurangi margin. These patches of coupling are also resolved as regions of elevated contractional strain in strain-rate maps of New Zealand's North Island (e.g. Dimitrova et al. 2016; Haines and Wallace 2020). Most notable of these is a locked patch located down-dip of the slow-slip region offshore Hawkes Bay. This patch is required in the model to fit relatively high subsidence rates observed above the locked patch from InSAR, as well as the contraction identified there in earlier studies.

The impact on the estimated slip deficit rates from using realistic elastic properties for derivation of the Green's functions for the Hikurangi subduction fault is also significant (Figure 2.5). The slip deficit rate in the deeply locked portion of the southern North Island for the heterogeneous model is ~5–7 mm/yr lower than for the uniform elastic half-space model, which is an approximately 20% difference in the slip deficit rate estimates. This is consistent with the results of Williams and Wallace (2015), who obtained ~20% lower slip amounts for deep slow-slip events when using models with realistic elastic properties, compared to the uniform half-space models. We note that some of the differences (Figure 2.5) between the two models for the offshore region may simply be a consequence of lack of resolution of offshore coupling with onshore geodetic data.

Figure 2.6 shows the elastic component due to locking on the subduction zone from the best-fit coupling model (Figure 2.4a). These velocities are subtracted from the Beavan et al. (2016) velocity field for the strain-rate estimates (Section 3) and slip deficit rate / backslip estimates for the crustal faults (Section 4).

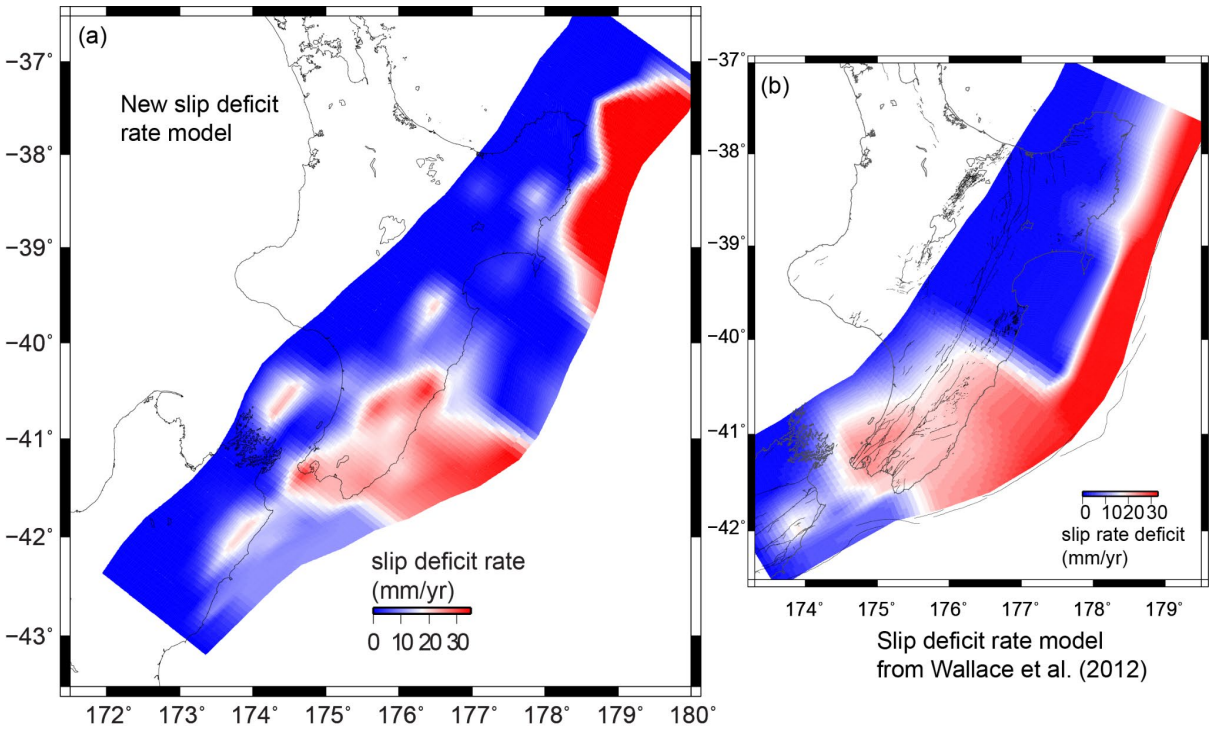

Figure 2.4 Comparison of slip deficit rate models from (a) this study and (b) a previous model of Wallace et al. (2012). The new model (left) has relaxed the assumption of a monotonic down-dip decrease in coupling (imposed by earlier published models) and also accounts for heterogeneity of elastic properties in the New Zealand region (the earlier models assume a uniform, elastic half-space). We note that both of these models are based on onshore GNSS and InSAR data and therefore have very little resolution in the offshore regions of the subduction interface.

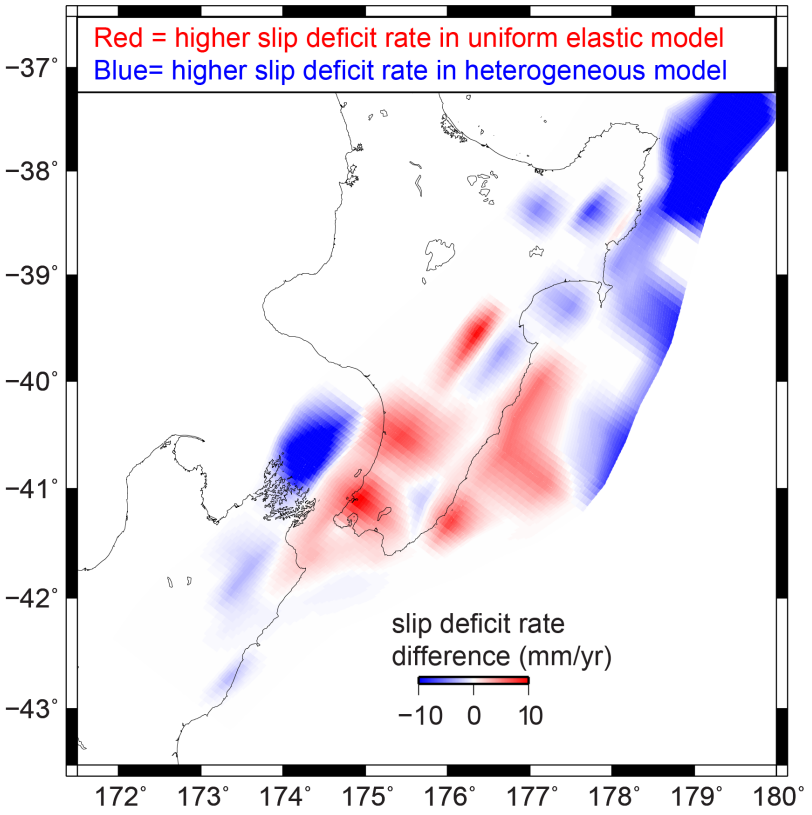

Figure 2.5 The difference in slip deficit rates between the coupling models with homogeneous elastic properties versus the heterogeneous elastic properties. The plot shows slip rate deficit differences for the homogeneous model minus the heterogeneous model.

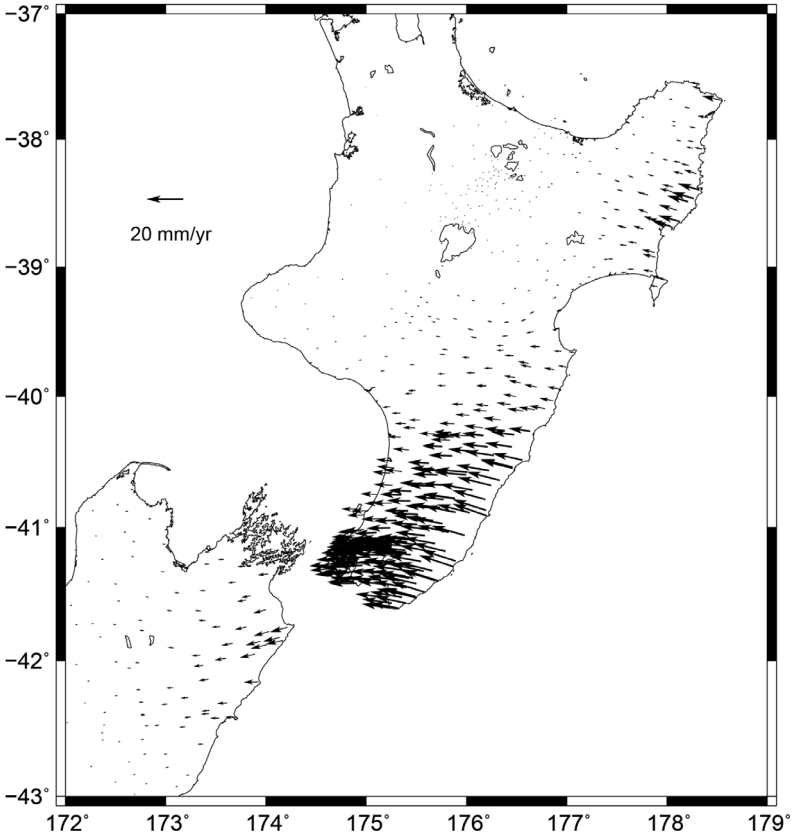

Figure 2.6 The horizontal deformation produced by interseismic coupling on the Hikurangi subduction zone from the best-fit model shown in Figure 2.4a. This component is removed from the velocity field in Figure 2.1 to create the strain-rate models for the slip rate deficit inversions for crustal faults in the model (see Figure 3.1 for the velocity field corrected for the above locking model).

Below, we show strain-rate models with and without the removal of elastic strain due to Hikurangi subduction coupling. Only strain-rate fields with the Hikurangi component removed are used in the slip deficit rate calculation to derive crustal fault slip rates (slip rate deficits), while the full strain-rate fields are used for the background seismicity model (via the hybrid model approach of Rhoades et al. [2017]), which is not a topic of this report. We also acknowledge the possibility that some of the elastic strain being interpreted as due to locking on the Hikurangi subduction zone could instead arise from slip deficits on crustal faults overlying the plate interface. Although inclusion of upper-plate faults in our block model for subduction interface coupling helps to avoid this to some degree, ideally, for future versions of the NSHM, we should instead be inverting simultaneously for crustal fault slip deficit rates, along with the subduction interface.

3.0 STRAIN-RATE MODELS

Strain rate has been linked to seismicity rate and moment accumulation (e.g. Kostrov 1974; Savage and Simpson 1997) and, in some recent studies, has been shown to correlate to the background seismicity rate (Zeng et al. 2018; Stevens and Avouac 2021) and rate of major earthquakes (e.g. Hussain et al. 2018). Thus, robust estimation of the surface strain rate tensor should provide valuable constraints on seismic hazard. Estimating the complete 2D or 3D strain tensor requires knowledge of the full 3D velocity field everywhere, while geodetic data such as GNSS only have spatially scattered data on the surface of the Earth. To use this data to estimate strain rates, some type of interpolation is required and the assumption of a 2D strain-rate field is used. Numerous methods and algorithms have been proposed for this purpose, but few published studies to date have systematically explored the differences in the methods or what implications these differences have for understanding crustal strain. Wu et al. (2011) discuss a few different methods and suggest that using spatial covariance information improves the fit and reduces artifacts in the interpolated strain-rate field. Baxter et al. (2011) discuss problems with calculating strain rates from sparse velocity observations and show that artifacts can be present. Given these uncertainties and the diversity of approaches developed to determining strain rates from GNSS velocity fields, we use four different methods to determine four strain-rate fields for New Zealand as input to the backslip inversions (Section 4), allowing us to account for the epistemic uncertainties in the estimation of strain rates from geodetic velocities.

3.1 Surface Strain Rate and Seismic Hazard

The surface strain-rate tensor is a symmetric, positive-definite tensor with three independent components represented by:

$$\dot{\epsilon}_{ij} = \frac{1}{2}\left(\frac{dv_i}{dx_j} + \frac{dv_j}{dx_i}\right) \qquad \text{Equation 3.1}$$

where v_i is the i^{th} component of the velocity of the surface. Here, we focus on surface strain rates, so i,j = 1,2. The 'principal strain rates' are defined as the eigenvalues of the strain-rate tensor: $\dot{\varepsilon}_1$ and $\dot{\varepsilon}_2$. Two invariants are of particular importance: one-half of the trace of the strain-rate tensor, which equals the areal strain rate or dilatation (change in area):

$$\dot{\Delta A} = 0.5(\dot{\epsilon}_{11} + \dot{\epsilon}_{22}) = 0.5(\dot{\epsilon}_1 + \dot{\epsilon}_2) \qquad \text{Equation 3.2}$$

and the maximum shear strain rate:

$$\dot{\gamma} = \sqrt{(\dot{\epsilon}_{11} - \dot{\epsilon}_{22})^2 + 4\dot{\epsilon}_{12}^2} = \dot{\epsilon}_1 - \dot{\epsilon}_2 \qquad \text{Equation 3.3}$$

Savage and Simpson (1997) considered the relation between strain and seismic moment accumulation rate. The interseismic moment deficit rate (MDR) for a given fault can be defined as

$$\dot{M}_d = G\dot{s}A_f \qquad \text{Equation 3.4}$$

for shear modulus G, mean slip deficit rate s and the relevant fault area A_f. Savage and Simpson (1997) suggest that the minimum MDR can be calculated from the surface strain rate by assuming a seismogenic thickness and using the maximum principal strain rates:

$$\dot{M}_d \geq 2GA_sH|\dot{\epsilon}^{\max}| \qquad \text{Equation 3.5}$$

where $|\dot{\varepsilon}^{max}| = max\{|\dot{\varepsilon}_1|, |\dot{\varepsilon}_2|, |\dot{\varepsilon}_1 + \dot{\varepsilon}_2|\}$ is the maximum principal strain rate and A_sH is the volume of crust under uniform strain rate. The assumption here is that the estimated surface strain rate is constant with depth. Thus, the surface strain rate should provide a lower bound on the seismic moment accumulation rate.

Even with a spatially dense GNSS velocity field, to compute strain rate from scattered velocities requires some form of interpolation scheme. Methods for calculating strain rate can be broken into several broad classes:

1. Direct calculation of strain from baselines, typically involving some type of triangulation like Delaunay (e.g. Savage et al. 2001; Cai and Grafarend 2007).
2. Fitting the velocity field using various types of basis functions (polynomials, splines, wavelets, etc.) (e.g. Feigl et al. 1993; Haines and Holt 1993; Beavan and Haines 2001; Tape et al. 2009; Hackl et al. 2009; Wang and Wright 2012; Weiss et al. 2020).
3. Approaches based on elasticity theory (e.g. Noda and Matsu'ura 2010; Haines et al. 2015 [VDoHS]; Sandwell and Wessel 2016).
4. Weighted mean approaches, including methods based on spatial statistics (sometimes referred to as 'least squares collocation', e.g. Shen et al. 1996; El-Fiky et al. 1997; Kato et al. 1998; Goudarzi et al. 2015; Tarayoun et al. 2018).
5. Approaches that use a locally-weighted regression approach that involves defining a moving local neighbourhood and solving for a simple (e.g. linear) field around each station (Shen et al. 2015).

Note that while (1) only calculates strains along baselines connecting stations, (2–5) all involve interpolation. (1) is generally unsatisfactory, because it does not account for data errors, and hence baseline strain-rate estimates tend to be noisy. The other approaches require interpolation and numerical calculation of derivatives. Numerical derivatives, for sufficiently dense node spacing, are typically not a large source of error compared to the interpolation step itself. We use four different methods for interpolating velocities from the GNSS velocity field, one representative from class 2 and 4, and two different methods from class 3, to account for the uncertainty in the resulting strain-rate field arising from choice of interpolation method.

In this study, we present a comparison of four methods for strain-rate calculation: (a) the VDoHS method (Haines et al. 2015; Haines and Wallace 2020), (b) a method based on calculation of body forces using Green's functions (similar to Sandwell and Wessel 2016), (c) VELMAP (Wang and Wright 2012; Weiss et al. 2020) and (d) a method based on geostatistics. We implement each of these methods using the same set of observations (the campaign GNSS field published by Beavan et al. [2016]). Each method adopts a different grid based on the requirements of that method, so we interpolate all of the gridded results to the grid used in the slip inversions (Figure 3.1). This permits direct study of the differences in results arising from the models themselves with their various built-in assumptions. Each of the methods are described briefly below, with results shown from each model with and without the predicted Hikurangi signal removed. Then, we calculate the mean model of the four methods and the residual fields and discuss the differences between models and the implications for strain-rate estimation.

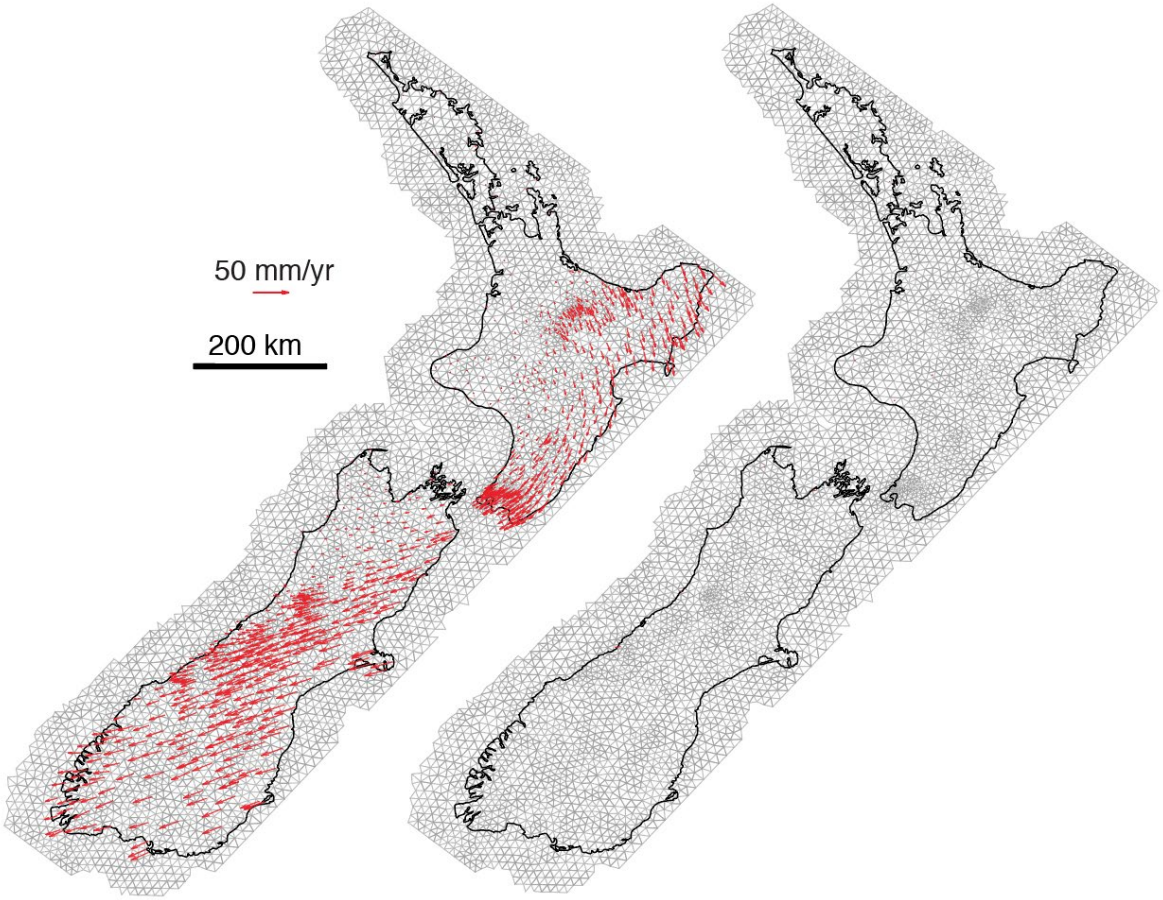

Figure 3.1 Mesh constructed for the strain-rate interpolation. The mesh size is determined by density of GPS velocity observation coordinates (shown in the left-hand version). Each of the four methods provide velocity and strain rate interpolated to these grid nodes for direct comparison.

3.1.1 Vertical Derivatives of Horizontal Stress

The VDoHS method, first developed in Haines et al. (2015), assumes an elastic thin plate and solves for a set of body forces that explain the velocity field, then uses those forces to compute strain rates. VDoHS rates are essentially spatial derivatives of stress rates and as such are a more spatially compact surface expression of subsurface deformation than conventionally used strain rates, which are themselves a spatial derivative of displacement fields. The Haines method uses the horizontal force balance equations at the Earth's surface to invert the GNSS velocity field for VDoHS rates. The VDoHS rates are then integrated to produce strain-rate fields, without the need for arbitrary smoothing required by strain-rate estimation methods that take spatial derivatives of the GNSS velocity field (such as the VELMAP method in Section 3.1.3 and similar previous methods used by Kreemer et al. [2000], Beavan and Haines [2001] and Hackl et al. [2009]). Because this method integrates VDoHS rates to obtain strain rates, there is no amplification of spatial domain noise, unlike methods that take derivatives of displacement fields. The VDoHS method has been implemented in Iceland (Árnadóttir et al. 2018), in the North Island of New Zealand (Dimitrova et al. 2016) and on a New-Zealand-wide basis (Haines and Wallace 2020) to produce a high-resolution view of tectonic and volcanic deformation in those locations. It has also been adapted for use with GPS time series to resolve transient slow-slip events and locking processes at the Cascadia subduction zone (Haines et al. 2019).

The basic approach, first published in Haines et al. (2015), uses a finite element approach and imposed horizontal body forces at specified locations, which deform the elastic body (Figure 3.2). The quasi-static force balance equations in 2D are:

$$\left(\frac{2}{1-\nu}\right)\frac{\partial^2 u}{\partial x^2}+\left(\frac{2\nu}{1-\nu}\right)\frac{\partial^2 v}{\partial x\partial y}+\frac{\partial^2 u}{\partial y^2}+\frac{\partial^2 v}{\partial x\partial y}=\frac{-f_x}{\mu}\delta(x)\delta(y)$$
$$\frac{\partial^2 u}{\partial x\partial y}+\frac{\partial^2 v}{\partial x^2}+\left(\frac{2\nu}{1-\nu}\right)\frac{\partial^2 u}{\partial x\partial y}+\left(\frac{2}{1-\nu}\right)\frac{\partial^2 v}{\partial y^2}=\frac{-f_y}{\mu}\delta(x)\delta(y),$$

Equation 3.6

(Haines et al. 2015), where f_x and f_y are the body forces and μ is the shear modulus. Haines and Wallace (2020) set up a grid of nodes co-located with the GNSS stations (Figure 3.2) and inverted for body forces that match the observed velocity field, which are used to determine the predicted velocity and strain rate everywhere. We undertake the same procedure outlined in Haines and Wallace (2020) to derive strain rates from the velocity field but, in the current case, use the velocity field corrected for sill cooling in the TVZ (Section 2.3), and, for the backslip calculation, we also remove the Hikurangi subduction component of deformation (Section 2.2). As with the other four strain-rate methods, we interpolate the high-resolution strain-rate field generated using the VDoHS method to a common grid used for the ensemble method calculation (Figure 3.1) using linear interpolation.

Haines and Wallace (2020) provided uncertainties on strain rate (Figures 3.3 and 3.4), which we use here to generate realisations of the strain-rate field for comparison purposes to the other methods. We generate realisations by multiplying a zero-mean normally distributed vector by the Cholesky factor of a covariance matrix representative of the uncertainty field, using an exponential variogram model to capture spatial correlations in the field. We do this many times to generate many spatially correlated noise realisations and then add those (zero-mean) fields to the original (mean) strain-rate components. The resulting realisations have the same ensemble mean and variance as the original fields.

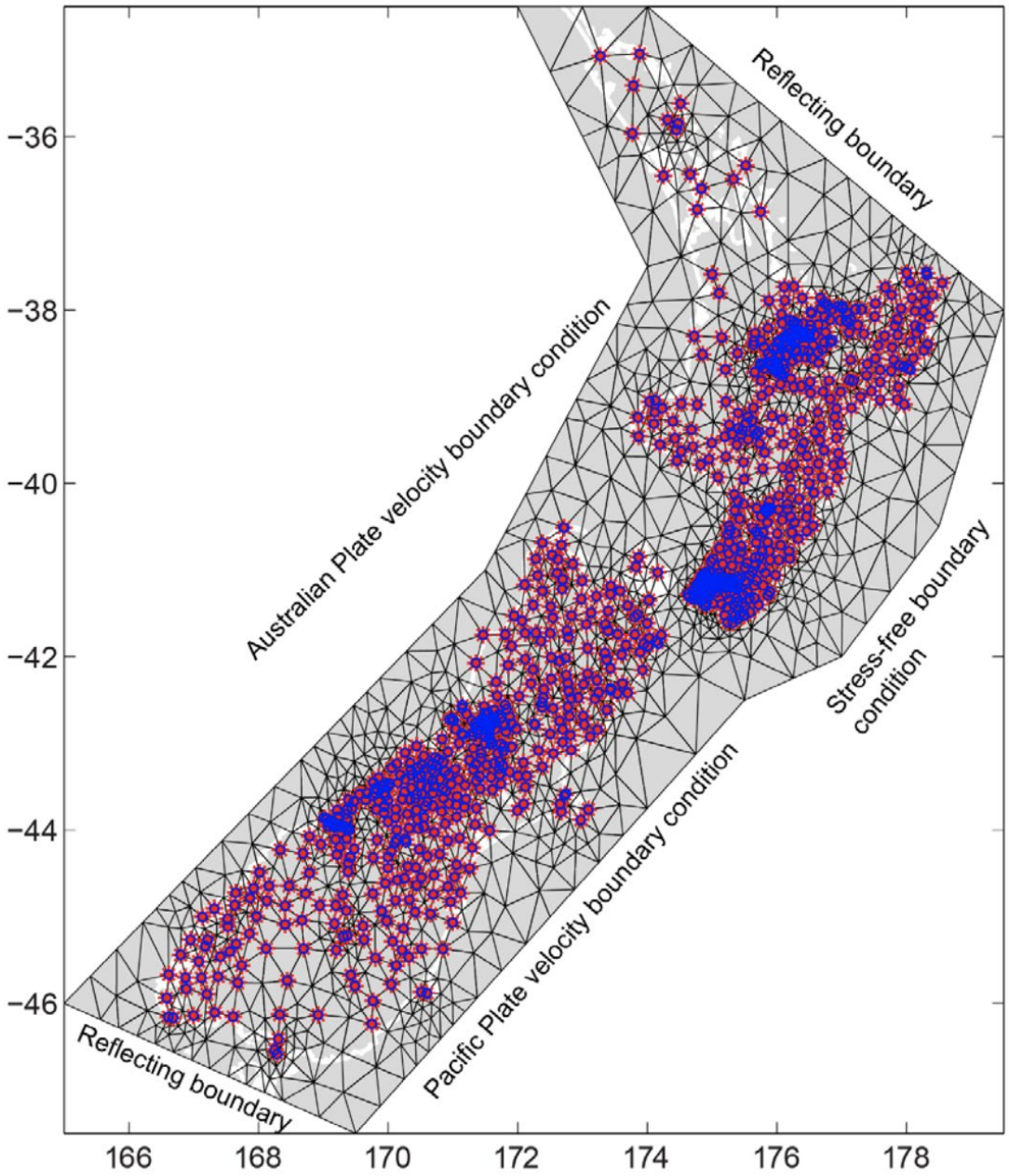

Figure 3.2 Grid originally used for determining the basis functions for the VDoHS rate inversions. In most cases, vertices (blue dots) are located at the GPS sites (red dots) used in the inversion. If GPS stations are closer than a minimum spacing (0.04 degrees), we replace the corresponding vertices with a single vertex at the average location of the GPS stations weighted by the inverse of the velocity variances. The nature of the boundary conditions for the model domain are discussed further in Haines and Wallace (2020). From Haines and Wallace (2020).

3.1.2 Body-Force Method

Sandwell and Wessel (2016) developed a method related to the VDoHS method (Section 3.1.1) to compute a smoothed velocity field from scattered data. They derive the Green's functions for a point body force in a thin elastic sheet and use them to calculate displacements instead of solving a finite element problem. The analytical solution method has been implemented as an interpolation algorithm of 2D vector data as a module *gpsgridder* in the Generic Mapping Tools (GMT; Wessel et al. 2013). The relationship between displacements and body force magnitude is linear and depends on one elastic parameter, Poisson's ratio. The Sandwell and Wessel (2016) method works by placing 2N body forces at N observation coordinates. Each observation coordinate has an east and north velocity/displacement component, so there

are 2N observations and 2N unknowns, providing a unique solution for body forces and a unique interpolation solution. In our method, we adopt the analytical thin-elastic-sheet Green's functions presented in Sandwell and Wessel (2016) but set up the velocity field interpolation as an over-determined inverse problem, similar to the VDoHS method (Haines et al. 2015).

We begin with the triangular mesh shown in Figure 3.1. The nominal node spacing in areas without data is 15 km, but the mesh is refined in regions of more dense data; for example, the node spacing is about 4 km in the Wellington region. The mesh is generated using a Matlab-based 2D unstructured mesh generator called *mesh2d* (Engwirda 2014; Figure 3.1). Body forces are placed at each triangular node and velocities (corrected for Hikurangi coupling and sill deformation in the central North Island; see Sections 2.1–2.2) and strain rates are computed at the triangle centroids.

Sandwell and Wessel (2016) provide the mathematical relationship between the vectors of observed velocities, *v*, and the vector of body forces, *f*, at all nodes:

$$\mathbf{v} = \mathbf{G}_v \mathbf{f}$$

Equation 3.7

where G_v is a matrix of body force Green's functions. Similarly, the strain rates at centroids of triangles are computed from body forces and the analytical Green's functions for strain rate as:

$$\epsilon = \mathbf{G}_\varepsilon \mathbf{f}$$

Equation 3.8

This is a highly under-determined problem, so we add an additional damping constraint on the magnitude of body forces and solve the following system of equations:

$$\begin{bmatrix} \Sigma_v^{-1/2}\mathbf{v} \\ \mathbf{0} \end{bmatrix} = \begin{bmatrix} \Sigma_v^{-1/2}\mathbf{G}_v \\ \alpha^2\mathbf{I} \end{bmatrix} \mathbf{f}$$

Equation 3.9

where I is the identity matrix, α is the damping parameter that determines the relative weight placed on fitting the velocity data versus keeping the body forces small and Σ_v is the diagonal matrix of variances for the velocities. This is a standard linear system that can be solved with least squares methods. The generalised inverse is:

$$\mathbf{G}^\sharp = \left[\mathbf{G}_v^T \Sigma_v^{-1} \mathbf{G}_v + \alpha^{-2}\mathbf{I}\right]^{-1} \Sigma_v^{-1/2} \mathbf{G}_w^T$$

Equation 3.10

(e.g. Menke 2018; Aster et al. 2018) and the best-fitting body forces, for a given α, are:

$$\mathbf{f}_\alpha = \mathbf{G}^\sharp \mathbf{v}$$

Equation 3.11

with covariance matrix:

$$\mathbf{\Sigma}_\alpha = \mathbf{G}^\sharp \mathbf{\Sigma}_v \left(\mathbf{G}^\sharp\right)^T$$

Equation 3.12

From this least squares solution, we can write the predicted strain rates due to body forces as:

$$\epsilon_\alpha = \mathbf{G}_\varepsilon \mathbf{f}_\alpha$$

Equation 3.13

Then, linear error propagation provides the full covariance matrix for strain-rate components for a given smoothing parameter, α:

$$\mathbf{\Sigma}_{\varepsilon,\alpha} = \mathbf{G}_\varepsilon \mathbf{\Sigma}_\alpha \mathbf{G}_\varepsilon^T$$

Equation 3.14

The posterior probability of strain rate-given data and smoothing parameter α is a Gaussian distribution:

$$p(\varepsilon|\mathbf{v},\alpha) = (2\pi)^{-k/2} \det\left(\mathbf{\Sigma}_{\varepsilon,\alpha}\right) \exp\left\{-0.5\,(\varepsilon-\varepsilon_\alpha)^T\,\mathbf{\Sigma}_{\varepsilon,\alpha}^{-1}\,(\varepsilon-\varepsilon_\alpha)\right\}$$

Equation 3.15

To account for the unknown smoothing parameter α, we want to integrate over a range of values for α. We can write the joint distribution for strain rate, ε and α given the data with the identity:

$$p(\varepsilon,\alpha|\mathbf{v}) = p(\varepsilon|\alpha,\mathbf{v})p(\alpha|\mathbf{v})$$

Equation 3.16

where the first distribution on the right side is Equation 3.15 and the second distribution is the posterior distribution of α-given data. Then, the posterior distribution of strain rate for all alpha values is obtained by marginalising Equation 3.16 over α

$$p(\varepsilon|\mathbf{v}) = \int_{-\infty}^{\infty} p(\varepsilon|\alpha,\mathbf{v})p(\alpha|\mathbf{v})d\alpha$$

Equation 3.17

Fukuda and Johnson (2010) presented a Monte Carlo method for estimating p(α|v) and p(ε|v) for similar damped least squares inversion problems. Here, we take a simpler, but more subjective, approach and assume that all α values within a range are equally likely, that is, we assume p(α|v) is a uniform distribution over an interval. We identify the interval of equally likely α values by conducting a series of damped inversions (Equations 3.11 and 3.12) for a range of α values and identify the interval over which the reduced χ^2 value is between 0.9 and 1.2. This provides a range of solutions from relatively rough (small α, low reduced χ^2) to relatively smooth (larger α, higher reduced χ^2) that fit the data nearly equally well and, on average, within about one standard deviation of the measurement error. The posterior distribution, p(ε|v), is approximated with discrete samples, similar to a Markov Chain Monte Carlo (MCMC) method; however, we do not need MCMC sampling methods. For each of 20 α values, we generate 100 realisations of p(ε|v,α) by drawing random samples from the posterior Gaussian distribution (Equation 3.15). These 2000 samples together represent samples (or realisations) of the posterior distribution p(ε|v).

3.1.3 VELMAP

VELMAP, which is based on Wang and Wright (2012; also see Weiss et al. 2020), uses linear least squares to solve for the 3D velocity field that best fits the observed GNSS velocity field. The method follows England and Molnar (1997, 2005) and assumes that the surface velocities vary linearly with latitude and longitude within each triangular element of the input mesh (i.e. strain rate is constant within each element). In comparison to the body-force and VDoHS methods, VELMAP does not have any implied elasticity assumption.

The velocity in the interior of each triangle is related to the velocity at the vertices by:

$$U = \sum_{m=1}^{3} N_m u_m$$

Equation 3.18

where u_m is the velocity of vertex and m and N_m are interpolation functions given by:

$$N_i = a_i + b_i\phi + c_i\theta$$

Equation 3.19

where ϕ and θ are the longitude and latitude, respectively,

$$a_1 = (\phi_2\theta_3 - \phi_3\theta_2)/\Delta$$

$$b_1 = (\theta_2 - \theta_3)/\Delta$$

$$c_1 = (\phi_3 - \phi_2)/\Delta$$

and

$$\Delta = \phi_1(\theta_2 - \theta_2) + \phi_2(\theta_3 - \theta_1) + \phi_3(\theta_1 - \theta_2$$

Equation 3.21

Using the same mesh described earlier, the GPS observations d_{gps} can be related to the unknown velocities, v, at the vertices via

$$\begin{bmatrix} \mathbf{G}_{gps} \\ \kappa^2\nabla^2 \end{bmatrix} \mathbf{v} = \begin{bmatrix} \mathbf{d}_{gps} \\ 0 \end{bmatrix}$$

Equation 3.22

where G_{gps} is the design matrix composed of the interpolation kernels for GPS velocities at the triangular nodes. ∇^2 is the Laplacian smoothing operator approximated by a scale-dependent umbrella operator (Desbrun et al. 1999), the weight of which is controlled by κ^2 (which functions the same as α in the body-force method). The velocities are solved for using a biconjugate gradient method weighted by a diagonal matrix containing the formal uncertainties of GPS data. As a result of the smoothing factor, the best-fit velocity field depends on the smoothing factor that we select. Traditionally, a trade-off curve of weighted misfit and solution roughness, or a Bayesian selection method, is used to find a value that has low misfit but is not too rough. To account for uncertainties in both the data and choice of smoothing factor, we perform a bootstrapping procedure on the input velocity field, as well as randomly selecting the smoothing factor. Due to the large variation in the fitted velocity field across smoothing factors, we initially select a value that provides a comparable misfit to the velocities as the VDoHS method. Once selected, we invert each of the 1000 bootstrapped datasets, randomly selecting a smoothing value within ±5% of our preferred value, providing 1000 estimates of the velocity field. This approach is similar to the probabilistic method for selection of the smoothing weighting described in the above section for the body-force method. Both approaches allow for some randomisation of the smoothing parameter to

propagate through to the uncertainties in estimated strain rates. To estimate the strain field associated with each velocity realisation, we use the spherical approximation equations of Savage et al. (2001).

3.1.4 Geostatistics

The geostatistical method is based on kriging for interpolation, which requires estimation of the spatial structure in the GNSS velocity field. We use variogram analysis to estimate a spatial structure function for each velocity component and to populate a full covariance matrix $\boldsymbol{\Sigma}$ that captures the spatial correlations between observation locations (e.g. Chiles and Delfiner 2009). Geostatistics is a weighted average approach, similar to inverse-distance weighting but where the weights are calculated using the spatial covariance matrix. The kriging system solves for optimal (in the least-squares sense) weights $\boldsymbol{\lambda}$, where the estimate at a new location $Z^*(x_0)$ is given by the weighted average of the observations z:

$$Z^*(\bar{x}_0) = \sum_{i=1}^{N} \lambda_i z(\bar{x}_i) = \bar{\lambda}^T \bar{z}$$

Equation 3.23

and the weights $\boldsymbol{\lambda}$ are found through solving the following system:

$$\begin{bmatrix} \Sigma & \mathbf{1} \\ \mathbf{1}^T & 0 \end{bmatrix} \begin{bmatrix} \lambda \\ -\nu \end{bmatrix} = \begin{bmatrix} \sigma_0 \\ 1 \end{bmatrix}$$

Equation 3.24

where $\boldsymbol{\Sigma}$ is an NxN matrix of covariances between the observation locations, $\boldsymbol{\sigma 0}$ is an N x 1 vector of covariances between the observed locations and the new estimation location and *1* is an N x 1 vector of ones. The system is solved for the vector of weights $\boldsymbol{\lambda}$ and the Lagrange multiplier $-\boldsymbol{\nu}$. The weights are substituted into Equation 3.23, while $\boldsymbol{\nu}$ is part of the uncertainty calculation:

$$\sigma^2_{Z^*} = \sigma^2_z - \lambda^T \sigma_0 + \nu$$

Equation 3.25

where $\boldsymbol{\sigma}$z is the data variance. Equation 3.24 can be set up to solve for all estimation points, interpolating a whole grid of points at once.

We use Ordinary Kriging (OK), which assumes second-order stationary fields. We remove a long-wavelength trend before calculating the variogram. Figure 3.9 shows example semivariogram plots for each velocity component, where the range represents the spatial correlation length scale, the nugget is the pointwise variance of the field (i.e. velocity uncertainties) and the sill represents the overall variance of the field. The variogram model is used to populate the covariance matrix $\boldsymbol{\Sigma}$, where element c_{ij} is the spatial covariance between stations *i* and *j*. We use a Gaussian model for the spatial covariance function, but other models such as an exponential or Matern model are also possible (e.g. Wackernagel 1995; Chiles and Delfiner 2009). Our choice of a Gaussian model to represent the spatial structure is because it assumes that the underlying field is both spatially continuous and differentiable, while the exponential and Matern models do not guarantee a point-wise differentiable field. Extrapolating to areas without data, OK reverts to the mean as the best estimate of a point.

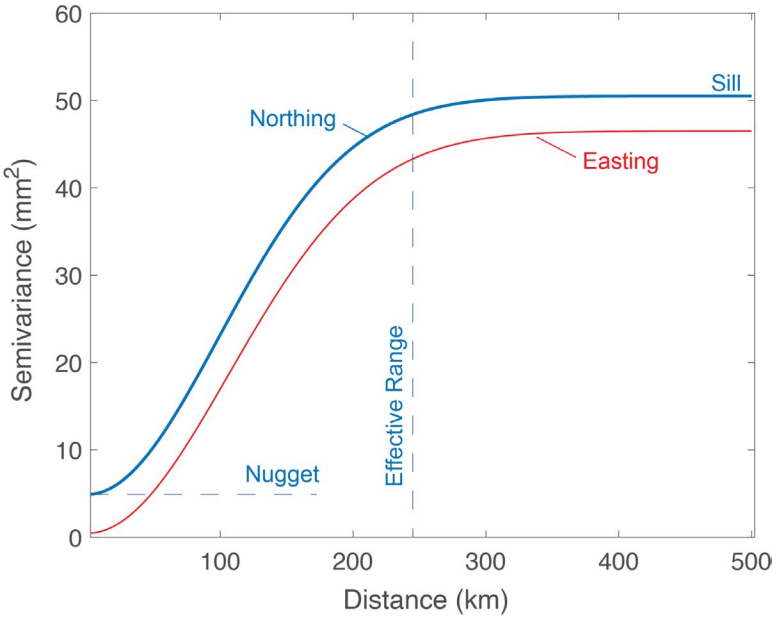

Figure 3.3 Variograms for New Zealand data. There are two variograms, one for each velocity component, as shown. The sill, range and nugget are labelled for the Northing component variogram.

Once the covariance is specified, realisations of the random field are generated by multiplying the Cholesky factor of the covariance matrix by a vector drawn from a standard normal distribution. This initial field $z_u(x)$ is 'unconditioned', that is, it is simply a random field with spatial correlation equal to the GNSS observations but does not necessarily fit the data. In a second step, the realisation is then conditioned on the observations $z(x)$ by solving for and adding a component to the field needed to fit the data:

$$\mathbf{v}_{c,k}(x_0) = \mathbf{v}_{u,k}(x_0) + \lambda^T(\mathbf{v}(x_i) - \mathbf{v}_{u,k}(x_i)) \qquad \text{Equation 3.26}$$

where $v_{c,k}(x_0)$ is the kth conditioned realisation of the velocity v = [v_{east}, v_{north}], located at x_0, and λ are weights obtained using the kriging equations (Equation 3.26). The mean and standard deviation of the maximum shear strain rate and dilatation rate for all realisations are shown in Figure 3.10, and Figure 3.11 shows the same results with the Hikurangi signal removed. Note that, in locations without strong data constraints (i.e. offshore), the mean of the maximum shear strain-rate field will not be zero because maximum shear is a strictly non-negative quantity.

3.1.5 Results

Results for all four methods are shown in Figures 3.4–3.7. Figure 3.4 shows the maximum shear strain rate estimated from each method, retaining the Hikurangi signal, and the corresponding uncertainty. Figure 3.5 shows the dilation rates for each method. Figures 3.6 and 3.7 show the same results, removing the Hikurangi signal.

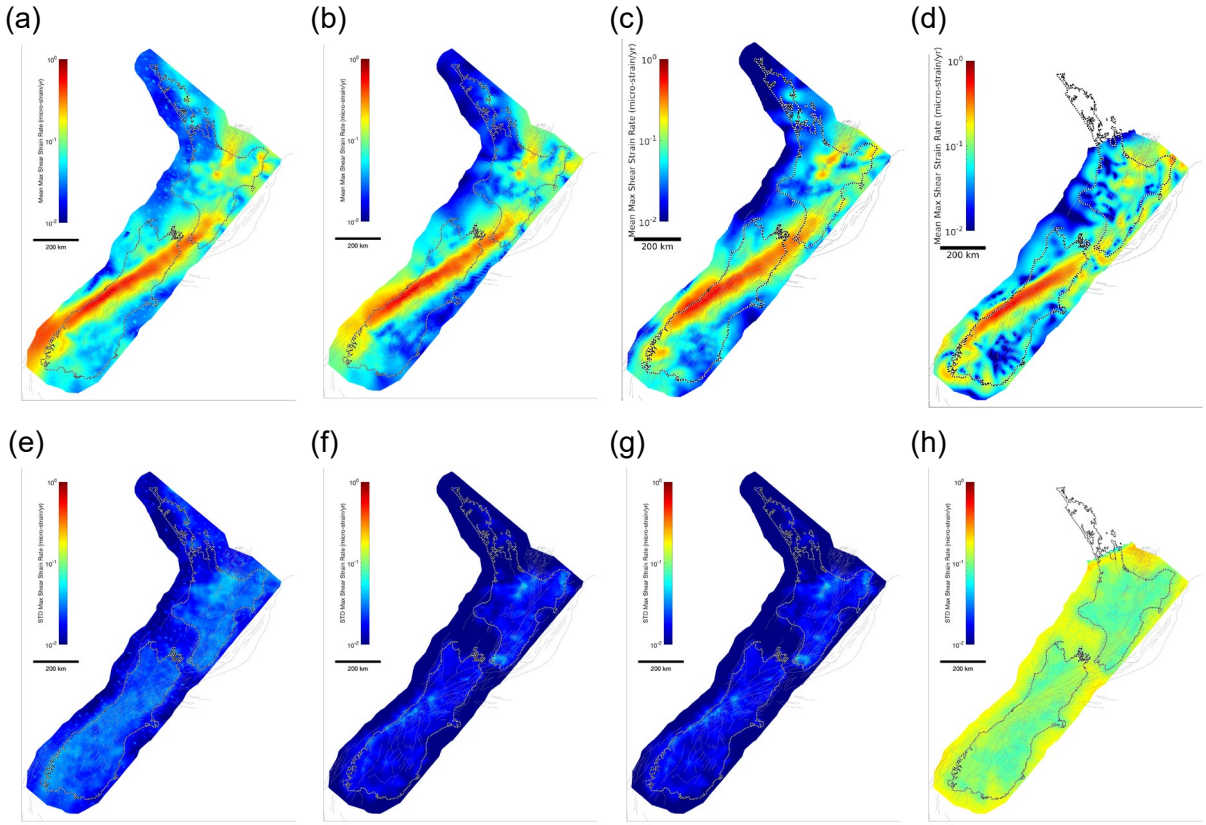

Figure 3.4 (a–d) Maximum shear strain rate retaining the Hikurangi signal and (e–h) corresponding uncertainty for the VDoHS (a, e), body-force (b, f), VELMAP (c, g) and geostatistical (d, g) methods.

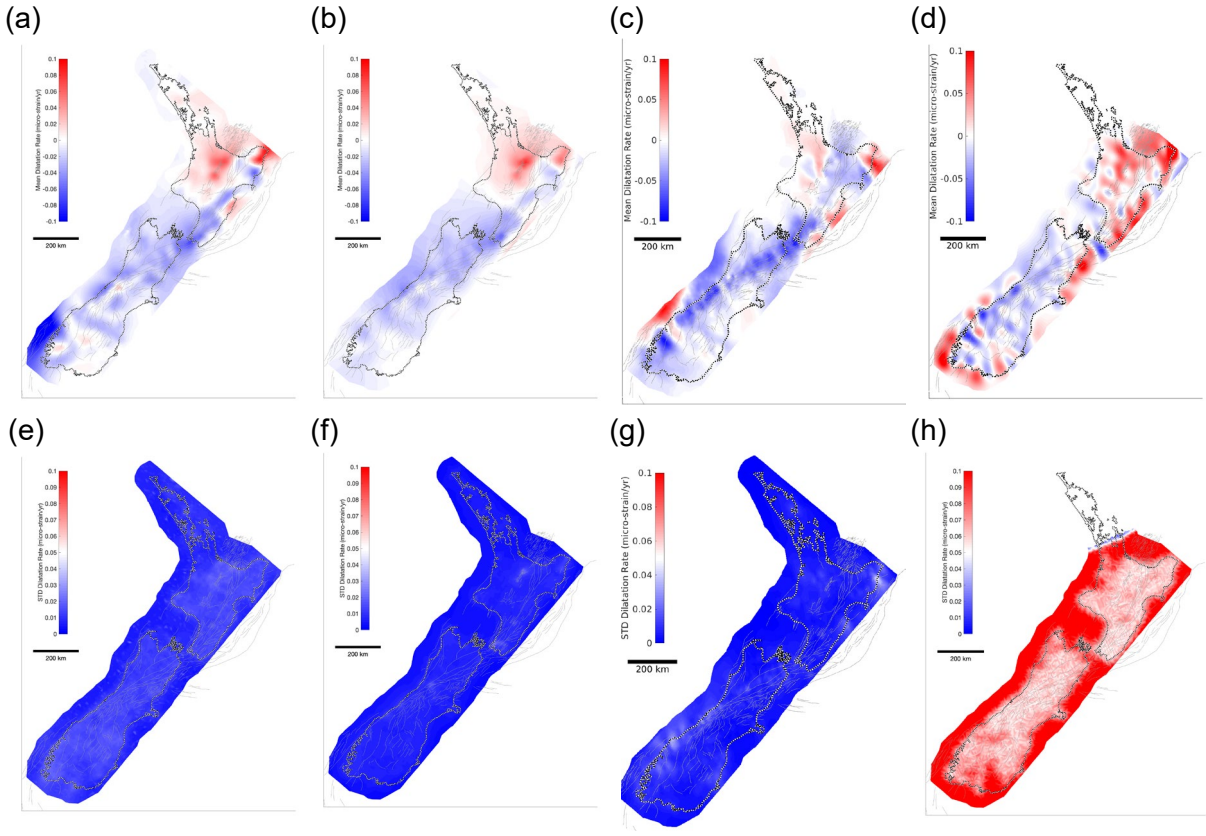

Figure 3.5 (a–d) Dilatation rate and corresponding uncertainty (e–h), retaining the Hikurangi signal, for the VDoHS (a, e), body-force (b, f), VELMAP (c, g) and geostatistical (d, g) methods.

Comparing figures for the VDoHS and body-force methods above, note that the maximum shear strain rate and dilatation rate are very similar between the two methods. This results from a very similar theoretical basis for the two methods (both assume an elastic thin plate and damp oscillations using gradient regularisation), while the actual calculation to get strain rate is different (Finite Elements versus analytical Green's function calculation).

The geostatistical method has significantly higher uncertainties than the other methods, particularly offshore. The reason for this is because the realisations are drawn from a Gaussian distribution constrained by the GNSS observations and the spatial structure function estimated in the variogram step. Thus, a query point located offshore, with no nearby stations to constrain the velocity there, will have the maximum uncertainty based on the observed variance of the velocities, not the velocity uncertainties. In comparison, the other methods penalise the magnitude of the velocity gradients such that, away from the GNSS observations, the velocities are estimated to be as low as possible.

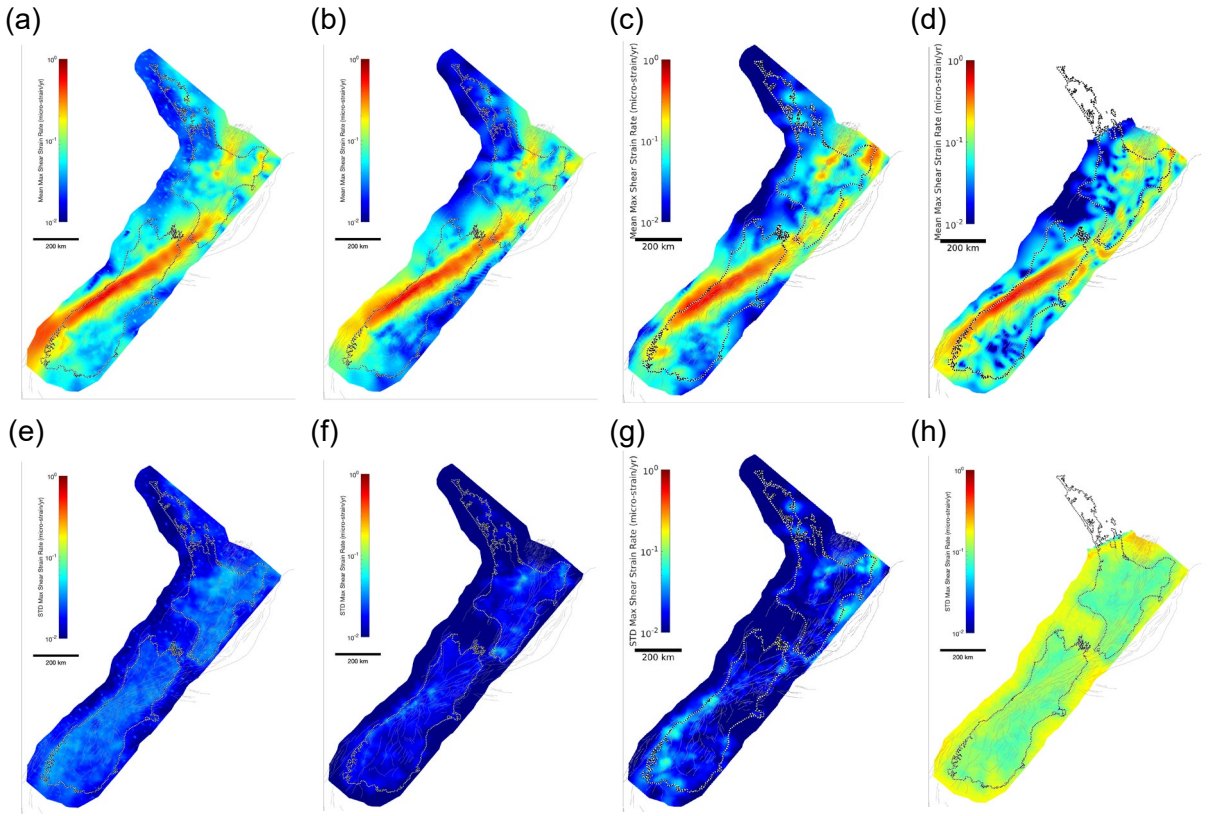

Figure 3.6 (a–d) Maximum shear strain rate removing the Hikurangi signal and (e–h) corresponding uncertainty for the VDoHS (a, e), body-force (b, f), VELMAP (c, g) and geostatistical (d, g) method.

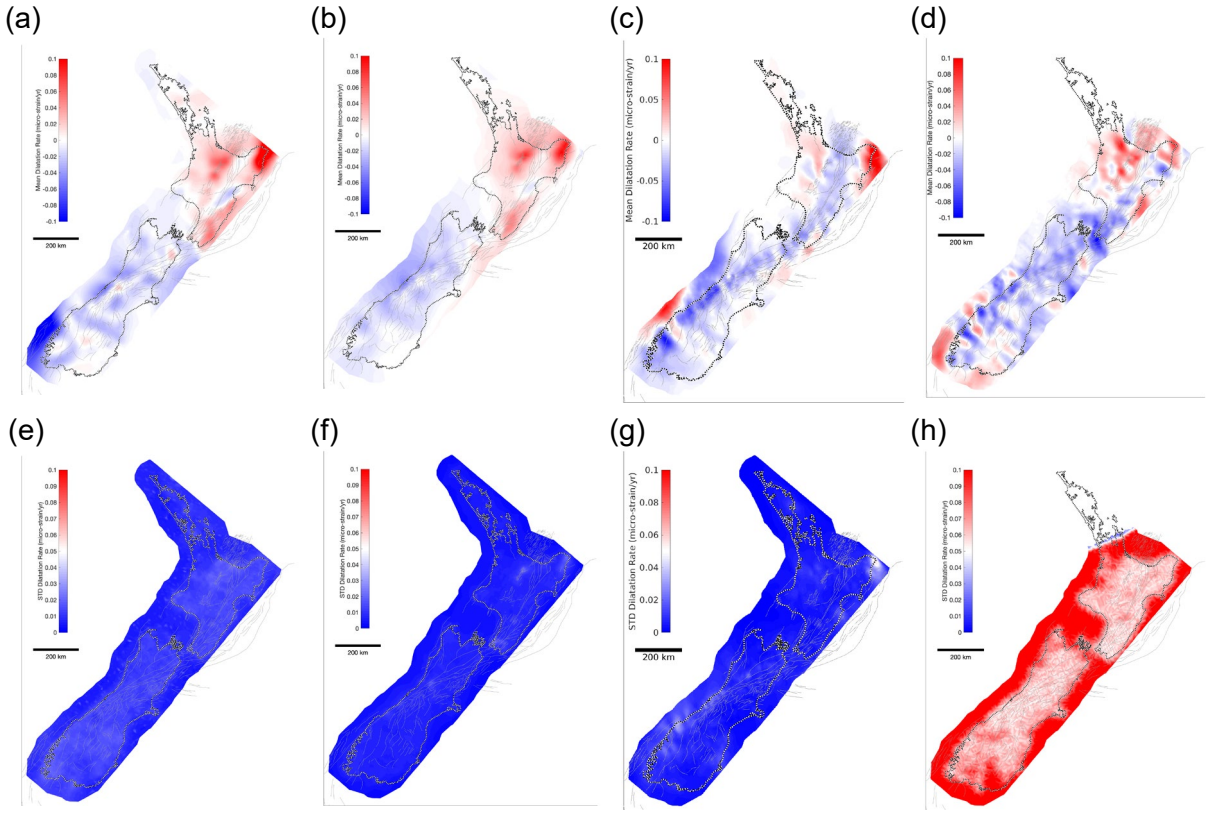

Figure 3.7 (a–d) Dilatation rate removing the Hikurangi signal and (e–h) corresponding uncertainty for the VDoHS (a, e), body-force (b, f), VELMAP (c, g) and geostatistical (d, g) methods.

3.2 Combined Strain-Rate Field

We calculate the mean strain-rate field using the four methods and show the results below. We show two combinations: the first is using equal weights for all four methods (Figure 3.8), except in Northland, where there is no geostatistical solution and we weight equally the other three methods. The uncertainties are similarly weighted and combined using standard linear error propagation.

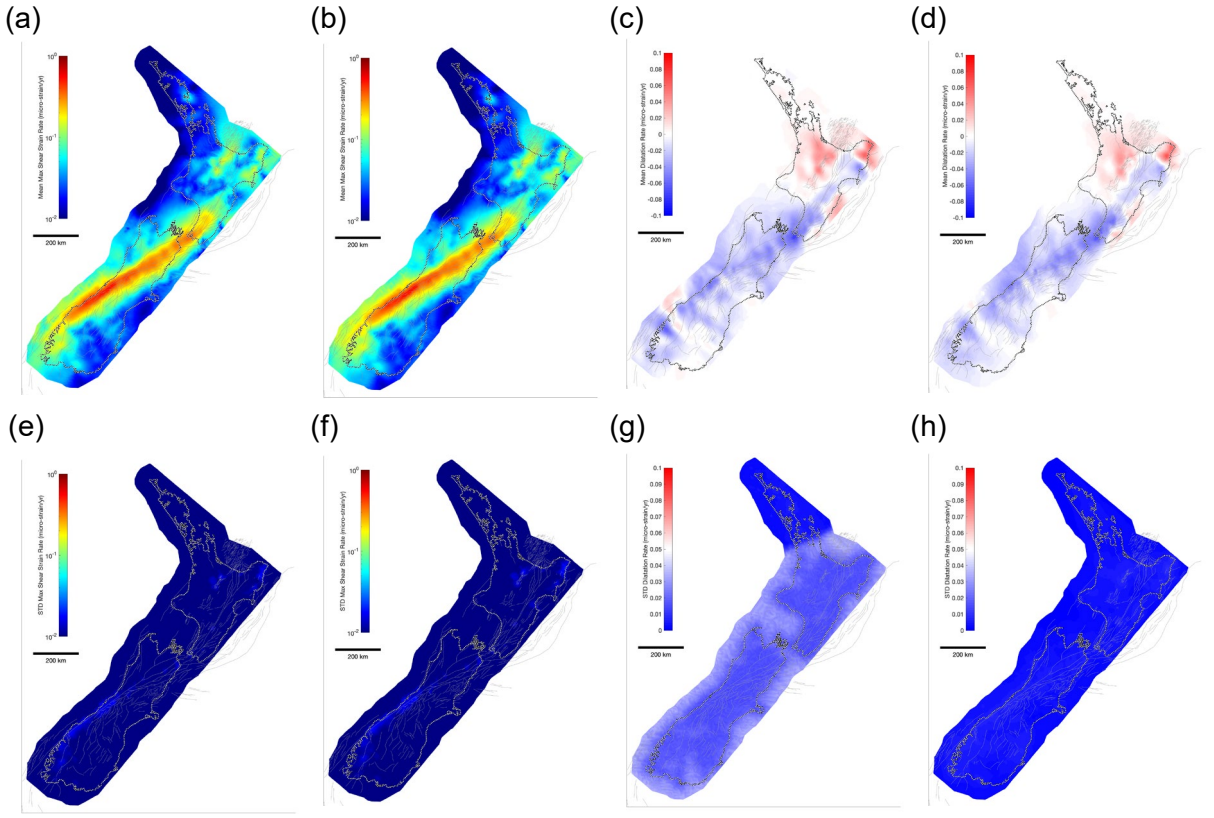

Figure 3.8 Maximum shear strain rate (a–b) and dilatation rate (c–d) with uncertainties (e–h) obtained by combining the four strain-rate methods, with the Hikurangi signal retained. (a, c) and (e, g) are obtained using equal weights on each method; (b, d) and (f, h) are obtained by weighting each map by its uncertainty.

The second method of combination is to weight each method by its own uncertainty. This has the disadvantage that if the uncertainty is under-estimated for a method, the weight assigned to that method will be disproportionately high in the result. The maximum shear strain rate and dilatation results are shown in Figure 3.9. Pixels are individually weighted, so the weights for a given method vary spatially across the domain. Mean weights averaged across the region are approximately 0.131, 0.406, 0.457, and 0.005 for the VDoHS, body force, VELMAP, and geostatistical methods, respectively, so the VELMAP method on average has the highest weight in the weighted combination, and the two elastic thin-sheet methods (VDoHS and body forces) have a combined weight comparable to the VELMAP weight.

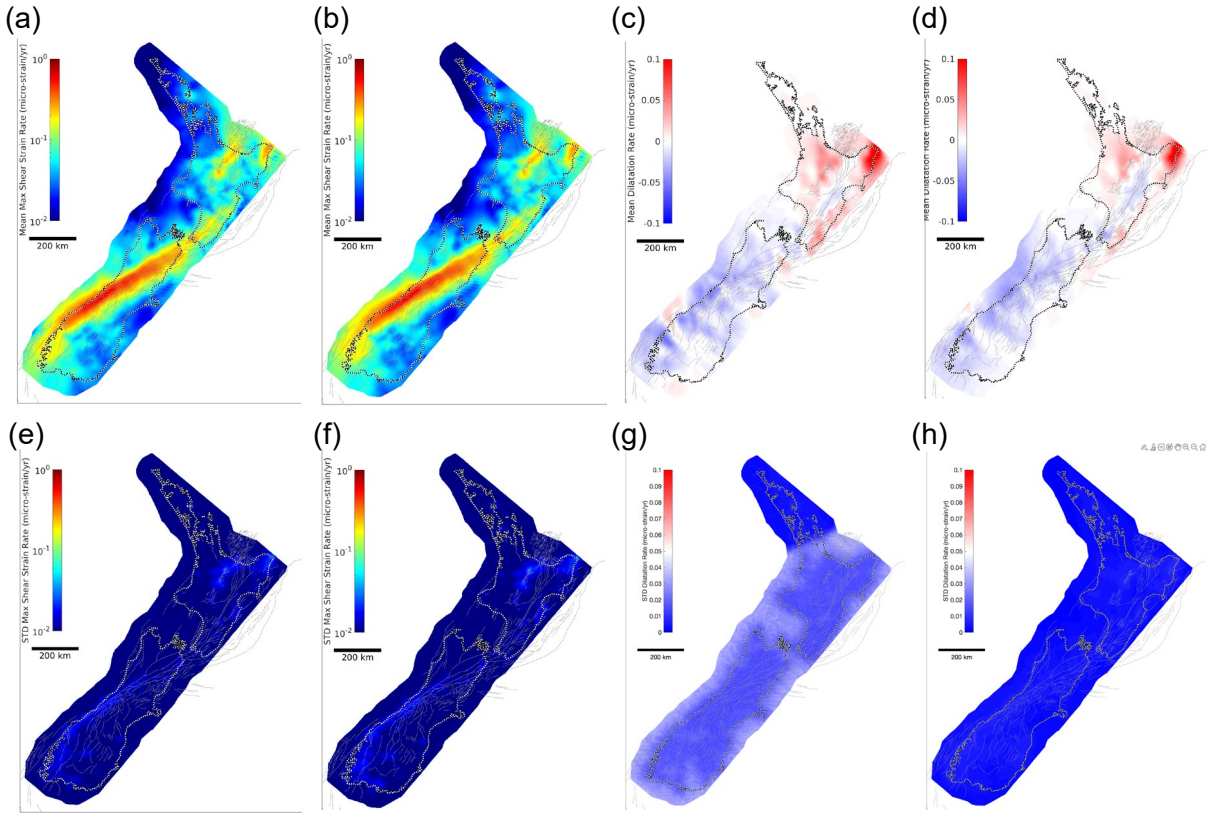

Figure 3.9 Maximum shear strain rate (a–b) and dilatation rate (c–d) with uncertainties (e–h) obtained by combining the four strain-rate methods, with the Hikurangi signal removed. (a, c) and (e, g) are obtained using equal weights on each method; (b, d) and (f, h) are obtained by weighting each map by its uncertainty.

We can remove the mean strain-rate field and compare residuals across the four methods. Figure 3.10 shows the residual maximum shear strain rate and dilatation rate for the methods. Unsurprisingly, the largest deviations from the mean strain-rate field occur offshore where there are no data constraints and within the high strain-rate belts. The geostatistics model shows the least systematic deviations from the mean, whereas the VELMAP model shows the most systematic deviations, especially along the Alpine Fault strain-rate belt.

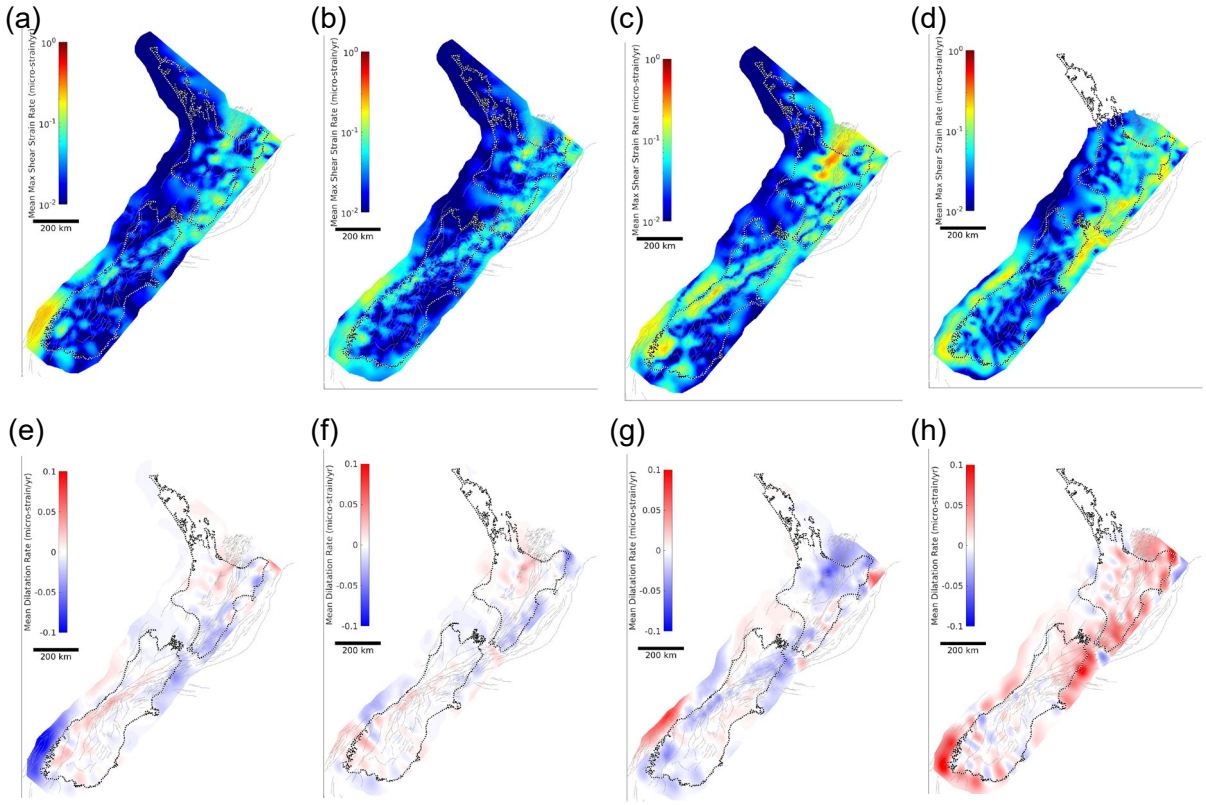

Figure 3.10 Residual maximum shear strain rate (a–d) and dilatation rate (e–h) for each of the four methods after removing the mean (equal weights) model, with the Hikurangi signal retained. Order from left to right is VDoHS, body forces, VELMAP and geostatistics.

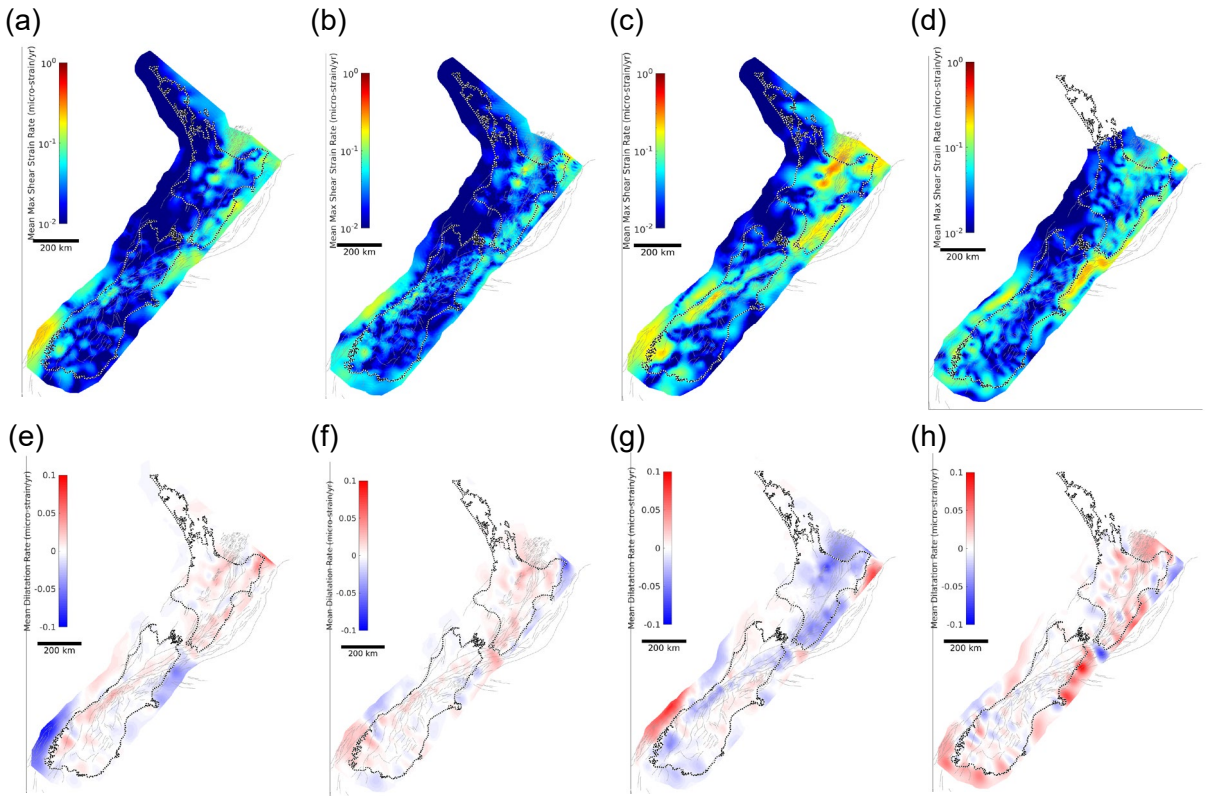

Figure 3.11 Residual maximum shear strain rate (a–d) and dilatation rate (e–h) for each of the four methods after removing the mean (equal weights) model, with the Hikurangi signal removed. Order from left to right is VDoHS, body forces, VELMAP and geostatistics.

3.3 Faulting Style Inferred Based on the Four Strain-Rate Methods and Comparison to the Geologic Faulting Style

Faulting style from geologic information is shown in Figure 3.12 (Seebeck et al. 2022). Style can also be inferred from strain rates using an eigenvector decomposition to determine principal strain-rate directions and magnitudes. Strain-rate style may not reflect faulting style because the instantaneous strain rate does not necessarily reflect the overall (i.e. absolute) long-term stress state in the crust. Using the mean strain-rate fields from each of the four methods described above, we show strain-rate tensors and style (contraction, extension, shear) implied by the strain tensors in Figure 3.13. Here, strain-rate style is defined in terms of principal strain rates ($\varepsilon_1+\varepsilon_3$)/ ($|\varepsilon_1|+|\varepsilon_3|$) and ranges from -1 to +1. The four methods result in different style maps, particularly at short to intermediate wavelengths. The Alpine Fault zone region is consistently strike-slip faulting, but other regions can be different or even opposite strain styles. The geostatistical method has larger uncertainties than the other method (consistent with the other geostatistical results shown in Figures 3.10–3.11), resulting in a larger area of shear strain style.

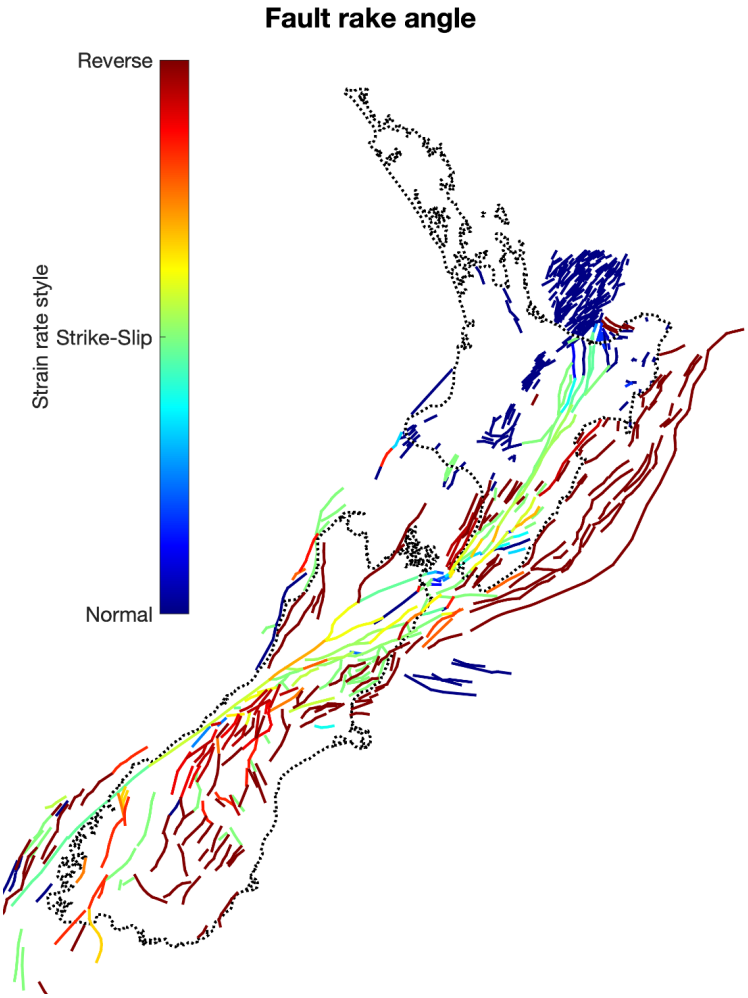

Figure 3.12 Faulting style inferred from geology (Seebeck et al. 2022).

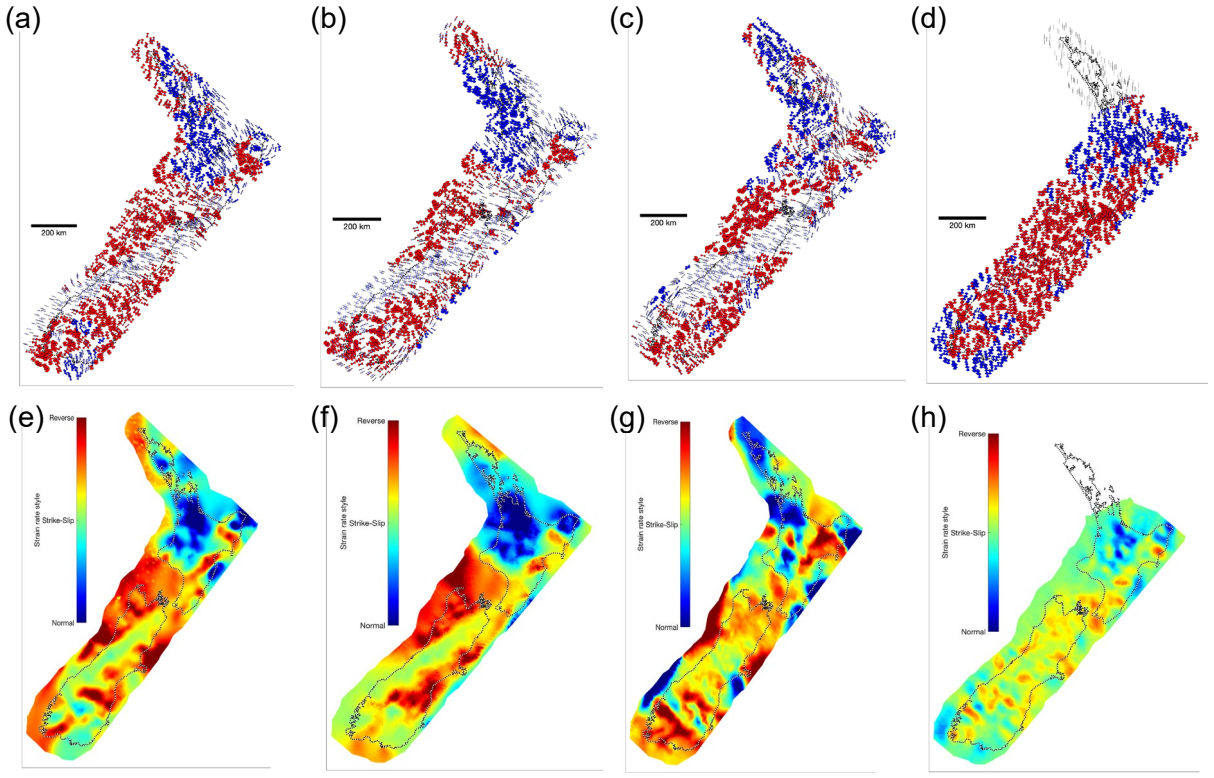

Figure 3.13 Inferred strain-rate direction and equivalent faulting style for each of the four methods. The Hikurangi signal has been removed from these estimates. Order from left to right is VDoHS, body forces, VELMAP and geostatistics. Top: Strain rate tensors represented as wedge diagrams, where the width of the wedge represents the 2-sigma uncertainty in direction propagated from the uncertainties in the strain rate components. Bottom: Inferred style based on the strain rate tensors.

3.4 Strain-Rate Method Comparison

Analysis of the results from the different strain-rate methods shows that there are strong similarities, as well as some interesting differences, between the mean fields of the four strain-rate methods. The mean maximum shear strain rate is nearly identical across all methods, while the dilatation and strain-rate style are fairly different. In particular, the dilatation rates appear to show the impact of different types of spatial interpolation methods, with VDoHS and body force results being relatively smooth, while VELMAP and geostatistics are comparatively rougher but with different characteristics. VELMAP shows north–south undulations in the dilatation rate, which presumably are a reflection of the triangle-based interpolation functions, while the geostatistical method is more ‘blobby’, reflecting the radial basis functions implied by the use of a distance-based covariance matrix. The residual plots in Figures 3.10–3.11 also differ. The residuals in the on-shore maximum shear strain rate occur mainly at wavelengths shorter than the inter-station spacing and thus illuminate the smallest deformation scale resolvable by the data. Off-shore, differences reflect differences in boundary condition assumptions.

The uncertainties of the four methods are calculated in quite different ways. It is computationally challenging to calculate robust uncertainties for the VDoHS approach (see discussion in Haines and Wallace [2020] and Árnadóttir et al. [2018]), and the quoted uncertainties from that method are based on data uncertainties and are strongly influenced by the distance between GNSS stations. The body-force method uses linear propagation of the formal GNSS uncertainties and regularisation variance. VELMAP uses a bootstrapping approach. The geostatistical method assumes that the uncertainty can be represented as a spatially correlated Gaussian random field with a variance (in absence of nearby data) equal to the variance of the velocity

observations of the entire field. It is worth comparing the residuals of the four methods to the uncertainties of each individual method. On-shore, the maximum shear strain residuals are comparable to the uncertainties, while off-shore and in data-poor areas the elastic thin-plate and VELMAP solutions have very small uncertainties compared to the geostatistical method and residuals between methods. The uncertainties of the VDoHS, body force and VELMAP methods are small relative to the differences between methods, while the geostatistical method has uncertainty larger than the differences. Thus, the uncertainty for a given strain-rate method cannot be related to differences between methods.

This conclusion, that the uncertainties within a method are not related to between-method uncertainty, is confirmed by Figure 3.14, which shows the spatially averaged dilatation and maximum shear strain rates (i.e. per realisation) for all realisations for each of the four methods. Each method is clustered by itself and is separate from the other three. The geostatistical method is most different because the higher uncertainties result in overall higher average strain rates, while the other three methods all tend to go to zero strain rate offshore, which reduces the overall mean strain per realisation. In particular, the body-force method has the lowest overall average, consistent with the figures shown above, suggesting it to give the smoothest results.

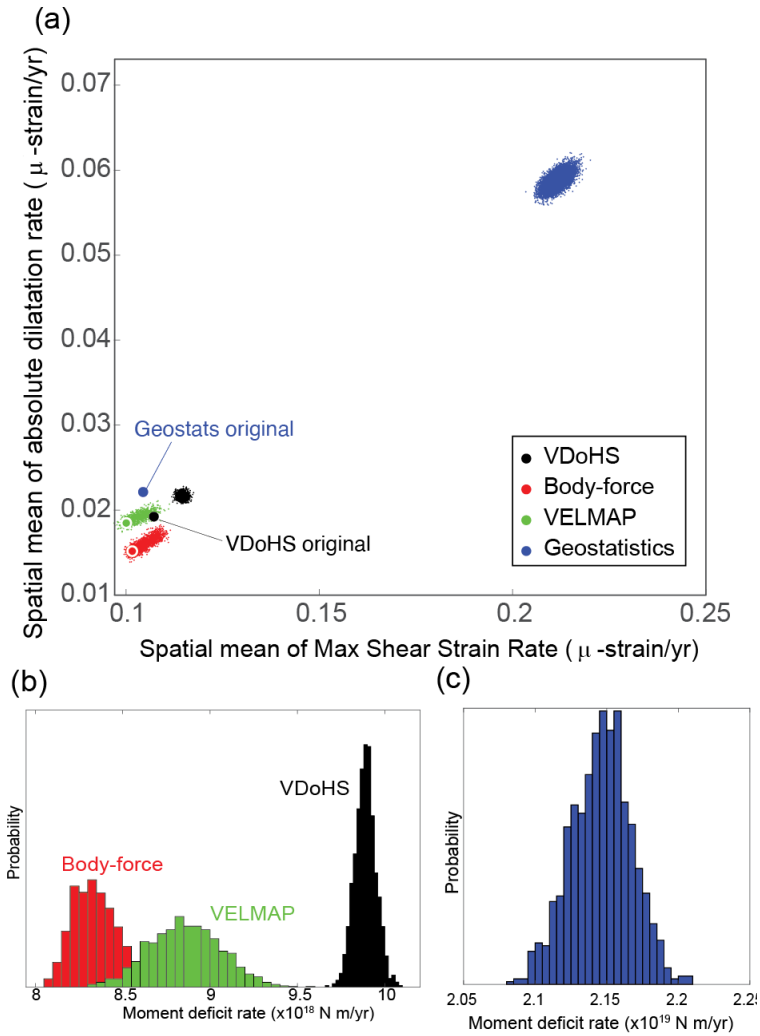

Figure 3.14 Comparison of the spatially averaged dilatation and maximum shear strain rates from each of the four methods. The Hikurangi strain signal has not been removed from these realisations. (a) The small dots represent the spatially averaged absolute dilatation rate (y-axis) versus the spatially averaged maximum shear strain rate (x-axis) for the individual realisations, coloured by method. Large dots represent the mean models for VELMAP and the body-force methods, the kriging result for the geostatistical method and the original (non-perturbed) result for the VDoHS method. (b–c) Total moment rate implied by the first 1000 realisations from each of the four methods.

These values are calculated using fixed geometry; the real seismogenic depths, etc., will vary spatially but be the same across models. We use a grid node area of 16 square km, a seismogenic depth of 15 km, and a constant shear modulus of 30 GPa. Figure 3.14 shows the distributions in total moment accumulation rate computed for each strain-rate model using the Savage and Simpson (1997) conversion from strain rate to moment rate (Equations 3.4 and 3.5). This calculation is similar to simply scaling the spatially averaged maximum shear strain rate; thus, we see the overlapping body force and VELMAP moment rates and the slightly higher moment rates from the VDoHS strain rates. The moment rates implied by the geostatistics strain rates are approximately a factor of two higher than the other methods. The geostatistics moments are higher because of a combination of the large uncertainties in strain rates (relatively large deviations from the mean strain rates across all realisations) and the absolute value in Equation 3.5 that skews the moment-rate distributions to higher values than the mean strain-rate models (the same effect is also clear in the maximum shear strain-rate distributions in Figure 3.14 that are skewed higher than the mean models).

4.0 GEODETIC SLIP DEFICIT RATE MODEL

As described previously, the principal assumption behind our slip deficit rate inversion method is that the majority of interseismic strain rate in the crust is elastic distortions attributed to interseismic coupling on crustal faults. Under this assumption, the strain-rate field is linearly related to the slip deficit rates on faults. We invert the four strain-rate maps for the spatial distribution of slip deficit rates on faults. We conduct suites of inversions with and without the geologic slip rate model as a prior on slip deficit rates. The rationale for inverting strain rates, instead of surface velocities, is that fair-field rigid plate motions and block rotations, as well as long-term fault slip rates, do not need to be accounted for in the forward model. In this section, we describe the methodology for forward and inversion models.

4.1 Slip Deficit Inversion Method

4.1.1 Construction of Slip Deficit Green's Functions

To solve for the spatial distribution of slip deficit rate on faults, we will utilise the solution for uniform slip on a rectangular dislocation in an elastic half space (Okada 1992). We represent the faults in New Zealand with a series of planar fault segments that are discretised into rectangular patches, as illustrated in Figure 4.1. The nominal patch length along strike is 10 km and varies from 5 to 15 km; the nominal down-dip width is 8 km and varies from 4 to 12 km. To construct this 3D fault model, we first approximate the surface traces of faults in the New Zealand NSHM 2022 fault model (Seebeck et al. 2022) with 10-km-long piecewise-continuous fault segments to smooth out shorter wavelength variations in fault strike. We adopt the preferred dip and rake from the fault model for each model segment. The planar fault segments are extended at constant dip from the surface to the D90 depth (i.e. the depth above which 90% of the seismicity occurs; see Ellis et al. [2021] and Seebeck et al. [2022]) in the NSHM 2022 fault model. We note that the choice of depth of the faults is a pragmatic one; we use D90 for consistency with the NSHM modeling framework. We show in Section 4.3 of this report that this choice is not critical for our estimates of slip deficit rate, and particularly the total moment rate on faults due to slip deficit rate, as the depth resolution is quite poor.

One challenge of modelling strain rates with uniform slip dislocation solutions is that the strain-rate field near the fault is highly sensitive to the spatial gradient of slip, and strain rates are in fact infinite at the edges of the dislocations. The implications of using uniform slip dislocations for modelling strain rate are illustrated in Figure 4.2, which shows the surface maximum shear strain rate for a vertical strike-slip fault. The slip deficit rate distribution is uniform over 5-km-long patches (slip deficit extends to 15 km depth) at the rates shown in Figure 4.2a. Figure 4.2b shows the resulting strain rates. Clearly, the imposed discontinuities in slip deficit rate introduce distinctive strain-rate lobes emanating from the discontinuities. To avoid these lobes, we impose continuous, linear slip gradients on faults. Figure 4.2c shows the surface maximum shear strain-rate pattern resulting from the linear slip deficit rate distribution. To get the slip rate distribution, we subdivide the uniform slip patches into many smaller patches of 0.5 km length (and 15 km deep), impose the slip rates shown in Figure 4.2a at the larger segment endpoints and impose a linear gradient between. The result of the linear tapering is a smoother surface strain-rate field without the lobes of high strain rates.

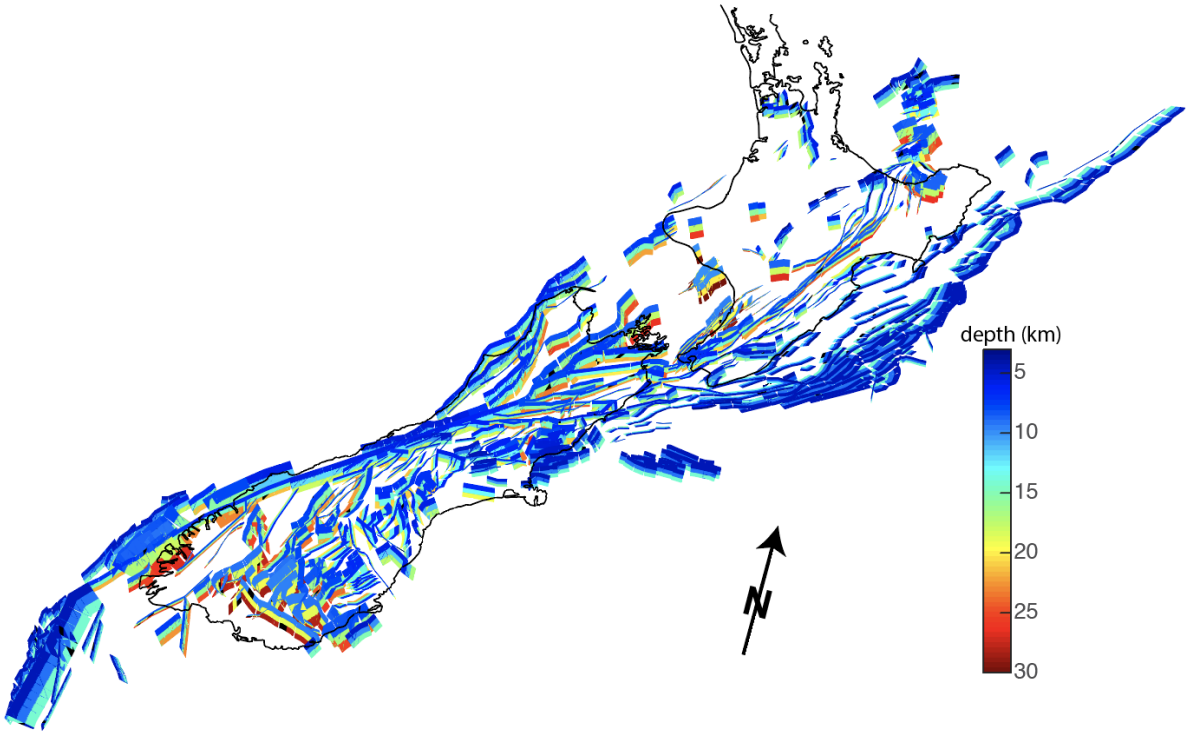

Figure 4.1 3D perspective view of rectangular fault geometry. Fault geometry is based on the New Zealand NSHM 2022 fault model. Details of construction of fault geometry in the main text. Colour shows the depth to the bottom of each rectangular slip patch.

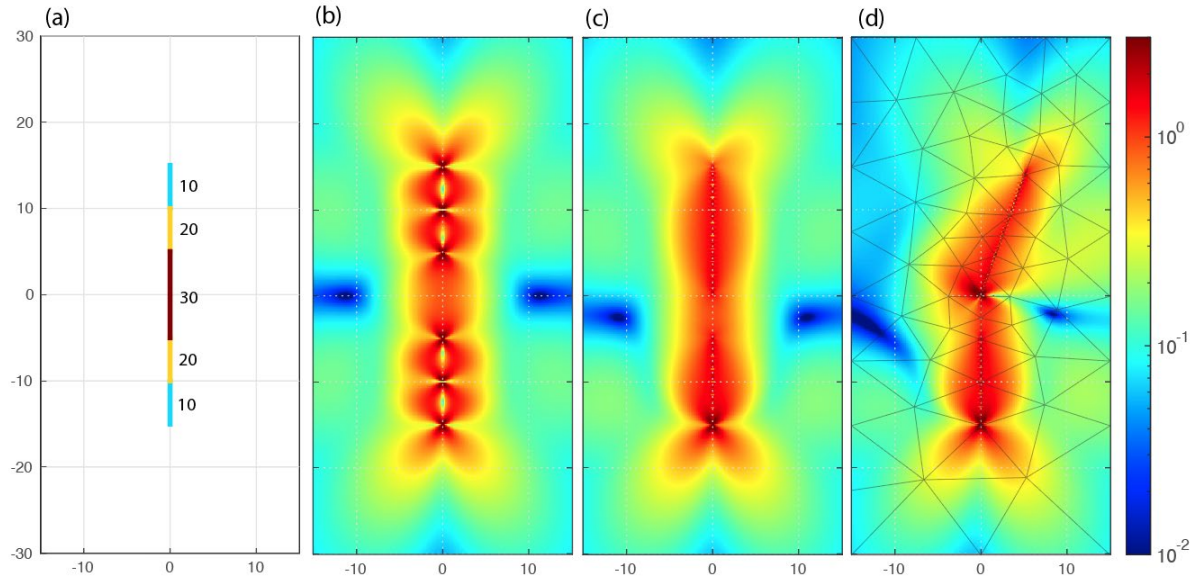

Figure 4.2 Illustration of strain-rate calculations using linearly tapered slip distributions, as described in the text. (a) Input uniform slip rate distribution (map view) on a vertical strike-slip fault extending from the surface to 15 km depth. (b) Computed maximum shear strain rate at the surface for non-tapered slip distribution (uniform slip rate over sections as illustrated in [a]). (c) Maximum shear strain rates for linearly tapered slip distribution. (d) Illustration of mesh construction used to minimise the influence of strain rate singularities due to terminations and kinks in faults.

Strain-rate singularities also arise because of discontinuities in geometry; for example, sharp bends in the fault surface. Figure 4.2d illustrates a geometry similar to Figure 4.2(a–c), but with a kink due to a 20° sudden change in strike at position (0,0). The same linearly tapered slip distribution as in Figure 4.2c is imposed. Here, the strain-rate concentration near (0,0) is due to the kink in the fault. While such strain-rate concentrations are not entirely unexpected in the crust, strain-rate concentrations associated with complex, non-planar fault geometry depend

on detailed knowledge of the fault geometry that we do not have access to. To avoid the problem of fitting smooth observed strain-rate fields with a model that contains strain-rate artifacts due to arbitrary representations of faults as recti-linear segments, we compute strain rates at the centroids of triangles in a fault-based triangular mesh, as illustrated in Figure 4.2d. The mesh is designed so that fault segment endpoints occur as nodes and fault traces occur as sides of triangles. This spacing of compute nodes minimises the influence of fault endpoints and kinks on strain-rate calculations. The mesh is constructed using the program MESH2D (Engwirda 2014) which is based on algorithms using Delaunay-refinement and Frontal-Delaunay triangulation techniques, as well as hill-climbing-type mesh optimisation.

Figure 4.3 shows the actual fault-based mesh that we have adopted for New Zealand, based on the surface trace approximations of the New Zealand NSHM 2022 fault model (Figure 4.1; Seebeck et al. 2022). The maximum edge length of triangles is 15 km along faults and 100 km at the edge of the model domain.

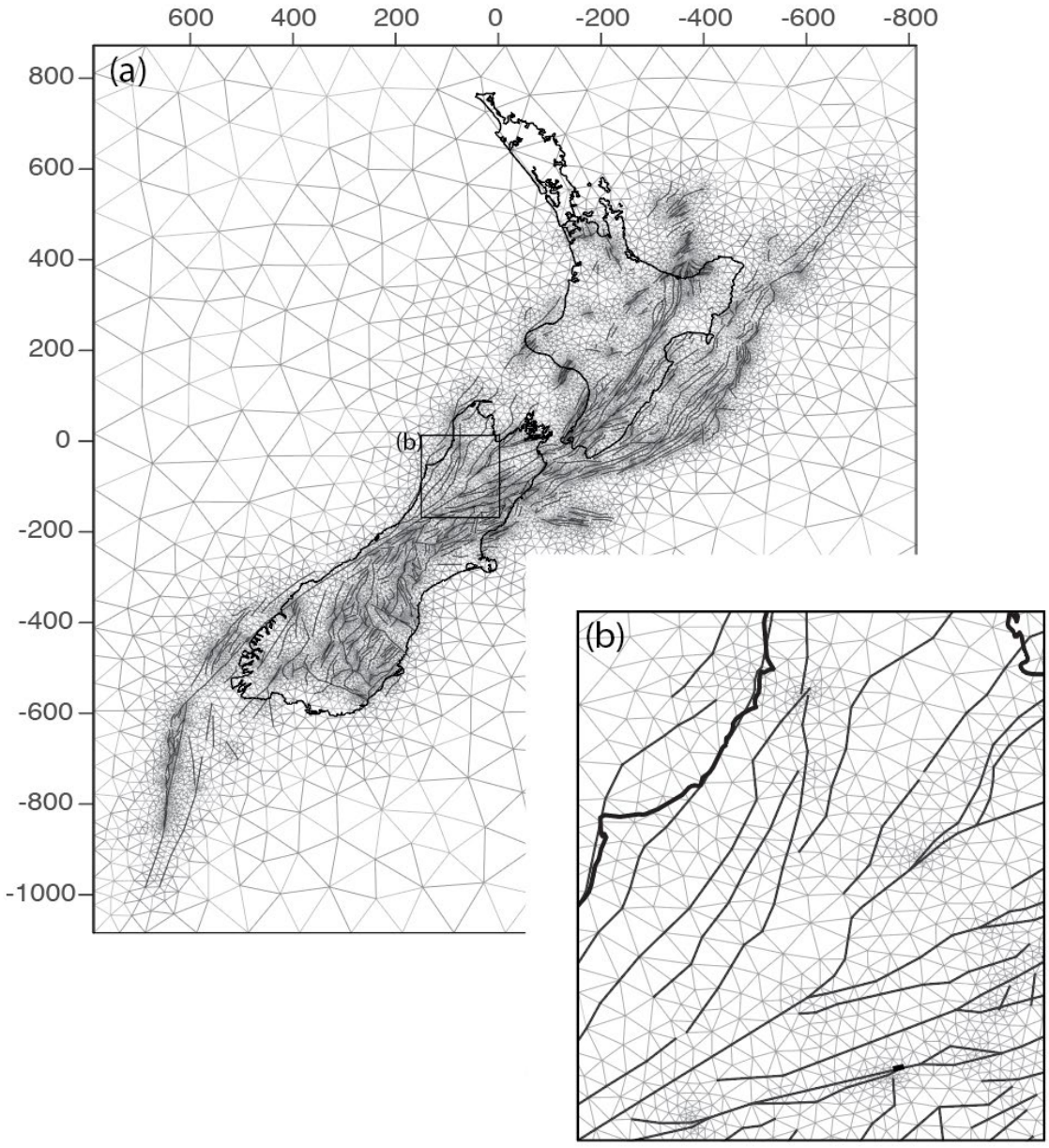

Figure 4.3 Mesh used for computing strain-rate Green's functions. Mesh size is controlled by fault trace geometry. Strains are computed at the centre of each triangular element for unit slip on each rectangular fault patch shown in Figure 4.1.

4.1.2 Geologic Constraints

Geologic constraints on slip rates are adopted from the New Zealand NSHM 2022 Geologic Deformation Model (GDM). We impose the preferred slip rake for each fault and solve for the slip deficit rate in that fixed rake direction. Slip deficit rate is therefore constrained to be a positive number (non-negativity constraint). We incorporate the preferred, upper and lower geologic slip rates in the GDM by introducing truncated Gaussian prior distributions on slip deficit rate, as illustrated in Figure 4.4. The figure illustrates the preferred, upper and lower geologic rates with distance along a fault segment. The prior slip rate at any point along the fault (shown with the red curve) is a truncated Gaussian distribution centred on the preferred geologic rate with 1-standard deviation equal to the geologic upper rate minus the lower rate. The distribution is truncated at zero at the low end and 10 times the GDM high slip rate (off-scale in Figure 4.4) at the upper end. The rationale for this choice of prior is two-fold. The Gaussian-shaped prior is convenient for use with linear error propagation, as described in detail in the following section. Secondly, the prior distribution favours the preferred geologic value but conservatively permits slip rates above and below the upper and lower rates.

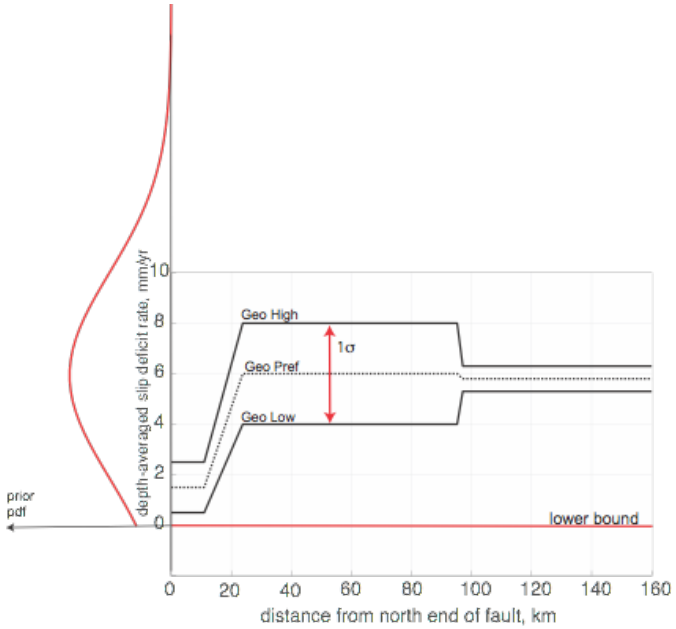

Figure 4.4 Illustration of implementation of geologic slip rate model as truncated Gaussian prior information for slip deficit rate inversions.

4.1.3 Inversion Scheme

We want to solve for the slip deficit rates on all rectangular slip patches for each of the four strain-rate maps, subject to bound constraints. The objective is to solve for the full (correlated) posterior probability distribution of slip deficit rate on patches. This inversion is conducted in two steps. We first conduct a linear inversion for slip deficit rate without bound constraints and use linear error propagation to obtain the posterior distribution. In the second step, we numerically construct the posterior distribution with bound constraints by sampling, using Monte Carlo methods.

Here, we set up the linear inversion. Let s be a vector of slip deficit rates on all patches, let d_ε be a vector of observed strain rates and let G_ε be the matrix of strain-rate Green's functions. The basic observation equation is then:

$$\mathbf{d}_\varepsilon = \mathbf{G}_\varepsilon \mathbf{s} + \epsilon \qquad \text{Equation 4.1}$$

where $\boldsymbol{\varepsilon}$ is a vector of errors, assumed to be Gaussian. We introduce the geologic slip rate constraints in two equivalent ways: as a prior distribution or as data. Let *sp* be a vector of preferred geologic slip rates on all patches and let $\sum s$ be the diagonal covariance matrix with the slip deficit rate variances on the diagonal. We also construct diagonal covariance matrices for the strain-rate data, $\sum \boldsymbol{\varepsilon}$. The full strain-rate covariance matrix for the body force and geostatistics strain-rate methods are available from strain-rate map realisations, but covariances are ignored for this inversion. If we treat the geologic constraints as data, we construct the following augmented observation equations:

$$\begin{bmatrix} \Sigma_{\varepsilon}^{-1/2}\mathbf{d}_{\varepsilon} \\ \Sigma_{s}^{-1/2}\mathbf{s}_{p} \end{bmatrix} = \begin{bmatrix} \Sigma_{\varepsilon}^{-1/2}\mathbf{G}_{\varepsilon} \\ \Sigma_{s}^{-1/2}\mathbf{I} \end{bmatrix} \mathbf{s} + \epsilon$$

Equation 4.2

To simplify notation, we write the weighted observation vector d_w on the left side of Equation 4.2 and weighted matrix G_w on the right side as:

$$\mathbf{d}_{w} = \mathbf{G}_{w}\mathbf{s} + \epsilon$$

Equation 4.3

We require that the slip deficit rate vary smoothly on neighbouring patches along fault segments by introducing the difference operator *D*, which computes differences in slip deficit rate in the along-strike and down-dip directions between patches. We then have the following system of equations to solve:

$$\begin{bmatrix} \mathbf{d}_{w} \\ \mathbf{0} \end{bmatrix} = \begin{bmatrix} \mathbf{G}_{w} \\ \alpha^{-2}\mathbf{D} \end{bmatrix} \mathbf{s} + \epsilon$$

Equation 4.4

where the smoothing parameter, α, determines the relative weight placed on fitting the data versus maintaining smoothness in slip deficit rate. Equation 4.4 can be solved using standard least squares formula. Equivalently, we can introduce the generalised inverse (e.g. Menke 2018; Aster et al. 2018):

$$\mathbf{G}^{\sharp} = \left[\mathbf{G}_{w}^{T}\mathbf{G}_{w} + \alpha^{-2}\mathbf{D}^{T}\mathbf{D}\right]^{-1}\mathbf{G}_{w}^{T}$$

Equation 4.5

and obtain the least squares solution as:

$$\mathbf{s}_{\alpha} = \mathbf{G}^{\sharp}\mathbf{d}_{w}$$

Equation 4.6

which is the best-fitting slip deficit rate distribution for a given smoothing parameter, α. The covariance matrix for slip deficit rate is then:

$$\boldsymbol{\Sigma}_{\alpha} = \mathbf{G}^{\sharp}\begin{bmatrix} \Sigma_{\varepsilon} & \mathbf{0} \\ \mathbf{0} & \Sigma_{s} \end{bmatrix}\left(\mathbf{G}^{\sharp}\right)^{T}$$

Equation 4.7

To incorporate the bound constraints on slip deficit rate, we switch notation to express the problem in terms of probability density functions. Bayes' Theorem states:

$$p(\mathbf{s}|\mathbf{d}) = p(\mathbf{d}|\mathbf{s})p(\mathbf{s})$$

Equation 4.8

where *p(s|d)* is probability density of slip deficit rate given data, *d*, *p(d|s)* is Likelihood and *p(s)* is the prior probability distribution of slip deficit rate. If we continue to view the geologic constraints as data, neglecting bound constraints, then the likelihood is:

$$p(\mathbf{d}|\mathbf{s}) \propto \exp\{-0.5\,(\mathbf{d}_w - \mathbf{G}_w\mathbf{s})^T\,(\mathbf{d}_w - \mathbf{G}_w\mathbf{s})\}$$

Equation 4.9

and the prior distribution, *p*(s), can be taken to uniform distributions. Because the relationship between data and slip deficit is linear, the Likelihood is a multivariate Gaussian distribution; we can write the distribution using the least squares solution (Equations 4.6 and 4.7):

$$p(\mathbf{d}|\mathbf{s}) \propto \exp\{-0.5\,(\mathbf{s} - \mathbf{s}_\alpha)^T\,\boldsymbol{\Sigma}_\alpha^{-1}\,(\mathbf{s} - \mathbf{s}_\alpha)\}$$

Equation 4.10

Equivalently, we can view the geologic constraints as a prior probability distribution on slip deficit rate and write the prior distribution as $p(s) = \tilde{p}(s)b(s)$, where $\tilde{p}(s)$ are Gaussian distributions and *b*(*s*) are box-car functions that truncate the Gaussian distributions. Then, we can write the posterior distribution on slip deficit rate given strain-rate data as:

$$p(\mathbf{s}|\mathbf{d}_\varepsilon) = p(\mathbf{d}_\varepsilon|\mathbf{s})\tilde{p}(\mathbf{s})b(s)$$

Equation 4.11

The Likelihood in Equation 4.11 is:

$$p(\mathbf{d}_\varepsilon|\mathbf{s}) \propto \exp\{-0.5\,(\mathbf{d}_\varepsilon - \mathbf{G}_\varepsilon\mathbf{s})^T\,(\mathbf{d}_\varepsilon - \mathbf{G}_\varepsilon\mathbf{s})\}$$

Equation 4.12

The distribution $p(d_\varepsilon|s)\tilde{p}(s)$ in Equation 4.11 is the same as distribution in Equation 4.10, which is computed using least squares and error propagation. However, the posterior distribution $p(\mathrm{s}|\mathrm{d}_\varepsilon)$ in Equation 4.11 must be obtained numerically, because of the bounds expressed in *b*(s) preclude a closed-form expression. We sample $p(\mathrm{s}|\mathrm{d}_\varepsilon)$ using the Monte Carlo Metropolis-Hastings algorithm.

Finally, we can form an aggregate posterior probability distribution of slip deficit rate by combining the discrete samples of Equation 4.11 obtained from the Monte Carlo Metropolis sampling methods for each of the four strain-rate map inversions. We form the aggregate slip deficit rate posterior probability distribution by treating each realisation from all four strain-rate maps as equally likely and forming a composite set of realisations containing all individual standard deviations, which we display as the 'combined' model in the results section below.

Figure 4.5 illustrates this method with actual results from inversion of the VELMAP strain-rate map for slip deficit rate. Here, we show posterior distributions for nearby slip patches on the closely spaced Gimmerburn and Garibaldi faults in the Otago region of the South Island, as well as joint distribution for patches on the nearby Mohaka and Ruahine faults in the North Island. The unbounded joint posterior distributions (Equation 4.10) are shown with contours in the left-side panels and blue curves in the marginal distribution plots in the centre and right-side panels. The numerically computed posterior distributions, incorporating bound constraints, are shown as 2D density plots in grey colour scale in the left-side panels and as orange curves in the marginal distribution plots. Also shown (with yellow curves) are prior probability distributions of slip deficit rate from the geologic constraints. For posterior distributions concentrated far from the bound constraints (Mohaka and Ruahine fault examples), the bounded and unbounded distributions are very similar. Note that the joint distributions are both negatively correlated, indicating a trade-off between slip deficit rates on the pairs of closely spaced faults.

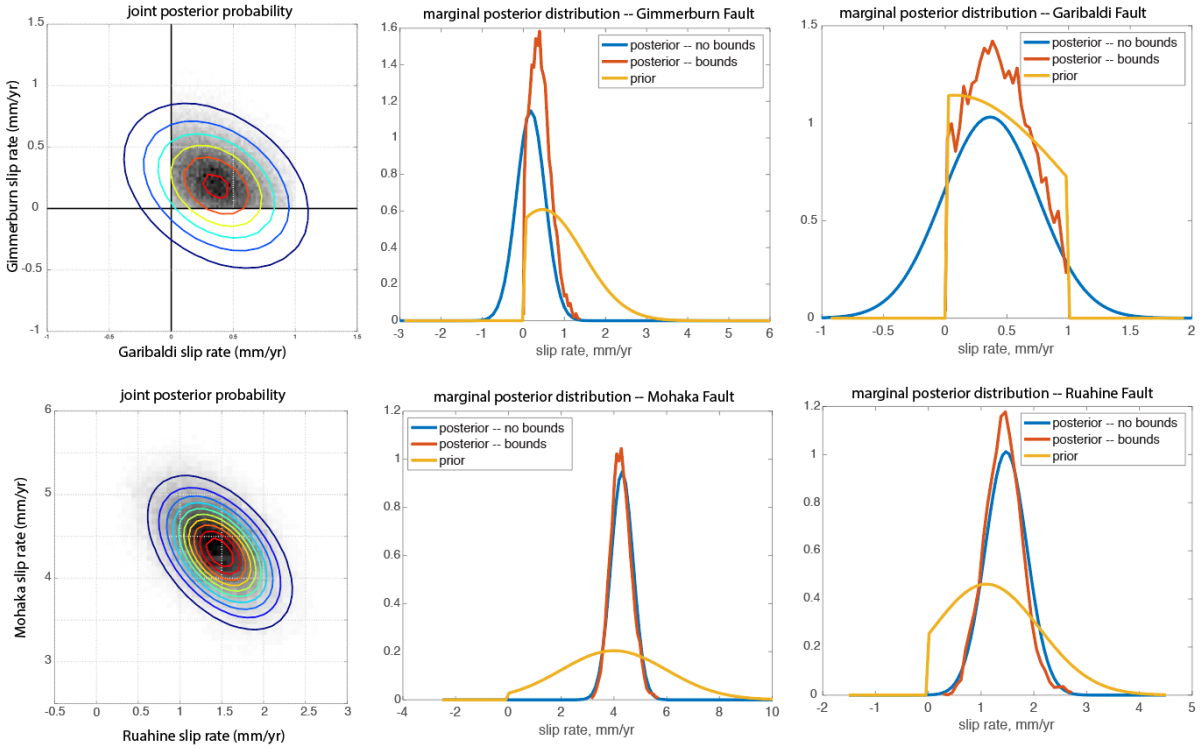

Figure 4.5 Illustration of Monte Carlo sampling of posterior slip deficit rate distributions. The unbounded joint posterior distributions (Equation 4.10) are shown with contours in the left-side panels and blue curves in the marginal distribution plots in the centre and right-side panels. Posterior distributions, incorporating bound constraints, are shown as 2D density plots in grey colour scale in the left-side panels and as orange curves in the marginal distribution plots. Yellow curves are prior probability distributions of slip deficit rate from the GDM.

4.2 Results

We conduct four different inversions for each of the four strain-rate maps for a total of 16 inversions, summarised in Table 4.1. The first inversion we conduct adopts a uniform prior on slip deficit rate (no preferred rate), with a lower bound of zero (to prevent backwards slip) and an upper bound equal to 10 times the GDM high slip rate. This is called the 'No Geologic Prior' inversion because geologic constraints are only used very loosely to bound slip deficit rates within an order of magnitude of the GDM rate. The second inversion assumes the truncated Gaussian prior distributions based on the geologic model, as described in Section 4.1.2, and is called the 'Geologic Prior' inversion. For the sake of comparison, and to illustrate the influence of the GDM constraints on inversion results, we also conduct a 'Strict Bounds' inversion, with strict bounds where the slip deficit rates are forced to lie between the GDM low and high slip rates using uniform, bounded prior distributions. The final result, called 'Fixed', is not an inversion at all; we fix the slip deficit rates to be exactly equal to the preferred geologic slip rates. The Variance reduction for each of these 16 models is given in Table 4.1. By design, the 'No Geologic Prior' inversions fit the data best, with variance reduction ranging from 68 to 79%. The 'Fixed' model fits less than half of the data, with variance reduction ranging from 38 to 49%.

In the following sections, we illustrate the principal results for the first two inversions in Table 4.1 ('No Geologic Prior' and 'Geologic Prior').

Table 4.1 Variance reduction for 16 different slip deficit rate inversions. Variance reduction defined as [1 – norm(residual) / norm(data)] x 100%, where norm(residual) is the norm of the residual vector and norm(data) is the norm of the data vector. All inversions have non-negative bounds. The four different inversion types are described in the main text.

	VELMAP	VDoHS	Geostatistics	Body Force
No Geologic Prior	71.7	75.5	67.8	79.0
Geologic Prior	70.2	72.9	55.1	76.9
Strict Bounds	57.9	65.0	54.7	66.9
Fixed	38.3	48.8	38.6	47.4

4.2.1 No Geologic Prior

Figure 4.6 illustrates the median slip deficit rate distribution for the 'No Geologic Prior' inversions with 3D perspective views of slip deficit rate on all of the rectangular slip patches. Figure 4.6b shows the median slip deficit rate from the four strain-rate map inversions with a logarithmic colour scale. Broadly speaking, the highest slip deficit rates occur, unsurprisingly, along the major strike-slip fault systems, including the Alpine Fault, the Marlborough Fault System and the North Island Dextral Fault Belt (Figure 4.6c). Slip deficit rates on off-shore faults are not reliable (and highly uncertain) because of the lack of geodetic data offshore. Figure 4.7 illustrates how much of the observed strain-rate field can be explained by slip deficit rate on the fault surfaces of the New Zealand NSHM 2022 fault model. The figure compares the mean maximum shear strain rate and dilatation of the four strain-rate maps with the mean rates of the four 'No Geologic Prior' inversions. The residual strain rates are computed by differencing the mean model strain rates from the mean observed rates. As shown in Table 4.1, this inversion result explains about 70–80% of the total strain-rate field. The residual maximum shear strain rates and dilatation rate maps (Figure 4.7) show the 20–30% of the total strain-rate field that is not explained by slip deficit rates on faults. As shown in previous sections, the uncertainties in maximum shear strain rate range from 0.01 to 0.05 micro-strain/yr and uncertainties in dilatation rate are of order 0.02 to 0.05 micro-strain/yr for the VDoHS, body force and VELMAP solutions; the uncertainties are several times larger in the geostatistics solution. Residual maximum shear strain rates exceed these uncertainties in the TVZ, at the southern edge and south of the Marlborough Fault system and in the northwest edges of the Otago and Southland regions (locations in Figure 4.6a). Residual dilation rates exceed uncertainties in a number of areas, and the modelled dilatation pattern is considerably more heterogeneous spatially than in the strain-rate maps. We see residual expansion (blue) along the southeast coast of the North Island and in the TVZ. The residual dilatation pattern is more heterogeneous in the South Island. In the following figures, we describe the estimated slip deficit rates in more detail.

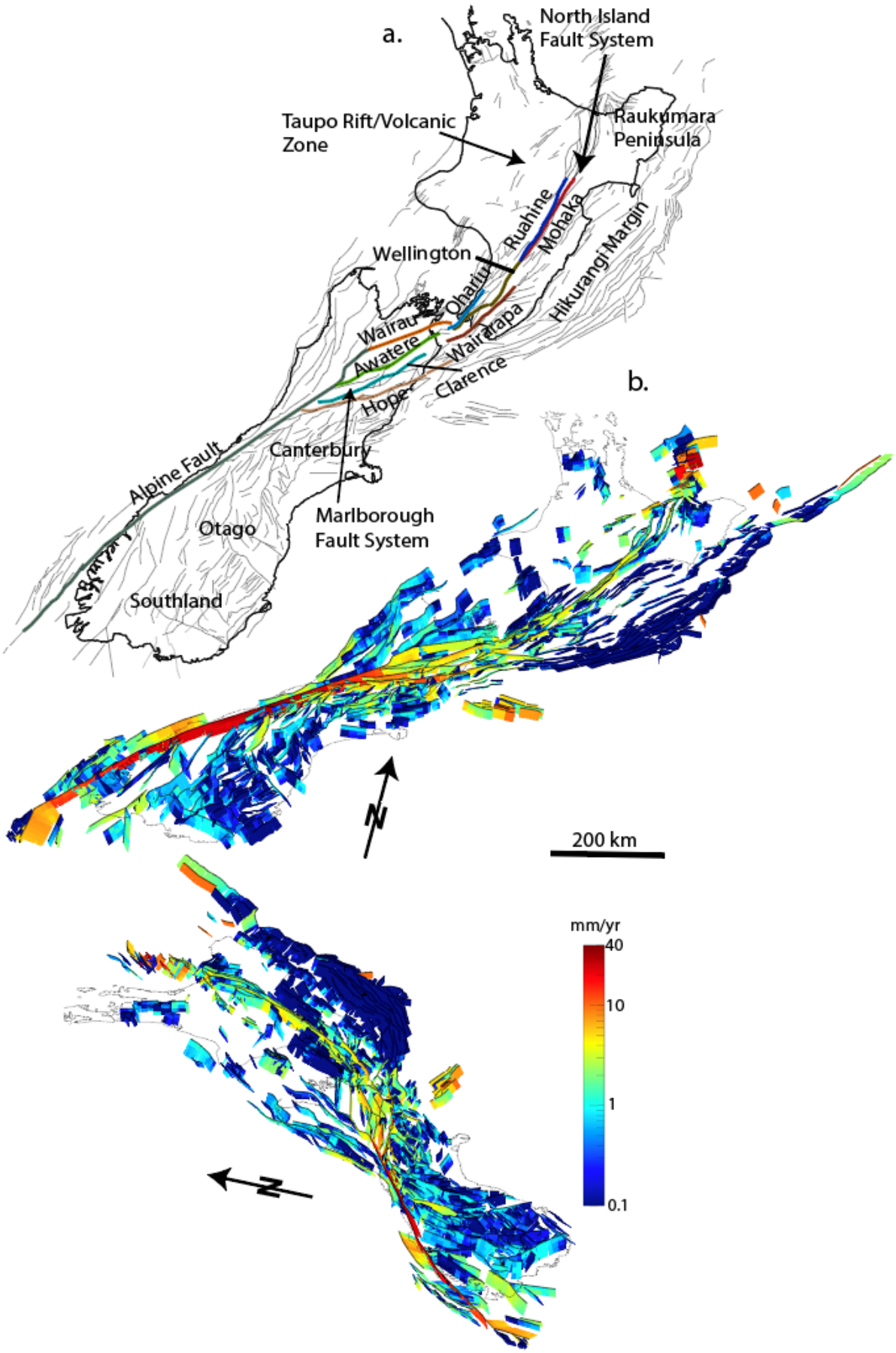

Figure 4.6 3D perspective views of median slip deficit rates. This is the median of the four best-fitting, unbounded inversions (one inversion for each strain-rate map). Colour shows slip deficit rate in mm/yr on a logarithmic colour scale.

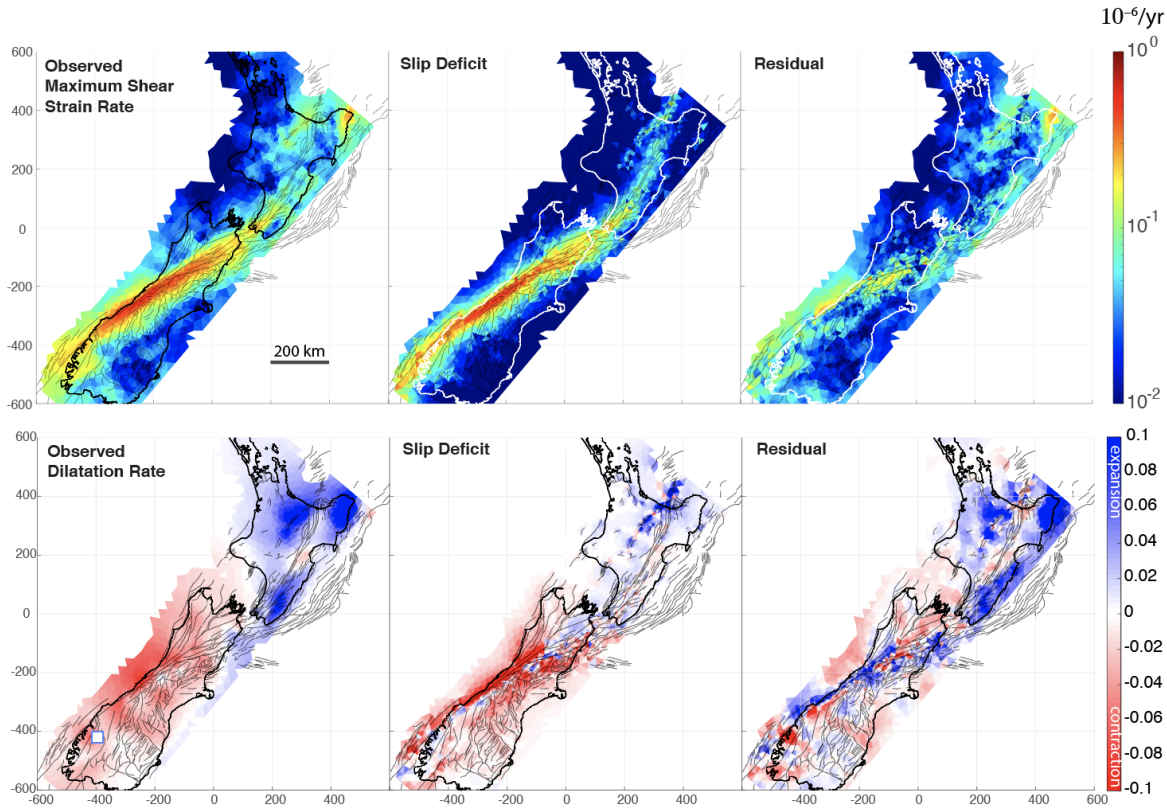

Figure 4.7 Comparison of observed and modelled strain rates computed from the average of the four strain-rate maps and the average of the means of the four strain-rate inversions. Left side panels are observed maximum shear strain rates and dilatation rates. Middle panels show modelled strain rates (strain rates due to slip deficit on faults). Right-side panels show observed minus modelled (residual).

Figure 4.8 compares the depth-averaged slip deficit rates for each of the four 'No Geologic Prior' inversions on a logarithmic colour scale. The differences between models are typically at the level of a few mm/yr or less on land. The off-shore slip deficit rates vary significantly, but this occurs because the off-shore slip deficit rates are unconstrained. Figure 4.9, which shows the difference between the mean depth-averaged slip deficit rates for each inversion and the GDM preferred slip rate on each fault section. There are systematic differences between the GDM preferred rates and the inverted slip deficit rates at the level of >1 mm/yr. The geodesy-based inversions infer higher slip rates on belts of faults following the Alpine Fault, as well as major strike-slip faults in the Marlborough Fault System and the North Island Fault zone. The geodesy-based inversions also infer systematically higher slip deficit rates southwest of the Marlborough Fault System and scattered throughout the Otago region. The geodetic rates are systematically lower along the near-shore part of the Hikurangi margin.

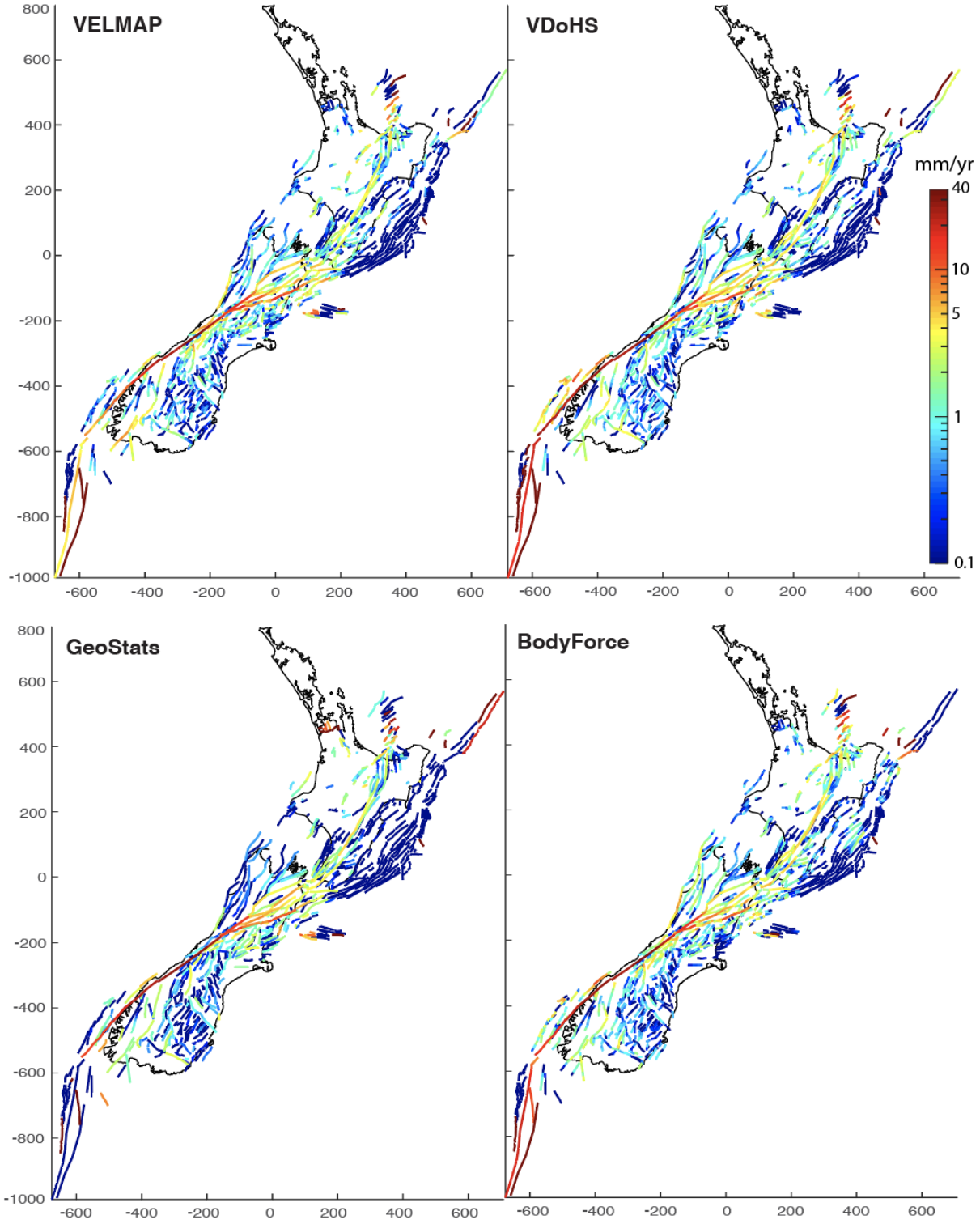

Figure 4.8 Mean depth-averaged slip deficit rates for the four strain-rate map inversions. Slip deficit rates shown along fault traces with a logarithmic colour scale.

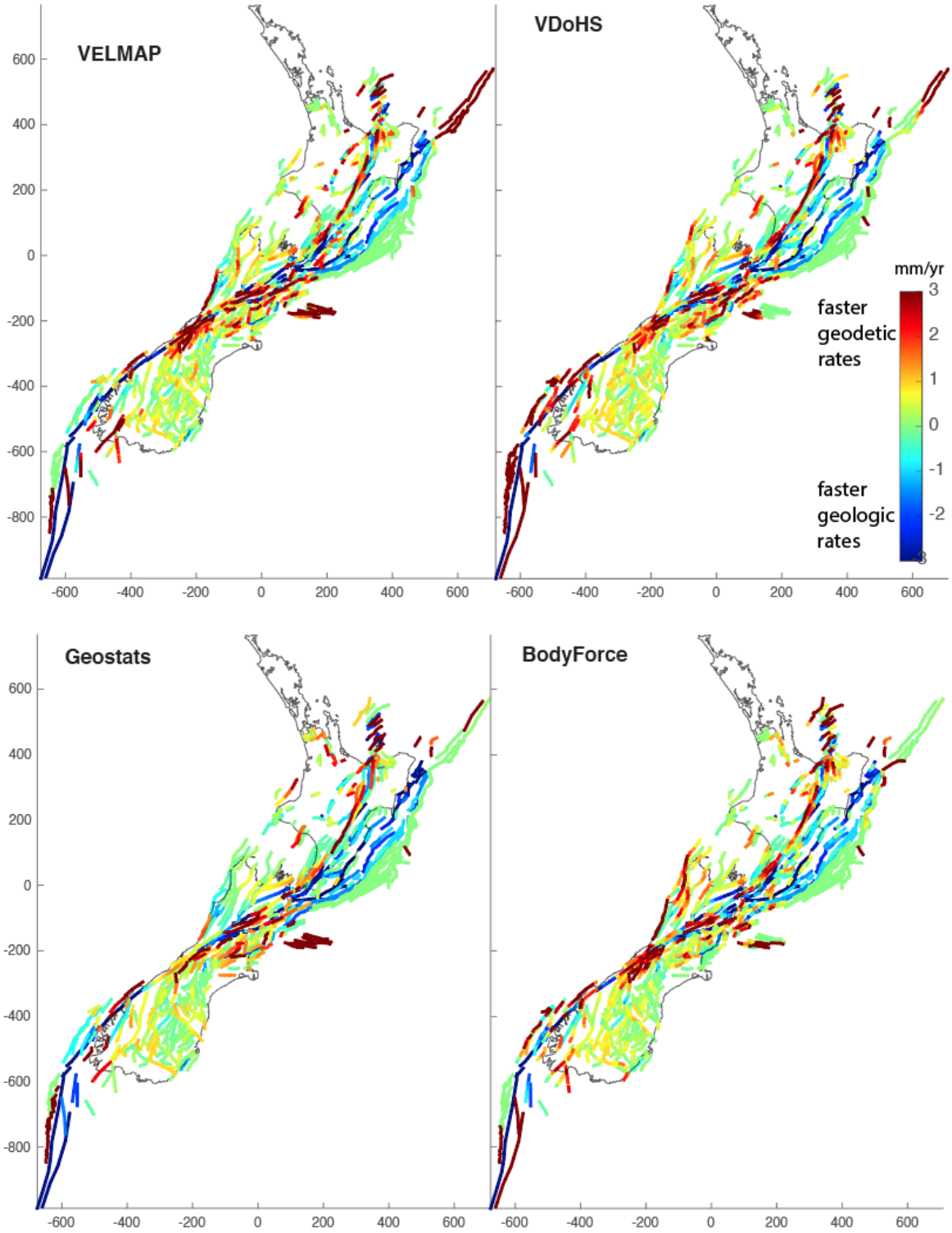

Figure 4.9 Difference between mean depth-averaged slip deficit rates and preferred geologic rates from the Geologic Deformation Model for the four strain-rate map inversions. Slip deficit rate differences (geodetic minus geologic) shown along fault traces with a logarithmic colour scale.

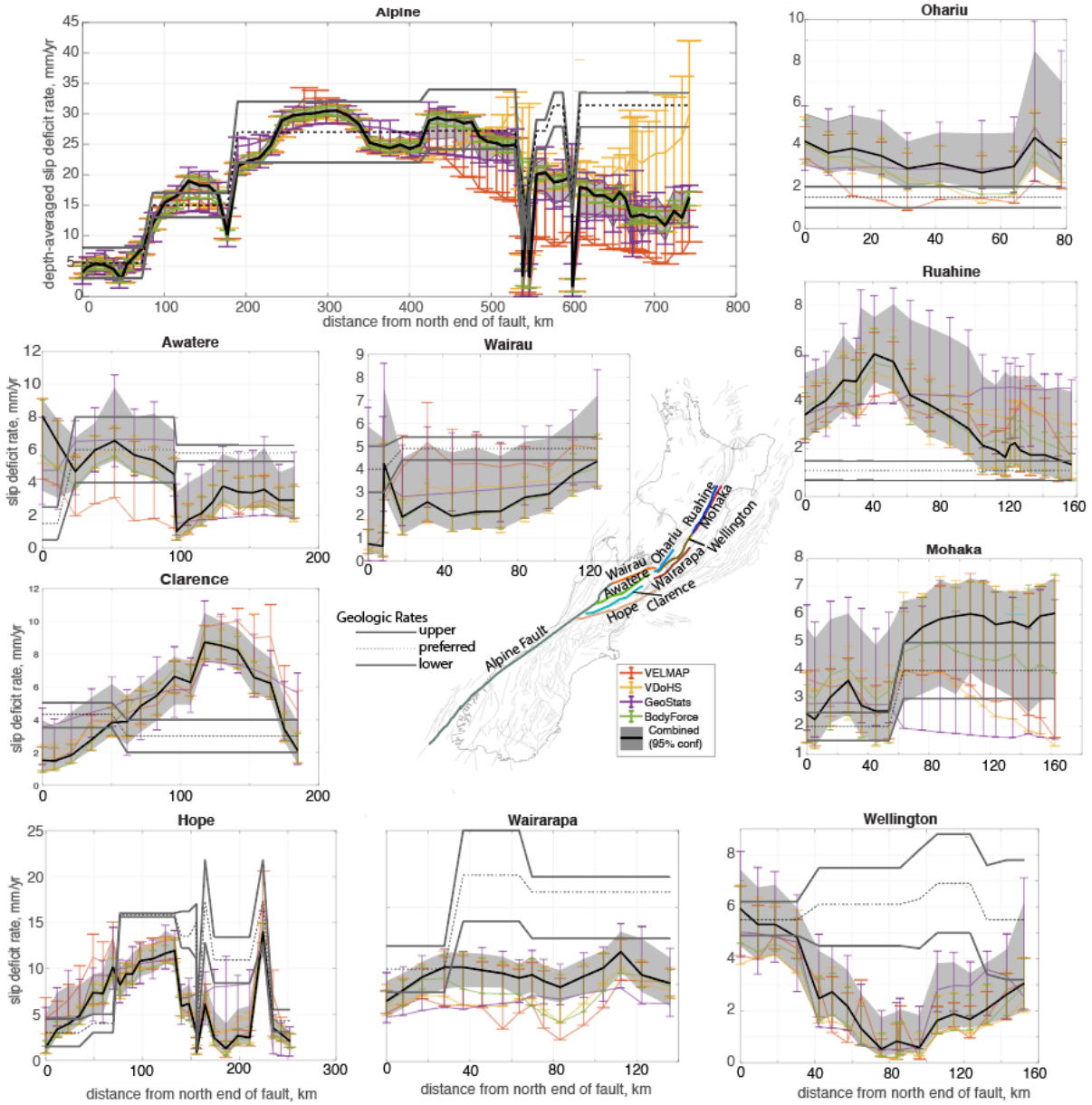

Figure 4.10 Plots of along-fault depth-averaged slip deficit rates. Best-fitting rates shown with curves and 95% error bounds shown with bars. The combined (or aggregate) distribution is shown with a solid black curve (most probable) and grey 95% confidence region.

Figure 4.10 summarises along-fault, depth-averaged slip deficit rates for some of the higher slip rate faults in New Zealand. The best-fitting (solid lines) and 95% confidence intervals (bars) are shown for each of the four strain-rate map inversions. The heavy solid black curve and grey-shaded region shows the aggregate mean and 95% confidence intervals. The aggregate rates are computed by combining all MCMC realisations of the four strain-rate map inversions into a single aggregate collection of realisations. For comparison, the figure also shows the preferred, upper and lower slip rates from the geologic slip rate model. The aggregate 95% confidence range of slip deficit rate is about 4 mm/yr for all of these high-rate faults. As described in the model description section, slip deficit rates are smoothed across fault segments; discontinuities in slip deficit rate are allowed across fault segments, as seen, for example, at ~100 km distance along the Awatere Fault. There are some significant deviations in model slip deficit rates from the GDM. In particular, the geodetically derived slip deficit rates at the 95% confidence level are lower than the geologic model slip rates along much of the Hope, Wairarapa and Wellington faults but higher along sections of the Clarence,

Ohariu and Ruahine faults. The slip deficit rates along the southern end of the Alpine Fault, beginning at about 500 km distance along the profile in Figure 4.10, are all systematically lower than the geologic model slip rates; however, we note that this section of the Alpine Fault is near the coastline or entirely off-shore and therefore the geodetic data constraints are poor and the computed strain rates here are dependent on the off-shore boundary conditions. As such, we regard these slip deficit rate estimates as unreliable.

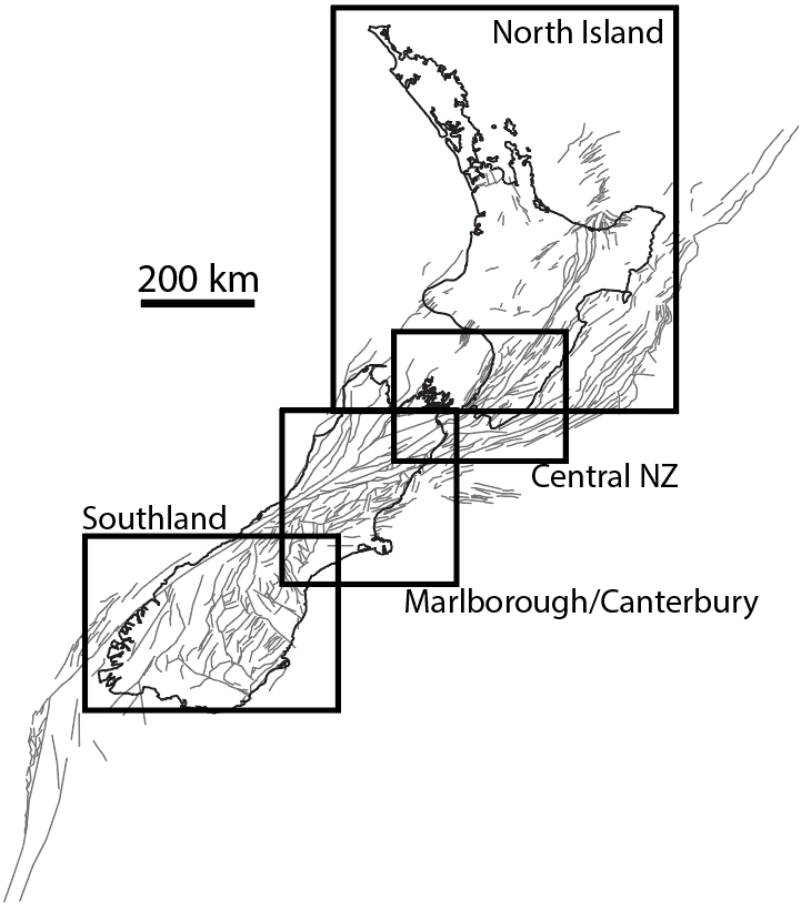

Figure 4.11 Location map for Figures 4.12–4.15.

In Figures 4.12–4.15, we show enlargements of maps of slip rate deficit and strain rate with the four regions illustrated in Figure 4.11. In these figures, we compare the observed and modelled maximum shear strain rates, as well as mean slip deficit rate distribution on 3D fault surfaces and mean depth-averaged slip deficit rates on faults. In these figures, the mean slip deficit rates and strain-rate predictions refer to the mean of the aggregate posterior distributions constructed from all four strain-rate map inversions. The mean observed strain-rate maps are computed as in Figure 4.7 by computing the mean of the four best-fitting strain-rate maps.

In the Southland/Otago region (Figure 4.12), the majority of shear strain rate occurs due to slip deficit rate on the Alpine Fault. However, there are non-trivial slip deficit rates (1–3 mm/yr) on N–NE/S–SW-trending faults south of the Alpine Fault that contribute to the wide belt of shear strain in the region. Most faults in the Otago region display ~1 mm/yr or lower slip deficit rates.

In the Marlborough/Canterbury region (Figure 4.13), the ~100-km-wide zone of shear strain rates exceeding 0.1 micro-strain/yr is accommodated largely by slip deficit rate on the Alpine Fault and Marlborough Fault System, but there are significant slip deficit rates of 1–5 mm/yr along the complex contractional and strike-slip fault systems south of the Hope Fault in the north Canterbury region.

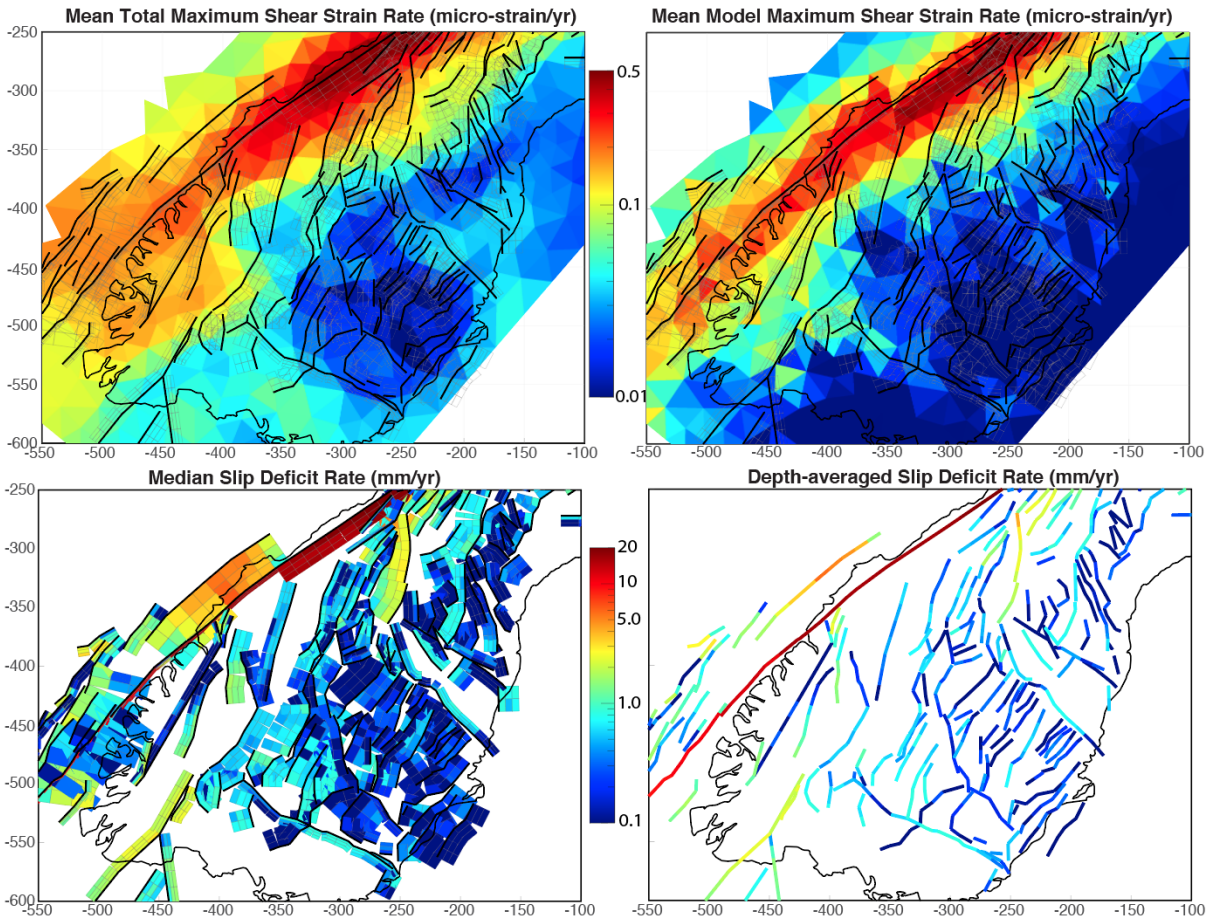

Figure 4.12 Results for the Southland region.

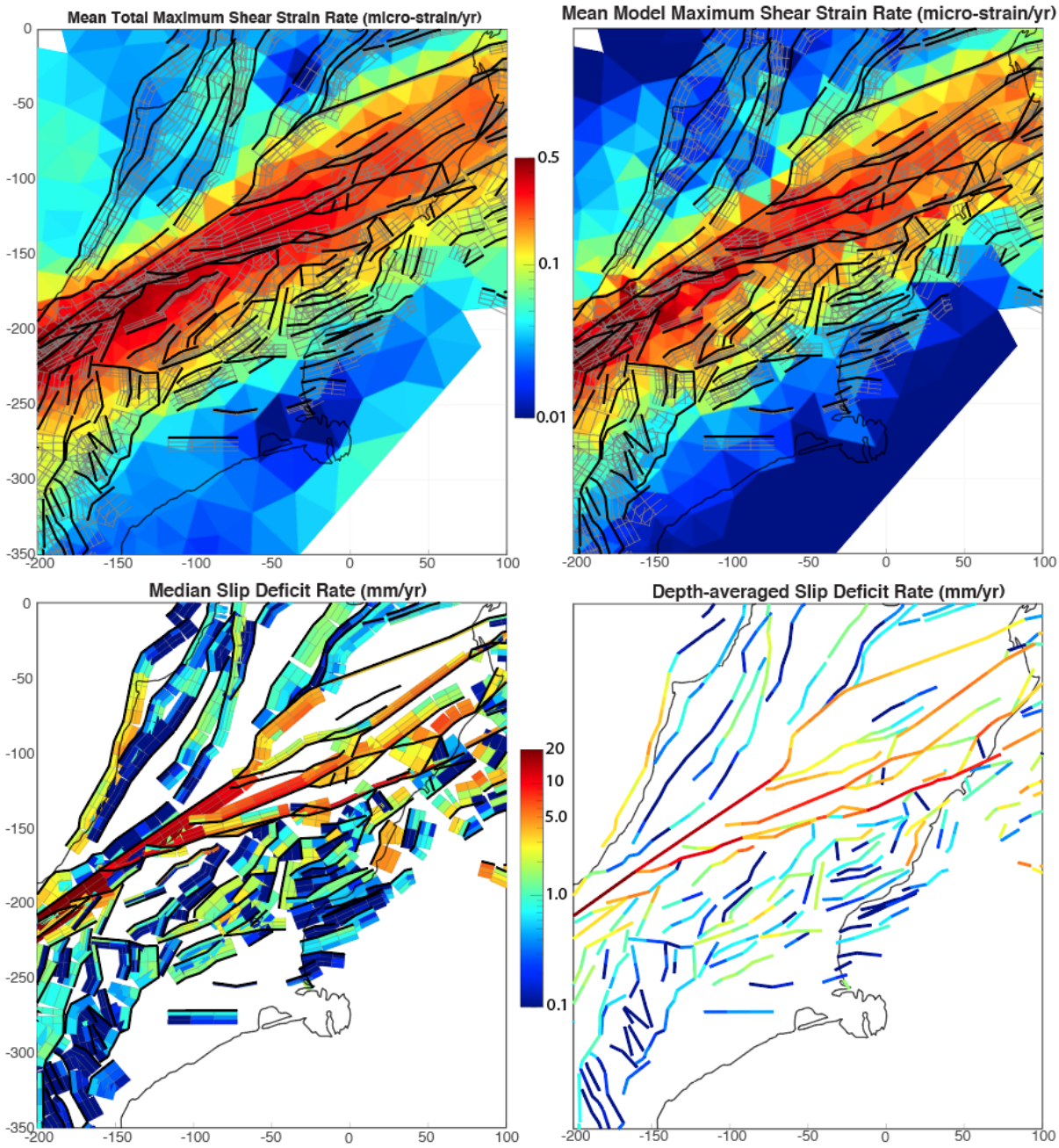

Figure 4.13 Results for the Marlborough/Canterbury region.

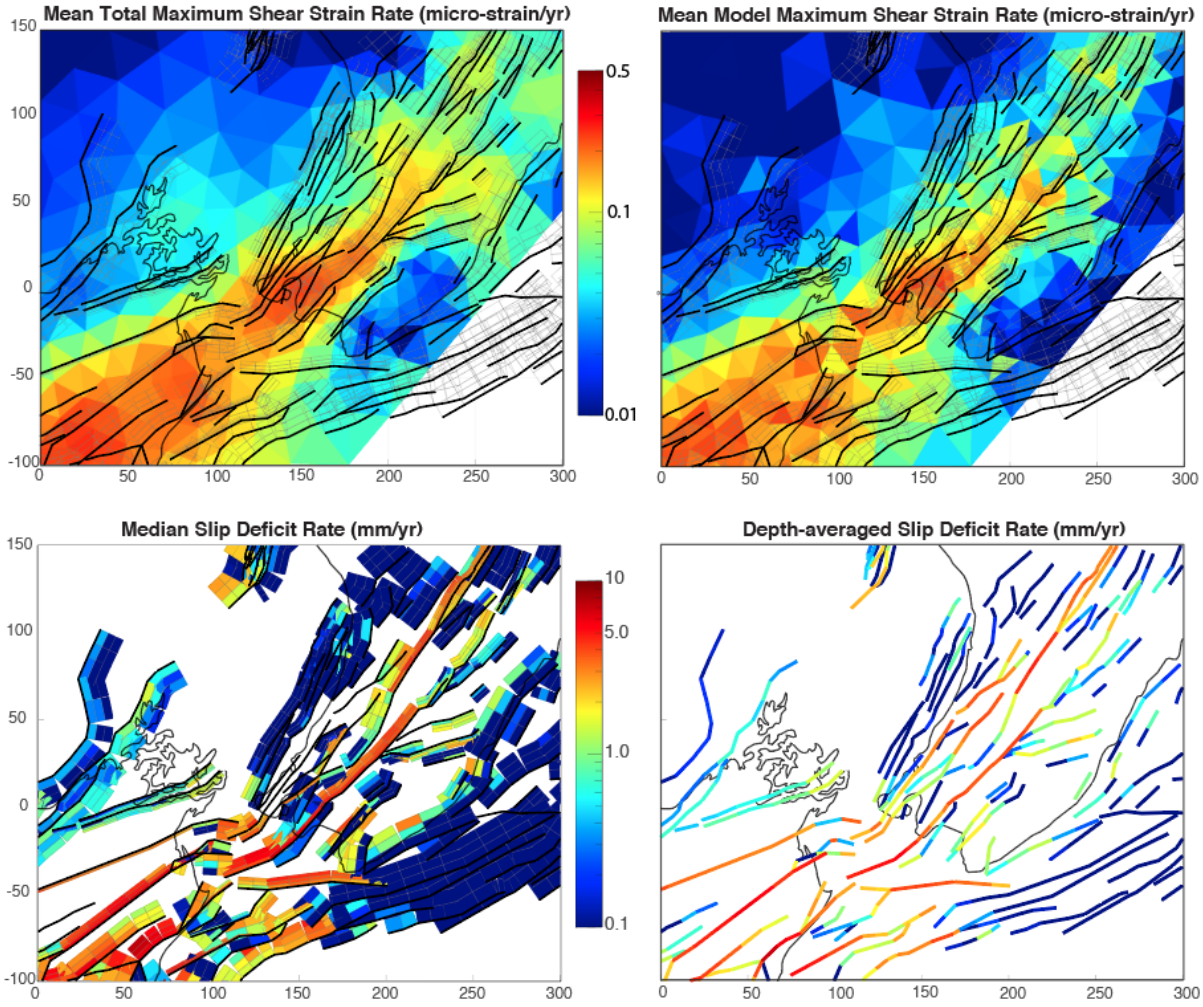

Figure 4.14 Results for the Central New Zealand region.

Figure 4.14 shows results for the Central New Zealand region. The maximum shear strain rates are lower here than in the Marlborough Fault System to the south. The observed zone of highest maximum shear strain rate in this region narrows from about ~100 km wide at the northeast end of South Island to about 50 km width in Wellington and narrowing to ~20 km width in the Tararua/Wairarapa region. The mean model maximum shear strain-rate map captures that basic spatial pattern. The shear through the Wellington region is accommodated by slip deficit rate across multiple faults, summing to about 13–15 mm/yr, with nearly half of that rate accommodated across the Wairarapa Fault.

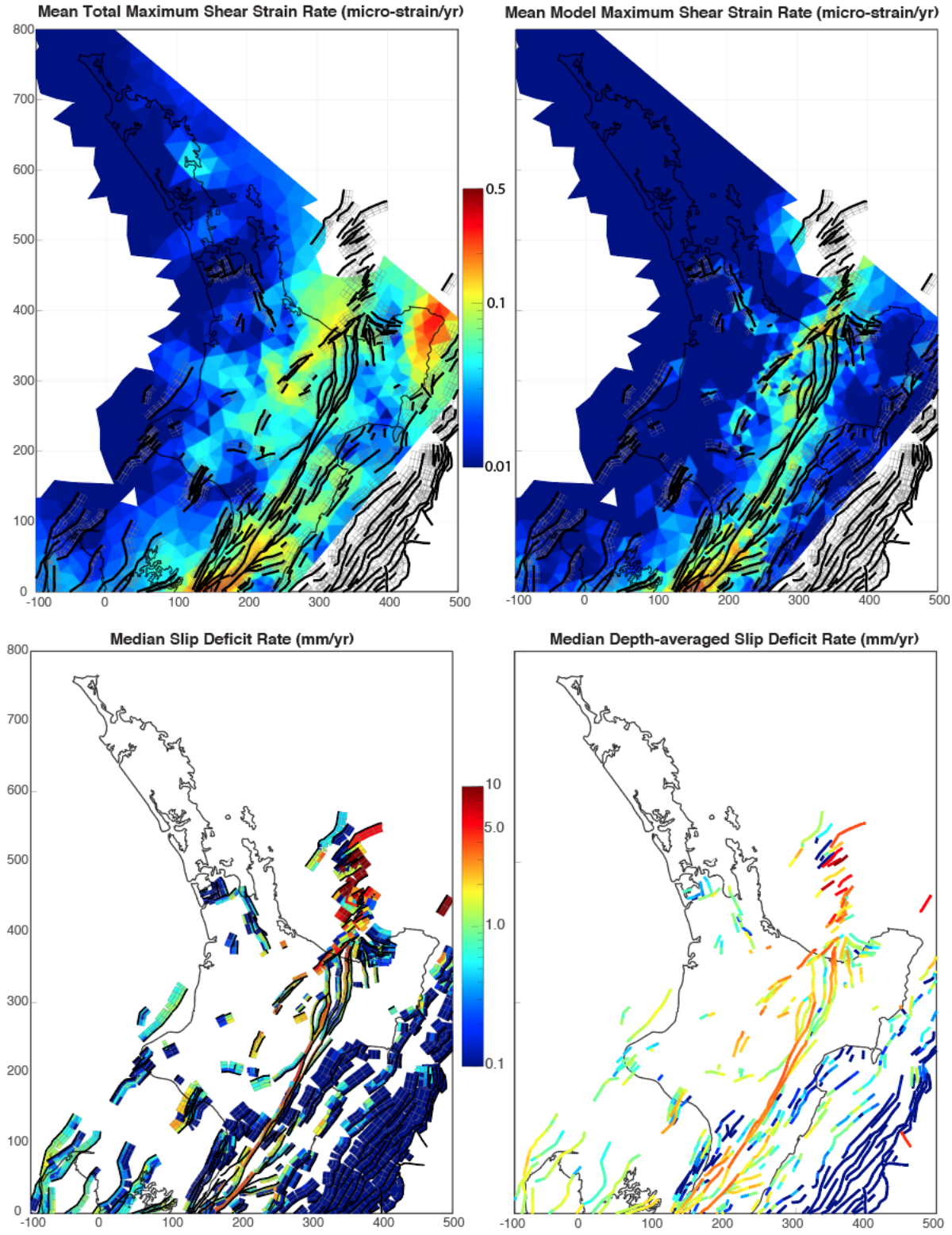

Figure 4.15 Results for the North Island region.

Figure 4.15 shows results for the North Island region. The shear strain rates are lower than the other regions, of order 0.1 micro-strain/yr and less. The strain is distributed broadly across the North Island, especially within the TVZ, the North Island Dextral Fault Belt and along the eastern coast. The strain rate along the North Island Dextral Fault Belt is accommodated by ~7–8 mm/yr of slip deficit rate across the Ruahine and Mohaka faults. The broadly distributed strain outside of this fault system largely cannot be modelled with slip deficit rate on faults in the model.

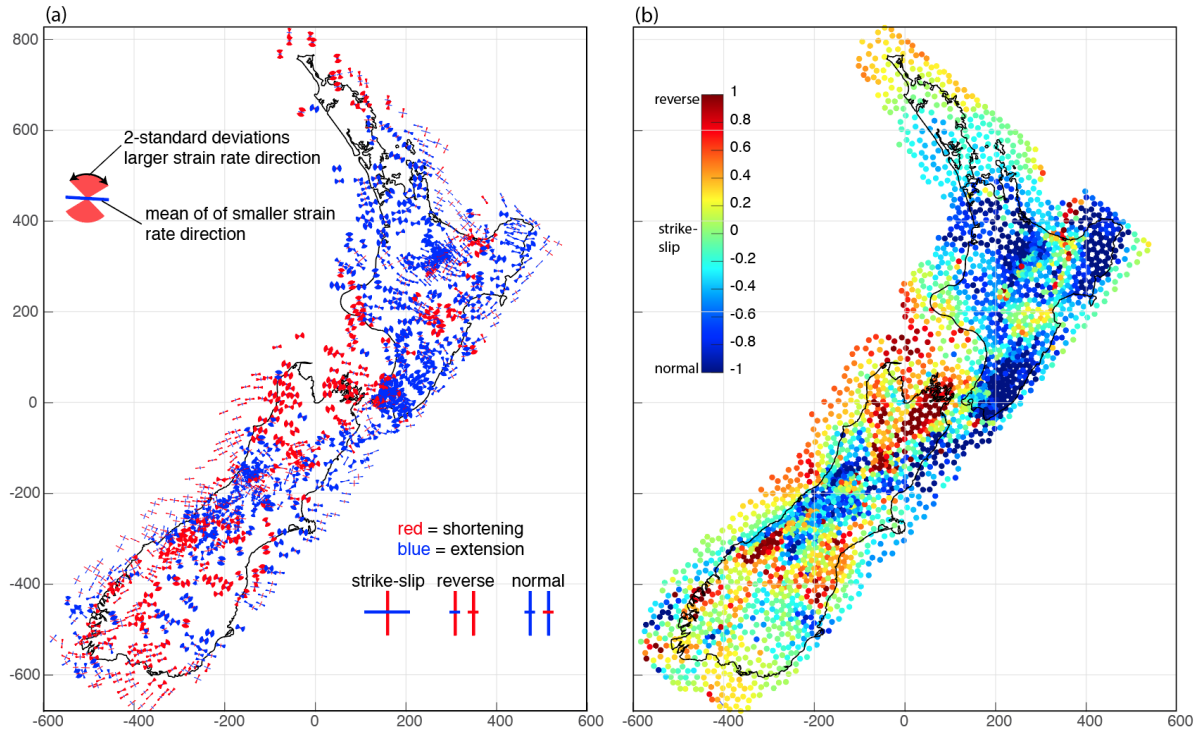

Figure 4.16 Analysis of residual strain-rate field. (a) Principal directions and uncertainties. This is constructed by subtracting the mean strain-rate field (mean of four best-fitting inversions) from the combined strain-rate field and uncertainties. (b) Residual strain-rate style. Strain-rate style defined in main text.

The residual strain-rate rates for the 'No Geologic Prior' are further analysed in Figure 4.16. Figure 4.16a shows the 95% confidence wedges on the orientations of residual principal strain rates. These wedges are computed by subtracting the mean model strain-rate field from the combined strain-rate field and 95% confidence intervals. Thus, these uncertainties in residual strain rate only incorporate uncertainties in the observed strain rates, not uncertainties in model strain rates. Figure 4.16a only shows strain rates at locations where the 95% confidence wedge angle is less than 60°. The symbols are the same as in Figure 3.19, with red bars or wedges indicating shortening and blue bars or wedges indicating extension rates. The strain rate 'style', computed as in Figure 3.19 of the mean residual strain-rate map, is shown in Figure 4.16b. It is clear from Figure 4.16 that the residual strain rates are not simply random noise; there are clear spatial patterns in residual strain-rate style. For example, the residual strain-rate field in the North Island is a systematically normal-faulting style with maximum extension rate directions oriented predominantly in the NW–SE quadrants. There is a zone of reverse-faulting style residual strain rates in the northwest Nelson region (northwest corner of the South Island). Along the Alpine Fault, within the Southland and Otago regions, there are zones of either reverse or normal faulting style. These are strain-rate zones that cannot be attributed to slip deficit rate on faults in the hazard model. Whether this strain rate is in reality accommodated by slip deficit on faults not in the hazard model, or as distributed off-fault strain throughout the crust, is not clear.

4.2.2 Inversion with Geologic Priors

We very briefly summarise the inversion with geologic slip rate priors in this section. Figure 4.17 shows the along-fault depth-averaged slip deficit rates for this inversion. Figure 4.17 is similar to Figure 4.10, with best-fitting slip deficit rates and 95% confidence intervals shown with colour curves and error bars. The aggregate slip deficit rate model is shown with light grey shading of the 95% confidence interval and a light grey heavy line showing the mean rate. For comparison, we also show the aggregate model for the 'No Geologic Model' (repeat from Figure 4.10) with

the darker shaded region. It is clear from a comparison of the two aggregate model results in Figure 4.17 that the inversion results with the geologic prior are shifted closer to the geologic model, and, in a majority of fault sections, the 95% confidence regions overlap the geologic model rates. The slip deficit rates from the geostatistics inversion are in best agreement with the geologic model because the larger uncertainties in the geostatistics strain-rate map allows the inversion to better match the prior slip deficit rates. However, even with the geologic prior, the estimated slip deficit rates along the southern sections of the Hope, Wairarapa and Wellington faults are lower than the geologic range.

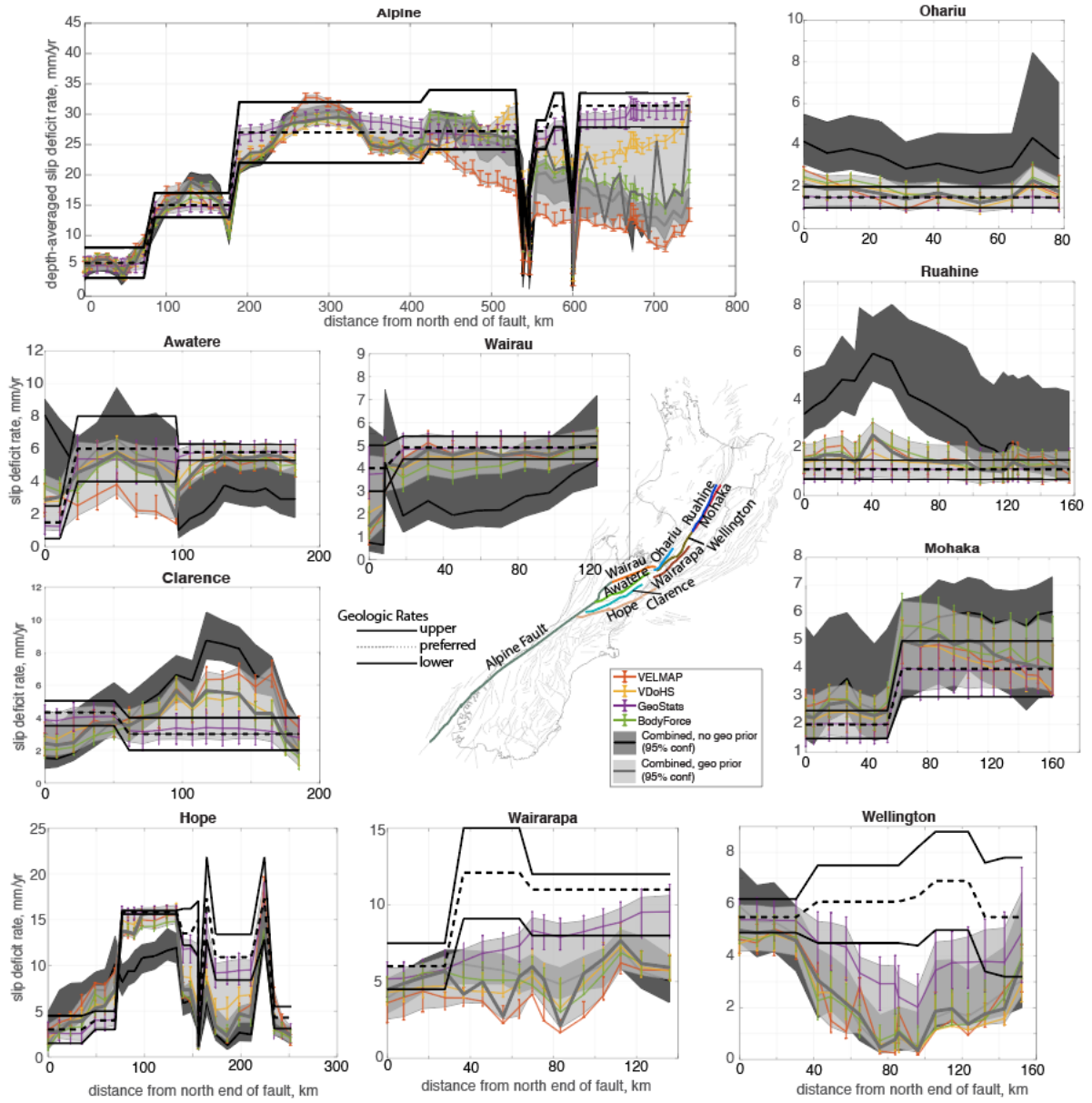

Figure 4.17 Comparison of along-fault depth-averaged slip deficit rates for inversions with and without the geologic priors. The combined distribution is shown with solid lines (most probable) and grey or orange 95% confidence regions.

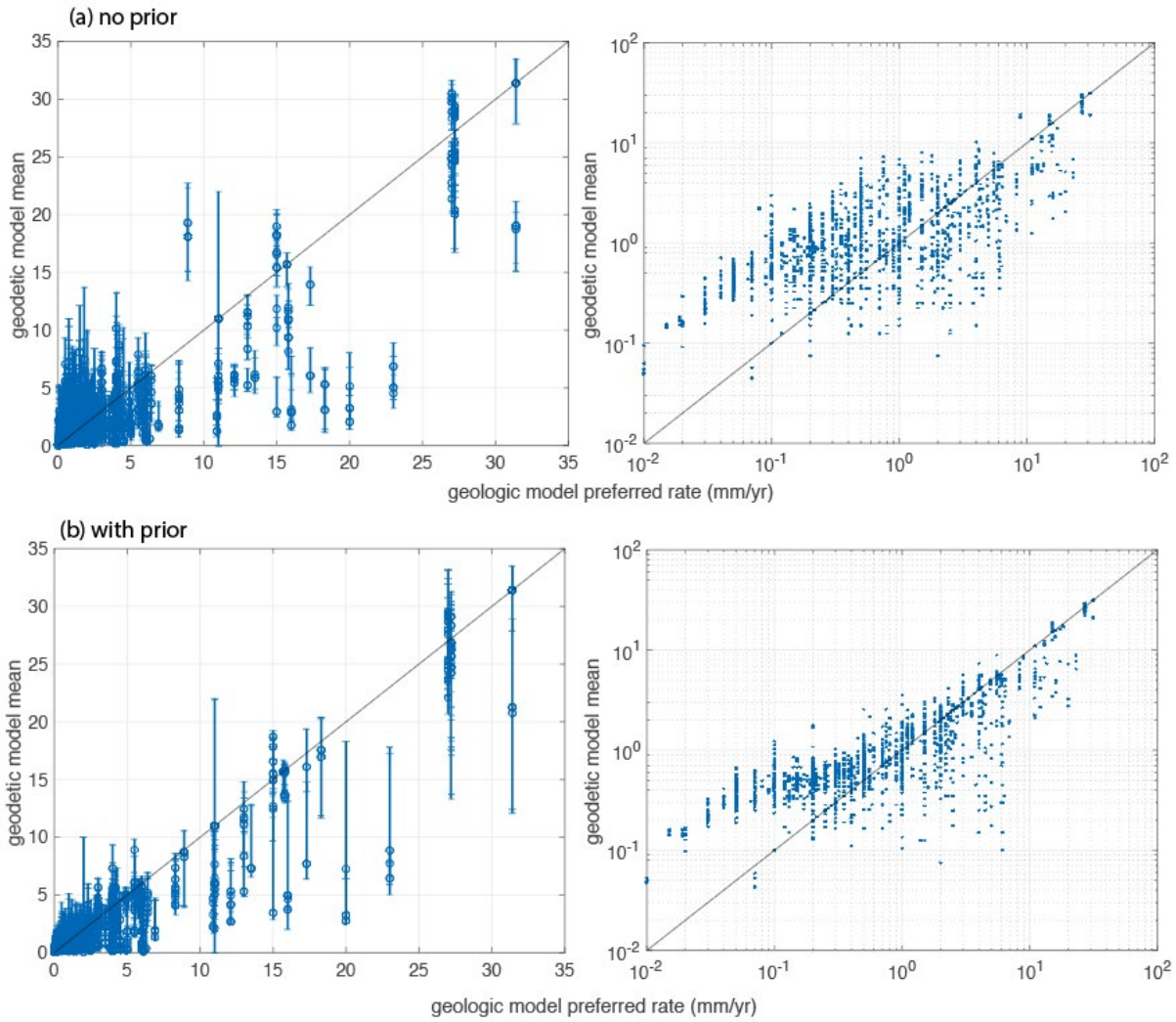

Figure 4.18 Comparison of Geologic Deformation Model (GDM) preferred slip rates and depth-averaged slip deficit rates. GDM rate is plotted on the horizontal axes and geodetically derived slip deficit rate is plotted on the vertical axes. (a) Geodetic result with no geologic prior. Error bars show the upper and lower 95% confidence limits for the geodetically derived rates. (b) Geodetic result with geologic prior.

Figure 4.18 compares the aggregate slip deficit rates by fault section with the preferred slip rate from the GDM. It is interesting to note that the cluster of points trend along a line with slope less than 1 for both sets of inversions, indicating a systemic mismatch. For fault sections with GDM rates less than about 1 mm/yr, there is a tendency for the geodetic slip deficit rates to be higher than the GDM rates, while, for sections with GDM rates above 1 mm/yr, the geodetic slip deficit rates tend to be lower. It is not immediately clear why this trend occurs, but it indicates that the GDM slip rates on low-rate faults are systematically lower than indicated by the present-day strain rates. This could occur for several reasons: (1) if the slip rates on low-rate faults are systematically underestimated in the GDM, (2) if low-rate faults are missing in the fault model or (3) if off-fault strain is not released as slip on faults and incorrectly mapped to fault slip deficit rate in the geodetic inversion. The systematic mismatch for fault sections with slip rates greater than about 1 mm/yr could potentially be attributed to fault creep (present-day slip deficit rate is lower than the long-term slip rate). Further examination of these systematic discrepancies is warranted for future NSHM studies.

Perhaps the most important discrepancy for seismic hazard in New Zealand is along the Wellington Fault (Figure 4.17) where the geodetic inversions show slip deficit rates of 1–4 mm/yr compared to slip rates of 5–8 mm/yr in the GDM. Given the close proximity

of the Wellington Fault to the southern end of the Hikurangi subduction margin, it is reasonable to question the influence of the method of removal of strain associated with coupling along the Hikurangi subduction zone on inferred rates on the Wellington Fault. For example, could some of the strain rate associated with coupling on the Wellington Fault be unintentionally subtracted from the geodetic data through the subduction zone coupling model adopted here? To test this, we conducted slip deficit rate inversions without the Hikurangi subduction correction to the velocity field and also using half of the correction (divide the correction velocities by two). These test inversions yielded similarly low geodetic slip deficit rates on the Wellington Fault, suggesting that this result is robust and not influenced significantly by the choice of Hikurangi coupling model.

4.3 Depth Distribution of Moment Accumulation Rate

To this point, we have focused our attention on depth-averaged slip deficit rates. It is interesting to consider whether or not the inversions can resolve the depth distribution of slip deficit rate. Figure 4.19 shows the centroid of moment accumulation rate on all fault sections in the model for all realisations of slip deficit rate generated to compute the posterior slip rate deficit distributions. The centroid of moment accumulation rate is simply the sum of the moment rate times depth to the centre of each patch along a fault section normalised by the total moment rate on the fault section. The distribution shows that centroid of moment accumulation is largely concentrated between about 5–15 km depth. However, this distribution looks like a slightly spread-out version of the distribution of fault section centroid depths, indicating that the inversion of geodetic data does not resolve depth of moment rate on average over the entire New Zealand region any better than using the centroid of the model fault sections.

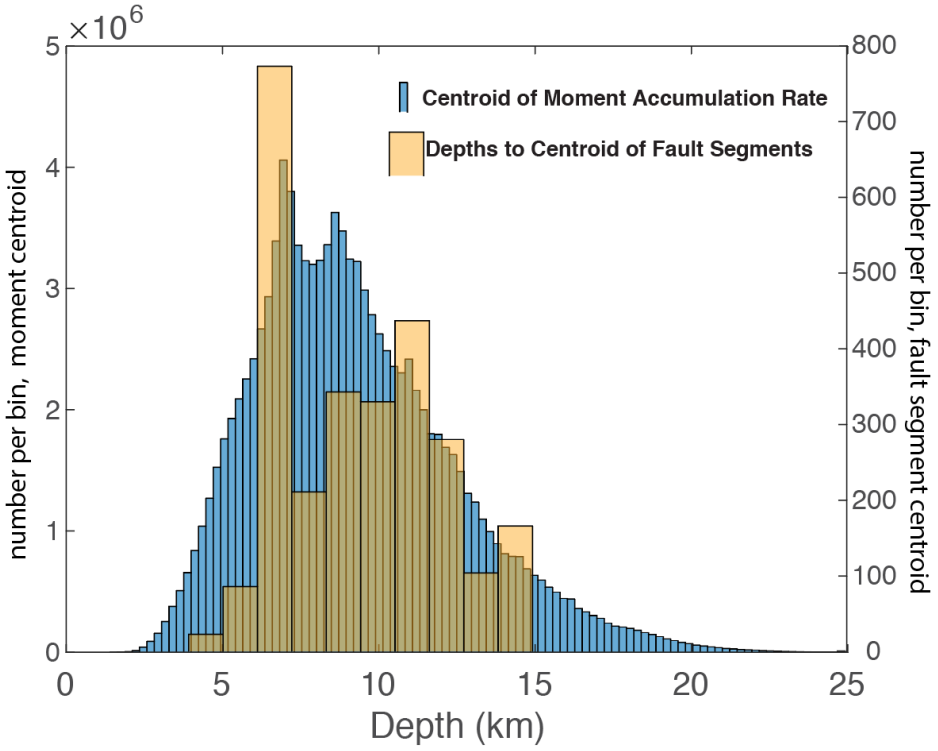

Figure 4.19 Comparison of depths to centroid of moment accumulation rate (blue histogram) to centroid depths of model fault sections (orange histograms). Centroid of moment accumulation rate is defined as the sum of the moment rate times depth to the centre of each patch along a fault section, normalised by the total moment rate on the fault section.

To examine whether the inversion can resolve the depth distribution of slip deficit rate on the highest slip rate faults, we show the depths of centroids of moment accumulation rate with distance along faults in Figure 4.20 with blue curves and 95% confidence intervals with error bars. The orange curves show the fault centroid depths. It is clear that the 95% confidence intervals of centroids of moment accumulation rate overlap the fault centroid depths. This suggests that the model slip deficit rate distribution on faults is not systematically skewed shallower or deeper than the middle depth of fault segments. Therefore, applying the estimated depth-averaged slip deficit rates over the entire model depth range (surface to D90 depth) is consistent with geodetic inversion results.

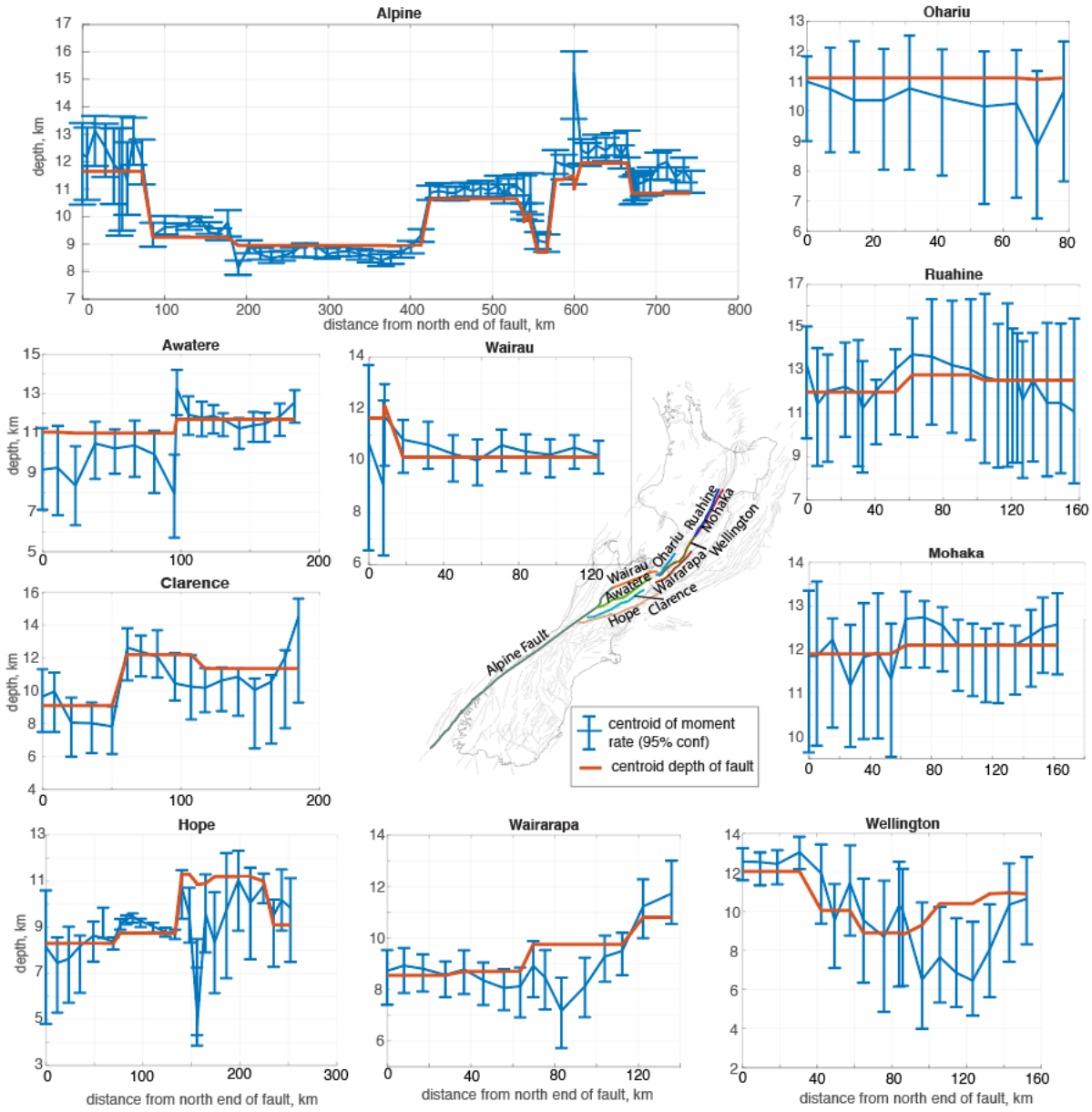

Figure 4.20 Depths of centroid of moment accumulation rate with distance along faults (blue curves) and 95% confidence intervals (blue error bars). Orange curves show centroid depth of faults.

4.4 Conclusions from Slip Deficit Rate Inversions

We conducted four inversions for slip deficit rate of each of the four strain-rate maps for a total of 16 inversions. The variance reduction is summarised in Table 4.1. Inversions that are bounded by geologic upper and lower slip rates explain only 55–67% of the data, whereas unbounded inversions explain 70–80% of the total strain-rate field. Residual strain rates that are not explained by slip deficit rates on faults are relatively low, with maximum shear strain rates typically less than about 0.1 micro-strain/yr. However, the residual strain rates are not randomly distributed; there are systematic spatial patterns to the style of the residual strain-rate field, indicating a potential tectonic origin to the residual strain rates. It is unclear whether this unmodeled strain can be attributed to slip deficit on faults not in the model or off-fault strain distributed through the crust.

The spatial distribution of depth-averaged slip deficit rate across model faults is similar for all four strain-rate map inversions with differences of less than about 3–4 mm/yr on the highest slip rate faults. However, there are systematic differences between the geologic preferred rates and the inverted slip deficit rates at the level of >1 mm/yr. The geodesy-based inversions infer higher slip rates on the major strike-slip systems, including the Alpine Fault, the Marlborough Fault System and the northern part of the North Island Dextral Fault Belt. The geodesy-based inversions also infer systematically higher slip deficit rates southwest of the Marlborough Fault System and scattered throughout the Otago region. The geodetic rates are systematically lower along the near-shore part of the Hikurangi margin. We also note that the slip deficit rate results are similar to those obtained in previous studies that invert the geodetic velocity field for block rotations and fault coupling (e.g. Wallace et al. 2004, 2012), indicating that our approach of inverting strain rates (rather than the velocity field as is conventionally done) produces comparable results in the New Zealand environment.

The inversions without geologic priors yield slip deficit rates that are significantly different from the geologic model slip rates along a few of the high-rate faults. Inferred slip deficit rates are higher than the geologic model along the Ohariu, Ruahine and southern Clarence faults. Inferred slip deficit rates are lower than the geologic model along the Hope, Wairarapa and Wellington faults. The inversions with geologic priors yield slip deficit rates with 95% confidence limits that largely overlap the range of slip rates in the geologic slip-rate model. Three exceptions are the southern section of the Hope Fault, the Wairarapa Fault and the southern sections of the Wellington Fault, all with slip deficit rates at or below the lower limit of the geologic model.

Finally, we find no significant difference in the centroid depth of moment accumulation rate from the centroid depth of faults. This indicates that applying the estimated depth-averaged slip deficit rates over the entire model depth range (surface to D90 depth) is consistent with geodetic inversion results.

5.0 CONCLUSIONS, IMPLEMENTATION RECOMMENDATIONS AND FUTURE DIRECTIONS

The principal result from the different strain-rate analyses conducted for this study is that the inferred strain-rate field is similar across all methods; the spatially averaged maximum shear strain rates from the mean models vary from 0.1 to 0.12 micro-strain/yr, disagreeing at only about the 20% level, while spatially averaged dilatation rates ranging between about 0.015 and 0.022 micro-strain/yr disagree more significantly at the ~40% level. The dilatation rates appear to show the impact of different types of spatial interpolation methods, with VDoHS and body force results being relatively smooth, while VELMAP and geostatistics are comparatively rougher but with different characteristics. The uncertainties of the four methods, which are calculated in quite different ways, are also quite variable. On-shore, the maximum shear strain residuals are comparable to the uncertainties, while off-shore and in data-poor areas the elastic thin-plate and VELMAP solutions have very small uncertainties compared to the geostatistical method and residuals between methods. The uncertainties of the VDoHS, body force and VELMAP methods are small relative to the differences between methods, while the geostatistical method has uncertainty larger than the differences.

Adopting the commonly held assumption that the majority of present-day strain-rate field is elastic strain due to interseismic coupling across actively slipping faults, we inverted the four strain-rate maps for slip deficit rates on faults. We conduct suites of inversions with and without the geologic slip-rate model as a prior on slip deficit rates. The differences in slip deficit rate across all four strain-rate map inversions is typically less than 3–4 mm/yr for the high-rate faults. There are some notable differences between the geologic slip-rate model and the slip deficit inversion results. The geodesy-based inversions infer higher slip deficit rates on belts of faults along the Alpine Fault and major strike-slip faults in the Marlborough Fault System and northern part of the North Island Dextral Fault Belt. The geodesy-based inversions also infer systematically higher slip deficit rates southwest of the Marlborough Fault System and scattered throughout the Otago region. The geodetic rates are systematically lower along the near-shore part of the Hikurangi margin. The slip deficit rate models explain 70–80% of the total strain-rate field; the remaining 20–30% of the strain-rate field cannot be mapped to slip deficit rates on faults. The source of residual strain rates is unclear, but systematic spatial patterns to the style of the residual strain-rate field suggest a potential tectonic origin to the residual strain rates. We find no significant difference in the centroid depth of moment accumulation rate from the centroid depth of faults. This indicates that applying the estimated depth-averaged slip deficit rates over the entire model depth range (surface to D90 depth) is consistent with geodetic inversion results.

Implementation Recommendations

Based on what we learned from the strain rate and slip deficit rate inversions in this study, we make a series of recommendations for the use of the strain-rate maps and slip deficit rate inferences in the 2022 New Zealand NSHM:

1. Offshore fault slip rates should be replaced with GDM rates because of the lack of offshore geodetic data constraints.
2. Aggregates of the two suites of slip deficit rate inversions, with geologic priors and without geologic priors, adequately represent the uncertainty in slip deficit rate. The mean, upper and lower 95% bounds on slip deficit rates of the aggregate slip deficit rate for both models was submitted to the NSHM. This is a pragmatic decision based on the desire to incorporate epistemic uncertainty without many logic-tree branches. Our judgment is that the aggregate slip deficit rate model, which consists of mean and uncertainties of slip

deficit rates constructed from all MCMC realisations from the four strain-rate maps, best represents the epistemic uncertainty.

3. Shear strain rates from the VDoHS method (with the sill removed) are being used in the hybrid model to inform the distributed seismicity model. The remaining strain that is not fit by slip deficits on known faults could also be used in future to inform off-fault seismicity. However, given that much of this residual strain could be due to model deficiencies and/or aseismic deformation, this should be done with great caution (if at all). In a general sense, the 20–30% residual strain (that is not fit by slip deficits on known faults) could be used to verify and/or validate the relative percentage of on- and off-fault seismicity in the NSHM.

Future Directions

Although our approach to incorporating geodetic data into the New Zealand NSHM 2022 fault source model represents a significant advance on what has been done in previous versions of the NSHM, there are still many improvements that could be made in future versions of the model. For example, our deformation models are purely elastic models, and do not incorporate the possible influence of viscoelastic deformation, which can be particularly important for subduction zones (e.g. Li et al. 2015, 2018; Johnson and Tebo 2018) and crustal faults. Thus, viscoelasticity should also be considered as a major priority of the geodetic modeling for future versions of the NSHM. Moreover, incorporation of variable elastic properties throughout New Zealand in the slip deficit rate inversions (e.g. Williams and Wallace 2015) for all of the fault sources is recommended for future versions of the New Zealand NSHM. For this version, we chose only to implement this for the Hikurangi subduction zone (see Section 2.2), as this is where the largest elastic contrasts are (between slab and forearc), and thus Hikurangi subduction interface slip deficit rate inversions will be the most strongly influenced by crustal elastic properties. To incorporate elastic heterogeneity into the crustal fault slip rate deficit inversions (using strain rates), new approaches will have to be developed to calculate elastic Green's functions for strain rates that are compatible with our strain-rate inversion method. We also acknowledge the possibility that some of the elastic strain being interpreted as due to locking on the Hikurangi subduction zone could instead arise from slip deficits on crustal faults overlying the plate interface (or vice versa). Ideally, for future versions of the NSHM, we should invert simultaneously for crustal fault the subduction interface fault slip deficit rates. An InSAR-based view of interseismic deformation in New Zealand is also bearing fruit (Hamling et al. 2022b), and future geodetic strain-rate models to underpin the fault slip inversions should incorporate these data as well.

6.0 ACKNOWLEDGMENTS

This work was funded by the New Zealand Ministry of Business, Innovation & Employment to GNS Science via the National Seismic Hazard Model 2022 Revision Project (contract 2020-BD101). We appreciate constructive and insightful reviews of this work from Jessica Murray, John Townend and Ned Field, which greatly improved this report.

7.0 REFERENCES

Aagaard BT, Knepley MG, Williams CA. 2013. A domain decomposition approach to implementing fault slip in finite-element models of quasi-static and dynamic crustal deformation. *Journal of Geophysical Research: Solid Earth*. 118(6):3059–3079. doi:10.1002/jgrb.50217.

Aagaard B, Knepley M, Williams C. 2017a. geodynamics/pylith: PyLith v2.2.1. Geneva (CH): Zenodo; [updated 2017 Sep 6; accessed 2021 Oct]. https://zenodo.org/record/886600#.YXdZ9flBw2w

Aagaard B, Knepley M, Williams C. 2017b. PyLith user manual: Version 2.2.0. Davis (CA): Computational Infrastructure for Geodynamics; [accessed 2021 Oct]. https://geodynamics.org/cig/software/github/pylith/v2.2.0/pylith-2.2.0_manual.pdf

Árnadóttir T, Haines J, Geirsson H, Hreinsdóttir S. 2018. A preseismic strain anomaly detected before M6 earthquakes in the South Iceland Seismic Zone from GPS station velocities. *Journal of Geophysical Research: Solid Earth*. 123(12):11091–11111. doi:10.1029/2018JB016068.

Aster RC, Borchers B, Thurber CH. 2018. Parameter estimation and inverse problems. 3rd ed. Amsterdam (NL): Elsevier. 392 p.

Baxter SC, Kedar S, Parker JW, Webb FH, Owen SE, Sibthorpe A, Dong D. 2011. Limitations of strain estimation techniques from discrete deformation observations. *Geophysical Research Letters*. 38(1):L01305. doi:10.1029/2010GL046028.

Beavan RJ, Haines AJ. 2001. Contemporary horizontal velocity and strain rate fields of the Pacific-Australian plate boundary zone through New Zealand. *Journal of Geophysical Research: Solid Earth*. 106(B1):741–770. doi:10.1029/2000JB900302.

Beavan RJ, Moore M, Pearson C, Henderson M, Parsons B, Bourne S, England P, Walcott D, Blick G, Darby DJ, et al. 1999. Crustal deformation during 1994–1998 due to oblique continental collision in the central Southern Alps, New Zealand, and implications for seismic potential of the Alpine fault. *Journal of Geophysical Research Solid Earth*. 104(B11):25233–25255. doi:10.1029/1999JB900198.

Beavan RJ, Wallace LM, Palmer NG, Denys P, Ellis SM, Fournier N, Hreinsdottir S, Pearson C, Denham M. 2016. New Zealand GPS velocity field: 1995–2013. *New Zealand Journal of Geology and Geophysics*. 59(1):5–14. doi:10.1080/00288306.2015.1112817.

Bertrand EA, Caldwell TG, Bannister S, Soengkono S, Bennie SL, Hill GJ, Heise W. 2015. Using array MT data to image the crustal resistivity structure of the southeastern Taupo Volcanic Zone, New Zealand. *Journal of Volcanology and Geothermal Research*. 305:63–75. doi:10.1016/j.jvolgeores.2015.09.020.

Bird P. 2009. Long-term fault slip rates, distributed deformation rates, and forecast of seismicity in the western United States from joint fitting of community geologic, geodetic, and stress direction data sets. *Journal of Geophysical Research: Solid Earth*. 114(B11):B11403. doi:10.1029/2009JB006317.

Cai J, Grafarend EW. 2007. Statistical analysis of geodetic deformation (strain rate) derived from the space geodetic measurements of BIFROST Project in Fennoscandia. *Journal of Geodynamics*. 43(2):214–238. doi:10.1016/j.jog.2006.09.010.

Chiles J-P, Delfiner P. 2009. Geostatistics: modeling spatial uncertainty. [Place unknown]: John Wiley & Sons. 719 p.

Davey FJ, Henrys SA, Lodolo E. 1995. Asymmetric rifting in a continental back-arc environment, North Island, New Zealand. *Journal of Volcanology and Geothermal Research*. 68(1–3):209–238. doi:10.1016/0377-0273(95)00014-I.

Desbrun M, Meyer M, Schröder P, Barr AH. 1999. Implicit fairing of irregular meshes using diffusion and curvature flow. In: *SIGGRAPH '99: Proceedings of the 26th annual conference on computer graphics and interactive techniques*; 1999 Aug 8–13; Los Angeles, California. New York (NY): ACM Press/Addison-Wesley Publishing Co. p. 317–324.

Dimitrova LL, Wallace LM, Haines AJ, Williams CA. 2016. High-resolution view of active tectonic deformation along the Hikurangi subduction margin and the Taupo Volcanic Zone, New Zealand. *New Zealand Journal of Geology and Geophysics*. 59(1):43–57. doi:10.1080/00288306.2015.1127823.

Dzurisin D, Savage JC, Fournier RO. 1990. Recent crustal subsidence at Yellowstone Caldera, Wyoming. *Bulletin of Volcanology*. 52:247–270. doi:10.1007/BF00304098.

Dzurisin D, Yamashita KM, Kleinman JW. 1994. Mechanisms of crustal uplift and subsidence at the Yellowstone caldera, Wyoming. *Bulletin of Volcanology*. 56:261–270. doi:10.1007/BF00302079.

Eberhart-Phillips D, Bannister S. 2015. 3-D imaging of the northern Hikurangi subduction zone, New Zealand: variations in subducted sediment, slab fluids and slow slip. *Geophysical Journal International*. 201(2):838–855. doi:10.1093/gji/ggv057.

Eberhart-Phillips D, Reyners ME. 2012. Imaging the Hikurangi Plate interface region, with improved local-earthquake tomography. *Geophysical Journal International*. 190(2):1221–1242. doi:10.1111/j.1365-246X.2012.05553.x.

Eberhart-Phillips D, Reyners M, Bannister S, Chadwick M, Ellis S. 2010. Establishing a versatile 3-D seismic velocity model for New Zealand. *Seismological Research Letters*. 81(6):992–1000. doi:10.1785/gssrl.81.6.992.

El-Fiky GS, Kato T, Fujii Y. 1997. Distribution of vertical crustal movement rates in the Tohoku district, Japan, predicted by least-squares collocation. *Journal of Geodesy*. 71:432–442. doi:10.1007/s001900050111.

Ellis SM, Bannister S, Van Dissen RJ, Eberhart-Phillips D, Boulton C, Reyners ME, Funnell RH, Mortimer N, Upton P. 2021. New Zealand Fault-Rupture Depth Model v1.0: a provisional estimate of the maximum depth of seismic rupture on New Zealand's active faults. Lower Hutt (NZ): GNS Science. 47 p. (GNS Science report; 2021/08).

England P, Molnar P. 1997. The field of crustal velocity in Asia calculated from Quaternary rates of slip on faults. *Geophysical Journal International*. 130(3):551–582. doi:10.1111/j.1365-246X.1997.tb01853.x.

England P, Molnar P. 2005. Late Quaternary to decadal velocity fields in Asia. *Journal of Geophysical Research: Solid Earth*. 110(B12):B12401. doi:10.1029/2004JB003541.

Engwirda D. 2014. Locally optimal Delaunay-refinement and optimisation-based mesh generation. [PhD thesis]. Sydney (AU): University of Sydney, School of Mathematics and Statistics. 204 p.

Feigl KL, Agnew DC, Bock Y, Dong D, Donnellan A, Hager BH, Herring TA, Jackson DD, Jordan TH, King RW, et al. 1993. Space geodetic measurement of crustal deformation in central and southern California, 1984–1992. *Journal of Geophysical Research: Solid Earth*. 98(B12):21677–21712. doi:10.1029/93JB02405.

Field EH, Arrowsmith RJ, Biasi GP, Bird P, Dawson TE, Felzer KR, Jackson DD, Johnson KM, Jordan TH, Madden C, et al. 2014. Uniform California earthquake rupture forecast, version 3 (UCERF3) – the time-independent model. *Bulletin of the Seismological Society of America*. 104(3):1122–1180. doi:10.1785/0120130164.

Fukuda J, Johnson KM. 2010. Mixed linear–non-linear inversion of crustal deformation data: Bayesian inference of model, weighting and regularization parameters. *Geophysical Journal International*. 181(3):1441–1458. doi:10.1111/j.1365-246X.2010.04564.x.

Goudarzi MA, Cocard M, Santerre R. 2015. GeoStrain: an open source software for calculating crustal strain rates. *Computers & Geosciences*. 82:1–12. doi:10.1016/j.cageo.2015.05.007.

Hackl M, Malservisi R, Wdowinski S. 2009. Strain rate patterns from dense GPS networks. *Natural Hazards and Earth System Sciences*. 9(4):1177–1187. doi:10.5194/nhess-9-1177-2009.

Haines AJ, Dimitrova LL, Wallace LM, Williams CA. 2015. Enhanced surface imaging of crustal deformation: obtaining tectonic force fields using GPS data. Cham (CH): Springer. 99 p.

Haines AJ, Holt WE. 1993. A procedure for obtaining the complete horizontal motions within zones of distributed deformation from the inversion of strain rate data. *Journal of Geophysical Research: Solid Earth*. 98(B7):12057–12082. doi:10.1029/93JB00892.

Haines AJ, Wallace LM. 2020. New Zealand-wide geodetic strain rates using a physics-based approach. *Geophysical Research Letters*. 47(1):e2019GL084606. doi:10.1029/2019gl084606.

Haines AJ, Wallace LM, Dimitrova L. 2019. Slow slip event detection in Cascadia using vertical derivatives of horizontal stress rates. *Journal of Geophysical Research: Solid Earth*. 124(5):5153–5173. doi:10.1029/2018jb016898.

Hamling IJ, Hreinsdottir S, Fournier N. 2015. The ups and downs of the TVZ: geodetic observations of deformation around the Taupo Volcanic Zone, New Zealand. *Journal of Geophysical Research: Solid Earth*. 120(6):4667–4679. doi:10.1002/2015jb012125.

Hamling IJ, Kilgour G, Hreinsdóttir S, Bertrand E, Bannister S. 2022a. Estimating the distribution of melt beneath the Okataina Caldera, New Zealand: an integrated approach using geodesy, seismology and magnetotellurics. *Journal of Volcanology and Geothermal Research*. 426:107549. doi:10.1016/j.jvolgeores.2022.107549.

Hamling IJ, Wright TJ, Hreinsdóttir S, Wallace LM. 2022b. A snapshot of New Zealand's dynamic deformation field from Envisat InSAR and GNSS observations between 2003 and 2011. *Geophysical Research Letters*. 49(2):e2021GL096465. doi:10.1029/2021GL096465.

Hammond WC, Blewitt G, Kreemer C. 2011. Block modeling of crustal deformation of the northern Walker Lane and Basin and Range from GPS velocities. *Journal of Geophysical Research: Solid Earth*. 116(B4):B04402. doi:10.1029/2010JB007817.

Harrison AJ, White RS. 2004. Crustal structure of the Taupo Volcanic Zone, New Zealand: stretching and igneous intrusion. *Geophysical Research Letters*. 31(13):L13615. doi:10.1029/2004GL019885.

Harrison A, White RS. 2006. Lithospheric structure of an active backarc basin: the Taupo Volcanic Zone, New Zealand. *Geophysical Journal International*. 167(2):968–990. doi:10.1111/j.1365-246X.2006.03166.x.

Heise W, Caldwell TG, Bibby HM, Bennie SL. 2010. Three-dimensional electrical resistivity image of magma beneath an active continental rift, Taupo Volcanic Zone, New Zealand. *Geophysical Research Letters*. 37(10):L10301. doi:10.1029/2010gl043110.

Holden L, Wallace LM, Beavan RJ, Fournier N, Cas R, Ailleres lL, Silcock D. 2015. Contemporary ground deformation in the Taupo Rift and Okataina Volcanic Centre from 1998 to 2011, measured using GPS. *Geophysical Journal International*. 202(3):2082–2105. doi:10.1093/gji/ggv243.

Hussain E, Wright TJ, Walters RJ, Bekaert DPS, Lloyd R, Hooper A. 2018. Constant strain accumulation rate between major earthquakes on the North Anatolian Fault. *Nature Communications*. 9:1392. doi:10.1038/s41467-018-03739-2.

Johnson KM, Fukuda Ji. 2010. New methods for estimating the spatial distribution of locked asperities and stress-driven interseismic creep on faults with application to the San Francisco Bay Area, California. *Journal of Geophysical Research: Solid Earth*. 115(B12):B12408. doi:10.1029/2010JB007703.

Johnson KM, Tebo D. 2018. Capturing 50 years of postseismic mantle flow at Nankai Subduction Zone. *Journal of Geophysical Research: Solid Earth*. 123(11):10091–10106. doi:10.1029/2018JB016345.

Kato T, El-Fiky GS, Oware EN, Miyazaki S. 1998. Crustal strains in the Japanese Islands as deduced from dense GPS array. *Geophysical Research Letters*. 25(18):3445–3448. doi:10.1029/98GL02693.

Kostrov VV. 1974. Seismic moment and energy of earthquakes, and seismic flow of rock. *Izvestiya, Academy of Sciences, USSR. Physics of the Solid Earth*. 1:23–40.

Kreemer C, Holt WE, Goes S, Govers R. 2000. Active deformation in eastern Indonesia and the Philippines from GPS and seismicity data. *Journal of Geophysical Research: Solid Earth*. 105(B1):663–680. doi:10.1029/1999JB900356.

Lamb S, Moore JDP, Smith E, Stern T. 2017. Episodic kinematics in continental rifts modulated by changes in mantle melt fraction. *Nature*. 547(7661):84–88. doi:10.1038/nature22962.

Li S, Moreno M, Bedford J, Rosenau M, Oncken O. 2015. Revisiting viscoelastic effects on interseismic deformation and locking degree: a case study of the Peru-North Chile subduction zone. *Journal of Geophysical Research: Solid Earth*. 120(6):4522–4538. doi:10.1002/2015JB011903.

Li S, Wang K, Wang Y, Jiang Y, Dosso SE. 2018. Geodetically inferred locking state of the Cascadia megathrust based on a viscoelastic Earth model. *Journal of Geophysical Research: Solid Earth*. 123(9):8056–8072. doi:10.1029/2018JB015620.

Mazzotti S, Le Pichon X, Henry P, Miyazaki S-I. 2000. Full interseismic locking of the Nankai and Japan-west Kurile subduction zones: an analysis of uniform elastic strain accumulation in Japan constrained by permanent GPS. *Journal of Geophysical Research: Solid Earth*. 105(B6):13159–13177. doi:10.1029/2000JB900060.

McCaffrey R. 2002. Crustal block rotations and plate coupling. In: Stein S, Freymueller JT, editors. *Plate boundary zones*. Washington (DC): American Geophysical Union. p. 101–122. (Geodynamic series; 30).

McCaffrey R. 2005. Block kinematics of the Pacific–North America plate boundary in the southwestern United States from inversion of GPS, seismological, and geologic data. *Journal of Geophysical Research: Solid Earth*. 110(B7):B07401. doi:10.1029/2004JB003307.

McCaffrey R. 2009. Time-dependent inversion of three-component continuous GPS for steady and transient sources in northern Cascadia. *Geophysical Research Letters*. 36(7):L07304. doi:10.1029/2008GL036784.

McCaffrey R, Long MD, Goldfinger C, Zwick PC, Nabelek JL, Johnson CK, Smith C. 2000. Rotation and plate locking at the Southern Cascadia Subduction Zone. *Geophysical Research Letters*. 27(19):3117–3120. doi:10.1029/2000GL011768.

Menke W. 2018. Geophysical data analysis: discrete inverse theory. 4th ed. London (GB): Elsevier. 322 p.

Noda A, Matsu'ura M. 2010. Physics-based GPS data inversion to estimate three-dimensional elastic and inelastic strain fields. *Geophysical Journal International*. 182(2):513–530. doi:10.1111/j.1365-246X.2010.04611.x.

Okada Y. 1992. Internal deformation due to shear and tensile faults in a half-space. *Bulletin of the Seismological Society of America*. 82(2):1018–1040. doi:10.1785/bssa0820021018.

Peltier A, Hurst AW, Scott BJ, Cayol V. 2009. Structures involved in the vertical deformation at Lake Taupo (New Zealand) between 1979 and 2007: new insights from numerical modelling. *Journal of Volcanology and Geothermal Research*. 181(3–4):173–184. doi:10.1016/j.jvolgeores.2009.01.017.

Poland MP, Burgmann R, Dzurisin D, Lisowski M, Masterlark T, Owen S, Fink J. 2006. Constraints on the mechanism of long-term, steady subsidence at Medicine Lake volcano, northern California, from GPS, leveling, and InSAR. *Journal of Volcanology and Geothermal Research*. 150(1–3):55–78. doi:10.1016/j.jvolgeores.2005.07.007.

Press WH, Flannery BP, Teukolsky SA, Vetterling WT. 1986. Numerical recipes in FORTRAN. Cambridge (GB): Cambridge University Press.

Rhoades DA, Christophersen A, Gerstenberger MC. 2017. Multiplicative earthquake likelihood models incorporating strain rates. *Geophysical Journal International*. 208(3):1764–1774. doi:10.1093/gji/ggw486.

Sandwell DT, Wessel P. 2016. Interpolation of 2-D vector data using constraints from elasticity. *Geophysical Research Letters*. 43(20):10703–10709. doi:10.1002/2016GL070340.

Savage JC. 1983. A dislocation model of strain accumulation and release at a subduction zone. *Journal of Geophysical Research: Solid Earth*. 88(B6):4984–4996. doi:10.1029/JB088iB06p04984.

Savage JC, Gan W, Svarc JL. 2001. Strain accumulation and rotation in the Eastern California Shear Zone. *Journal of Geophysical Research: Solid Earth*. 106(B10):21995–22007. doi:10.1029/2000JB000127.

Savage JC, Simpson RW. 1997. Surface strain accumulation and the seismic moment tensor. *Bulletin of the Seismological Society of America*. 87(5):1345–1353. doi:10.1785/bssa0870051345.

Seebeck H, Van Dissen RJ, Litchfield NJ, Barnes PM, Nicol A, Langridge RM, Barrel DJA, Villamor P, Ellis SM, Rattenbury MS, et al. 2022. New Zealand Community Fault Model – version 1.0. Lower Hutt (NZ): GNS Science. 97 p. (GNS Science report; 2021/57).

Shen Z-K, Jackson DD, Ge BX. 1996. Crustal deformation across and beyond the Los Angeles basin from geodetic measurements. *Journal of Geophysical Research: Solid Earth*. 101(B12):27957–27980. doi:10.1029/96JB02544.

Shen Z-K, Wang M, Zeng Y, Wang F. 2015. Optimal interpolation of spatially discretized geodetic data. *Bulletin of the Seismological Society of America*. 105(4):2117–2127. doi:10.1785/0120140247.

Sigmundsson F, Vadon H, Massonnet D. 1997. Readjustment of the Krafla Spreading Segment to crustal rifting measured by satellite radar interferometry. *Geophysical Research Letters*. 24(15):1843–1846. doi:10.1029/97GL01934.

Stevens VL, Avouac J-P. 2021. On the relationship between strain rate and seismicity in the India–Asia collision zone: implications for probabilistic seismic hazard. *Geophysical Journal International*. 226(1):220–245. doi:10.1093/gji/ggab098.

Stratford WR, Stern TA. 2004. Strong seismic reflections and melts in the mantle of a continental back-arc basin. *Geophysical Research Letters*. 31(6):L06622. doi:10.1029/2003GL019232.

Stratford WR, Stern TA. 2006. Crust and upper mantle structure of a continental backarc: central North Island, New Zealand. *Geophysical Journal International*. 166(1):469–484. doi:10.1111/j.1365-246X.2006.02967.x.

Tape C, Musé P, Simons M, Dong D, Webb F. 2009. Multiscale estimation of GPS velocity fields. *Geophysical Journal International*. 179(2):945–971. doi:10.1111/j.1365-246X.2009.04337.x.

Tarayoun A, Mazzotti S, Craymer M, Henton J. 2018. Structural inheritance control on intraplate present-day deformation: GPS strain rate variations in the Saint Lawrence Valley, eastern Canada. *Journal of Geophysical Research: Solid Earth*. 123(8):7004–7020. doi:10.1029/2017JB015417.

Villamor P, Berryman KR. 2001. A Late Quaternary extension rate in the Taupo Volcanic Zone, New Zealand, derived from fault slip data. *New Zealand Journal of Geology and Geophysics*. 44(2):243–269. doi:10.1080/00288306.2001.9514937.

Wackernagel H. 1995. Multivariate geostatistics: an introduction with applications. Berlin (DE): Springer. 256 p.

Wallace LM, Barnes P, Beavan J, Van Dissen R, Litchfield N, Mountjoy J, Langridge R, Lamarche G, Pondard N. 2012. The kinematics of a transition from subduction to strike-slip: an example from the central New Zealand plate boundary. *Journal of Geophysical Research: Solid Earth*. 117(B2):B02405. doi:10.1029/2011jb008640.

Wallace LM, Beavan J, McCaffrey R, Darby D. 2004. Subduction zone coupling and tectonic block rotations in the North Island, New Zealand. *Journal of Geophysical Research: Solid Earth*. 109(B12):B12406. doi:10.1029/2004jb003241.

Wang H, Wright TJ. 2012. Satellite geodetic imaging reveals internal deformation of western Tibet. *Geophysical Research Letters*. 39(7):L07303. doi:10.1029/2012GL051222.

Weiss JR, Walters RJ, Morishita Y, Wright TJ, Lazecky M, Wang H, Hussain E, Hooper AJ, Elliott JR, Rollins C, et al. 2020. High-resolution surface velocities and strain for Anatolia from Sentinel-1 InSAR and GNSS data. *Geophysical Research Letters*. 47(17):e2020GL087376. doi:10.1029/2020GL087376.

Wessel P, Smith WHF, Scharroo R, Luis J, Wobbe F. 2013. Generic mapping tools: improved version released. *Eos Transactions*. 94(45):409–410. doi:10.1002/2013EO450001.

Williams CA, Eberhart-Phillips D, Bannister S, Barker DHN, Henrys S, Reyners M, Sutherland R. 2013. Revised interface geometry for the Hikurangi subduction zone, New Zealand. *Seismological Research Letters*. 84(6):1066–1073. doi:10.1785/0220130035.

Williams CA, Wallace LM. 2015. Effects of material property variations on slip estimates for subduction interface slow-slip events. *Geophysical Research Letters*. 42(4):1113–1121. doi:10.1002/2014gl062505.

Williams CA, Wallace LM. 2018. The impact of realistic elastic properties on inversions of shallow subduction interface slow slip events using seafloor geodetic data. *Geophysical Research Letters*. 45(15):7462–7470. doi:10.1029/2018gl078042.

Wu Y, Jiang Z, Yang G, Wei W, Liu X. 2011. Comparison of GPS strain rate computing methods and their reliability. *Geophysical Journal International*. 185(2):703–717. doi:10.1111/j.1365-246X.2011.04976.x.

Zeng Y, Shen Z-K. 2014. Fault network modeling of crustal deformation in California constrained using GPS and geologic observations. *Tectonophysics*. 612–613:1–17. doi:10.1016/j.tecto.2013.11.030.

Zeng Y, Shen ZK. 2016. A fault-based model for crustal deformation, fault slip rates, and off-fault strain rate in California. *Bulletin of the Seismological Society of America*. 106(2):766–784. doi:10.1785/0120140250.

Zeng Y, Petersen MD, Shen Z-K. 2018. Earthquake potential in California-Nevada implied by correlation of strain rate and seismicity. *Geophysical Research Letters*. 45(4):1778–1785. doi:10.1002/2017GL075967.

www.gns.cri.nz

Principal Location

1 Fairway Drive, Avalon
Lower Hutt 5010
PO Box 30368
Lower Hutt 5040
New Zealand
T +64-4-570 1444
F +64-4-570 4600

Other Locations

Dunedin Research Centre
764 Cumberland Street
Private Bag 1930
Dunedin 9054
New Zealand
T +64-3-477 4050
F +64-3-477 5232

Wairakei Research Centre
114 Karetoto Road
Private Bag 2000
Taupo 3352
New Zealand
T +64-7-374 8211
F +64-7-374 8199

National Isotope Centre
30 Gracefield Road
PO Box 30368
Lower Hutt 5040
New Zealand
T +64-4-570 1444
F +64-4-570 4657